Imperial College London

Wear modelling and simulation in moving geometries

Lily Ip

Department of Earth Science and Engineering
Imperial College London

Submitted in part fulfillment of the requirement for the degree of
Doctor of Philosophy of Imperial College London
and the Diploma of Imperial College London

December 2021

Abstract

The aim of this thesis is to describe the new wear modelling framework for the numerical simulation of fully coupled multiphase flows with dynamic boundary motion in response to wear. The framework considers the combination of coupling fluid flow, particle motion, wear modelling and boundary movement within a single model which has not yet been achieved in research. This is of significance in the minerals processing industry from both economical and safety aspects due to the degradation of components as a result of wear from the abrasive nature of slurry flows. The wear modelling framework uses a hybrid Eulerian-Lagrangian modelling approach which tracks particle trajectory with representative Lagrangian particles, with particle-particle interactions modelled statistically through the use of the kinetic theory of granular flow. This approach allows for full coupling of the phases with particle trajectory information required for wear modelling whilst remaining computationally feasible through the use of representative particles.

Boundary movement in response to wear uses an anisotropic unstructured adaptive mesh approach which allows the mesh to move in response to a specified grid velocity and also optimised in order to provide resolution in areas important to the chosen fields and decrease in areas not required at specified time steps. The wear modelling framework takes place between a Python based Lagrangian particle module coupled with a computational fluid dynamics framework developed within Imperial College London called Fluidity.

The framework can be applied to the study of component wear when subject to solid particles entrained in fluids. Component wear is a key consideration in many industries working with particle-laden flow as the study of wear through experimentation or in the field is time consuming and expensive. Simulation of jet impingement in two dimensions confirms the behaviour of boundary deformation in response to wear. A comprehensive study of Coriolis tester arm simulations are conducted to understand the effects of physical parameters on the wear profile obtained. Results are compared with experimental data from Weir Minerals and numerical simulations using the wear modelling framework are able to accurately capture the key characteristics of the wear profile and the behaviour of the particles.

Acknowledgements

One of my goals in life is to contribute new knowledge and understanding that can benefit the world we live in today. I would like to take this opportunity to express my sincerest thanks to the individuals and teams mentioned below who has helped me take a great step in reaching this goal.

Firstly, I would like to thank my supervisors Prof. Stephen Neethling and Prof. Matthew Piggott for giving me the opportunity to pursue a PhD under their supervision. Prof. Stephen Neethling, thank you for your guidance and endless patience. You always made time to share your vast knowledge, words of encouragement and latest Lego builds. Prof. Matthew Piggott, thank you for providing guidance when I needed supported. I will always remember when you reached out to me with this opportunity, for this I am eternally grateful. My mentor Dr. James Percival, thank you for the endless troubleshooting in the technical aspects of this research. Without your support, this thesis would not have been possible.

Special thanks to Emma Watson, the Department Operations Manager for ensuring I had all the support and structure available especially around maternity leave and Tim Greaves for the hours of support with troubleshooting the Fluidity code on Imperial College London's High Performance Computing Service. Thank you to individuals from Weir Minerals who provided guidance and experimental data for which the contents of the thesis was based on. Funding from Engineering and Physical Sciences Research Council and Weir Minerals were generously received, along with computational resources provided by Department of Earth Science and Engineering, Imperial College London High Performance Computing Service and the UK Materials and Molecular Modelling Hub for computational resources.

Thank you to my family and friends for their unwavering love and support, for believing in me and keeping my spirits up during the most difficult times. Special mention to my closest friend Saira, you understood me and my challenges perfectly and possess the special ability to motivate me each time we speak.

Last, but definitely not least, thank you to my husband Terry and my son Teddy. Words cannot express how grateful I am to have you two by my side. And Teddy, guess what... Love You!

Copyright Declaration

Declaration

I hereby certify that the work presented in this thesis was performed by me during my time at Imperial College London and the work of others has been properly acknowledged.

No part of this thesis has been submitted in support of another degree at Imperial College London, or anywhere else.

Lily Ip

December 2021

Contents

List of Figures

List of Tables

Chapter 1

Introduction

Contents

1.1 Overview

Particle-laden wear is of great importance across many industries such as mining and minerals processing, oil and gas, and the handling of aggregates. The movement of these solid particles entrained in fluid causes damage to the component parts leading to material loss due to the abrasive nature of these slurries and over time failure of these components. The study of wear in the field and experimentally is typically expensive, time consuming and limited to a small range of physical parameters, therefore the ability to computationally model and simulate these systems would provide a great advantage to the industry and their processes. Furthermore, having the ability to computationally model wear and its subsequent effect on the system will not only support the potential to design components to minimise the wear experienced but also supports the optimisation of operating parameters in existing designs. Application of this model in industries can result in longer service life of components, improved performance and reliability, leading to increased profit margins in a highly competitive market such as minerals processing.

Existing ways of modelling wear are based on empirical correlations that relates particle impact trajectory and velocity with target material loss rate which are experimentally expensive, time consuming and restrictive to specific test scenarios [Parsi et al., 2014]. However, a more complete approach to modelling and simulation of wear is a complex problem and would require the understanding of:

- Multiphase flow modelling - describing the motion of the solid within the fluid and the coupled interactions between them.
- Wear modelling - describing the wear of materials due to solid particle impingement and it's subsequent effect on the motion of the particle.
- Moving Geometries - describing the movement of the surface deformation in response to wear. This can also be extended to the modelling of systems with moving and rotating components that are of direct industrial relevance such as that of the centrifugal pump.

Therefore, a comprehensive modelling framework incorporating these considerations

in a single model has yet been achieved in literature [Vieira and Shirazi, 2021]. This thesis will focus on the computational modelling of multiphase flows in the form of a slurry with the addition of particle-laden wear against moving boundaries deforming in response to wear. The following sections within this chapter describes the background related to each of the components within this modelling framework.

1.2 Modelling multiphase flows

The study of multiphase flow is a challenging area in fluid dynamics It describes how two or more states of matter interact with each other as well as with the overall system when subjected to various conditions and forces. The study of multiphase flow has many applications in industry such as a nuclear reactors [Colombo and Fairweather, 2015], flow of oil and gas [Pedersen et al., 2017], and flows in minerals processing [Neethling and Barker, 2016]. It is also important in geophysical flows such as sediment transport [Ouda and Toorman, 2019], landslides [Cuomo, 2020] and pyroclastic flows [Jacobs et al., 2013].

Slurry flows is described as a suspension of solid particles in a carrier fluid and is widespread in minerals, chemical and food industries. Unlike the modelling of single phase fluids, slurry transportation is highly complex due to the interactions between the phases as well as the interactions between the various phases and the walls. A wide range of variables can influence the behaviour of slurry flows, these include particle properties such as size, distribution and shape as well as the fluid-particle interface. In addition to the wide range of variables influencing the behaviour of slurry flows, the flow regime is also subject to variation with respect to the properties of the solid relative to the liquid. Initially, Durand and Condolios [1952] developed a flow regime classification based on average particle size which has then been further refined over the years and has now been widely accepted that slurry flows can be classified into four main regimes as shown in Figure 1.1 [Crowe, 2005]. Homogeneous flow is characterized by a uniform distribution of particles throughout the liquid, whereas heterogeneous flow is one which solid particles are sufficiently large and settling occurs such that the particles are no longer uniformly distributed across the

fluid. Flows with a moving or stationary bed are subsets of homogeneous flows. In a moving bed, large particles will settle and slide along the base of the system, whereas in a stationary bed, the flow velocity has become too low to allow for the motion of all particles in the fluid. In most practical situations this last classification of slurry regime is to be avoided. In this thesis, the study focuses on the implementation of models for heterogeneous slurry flows and the subsequent wear this causes on the system walls.

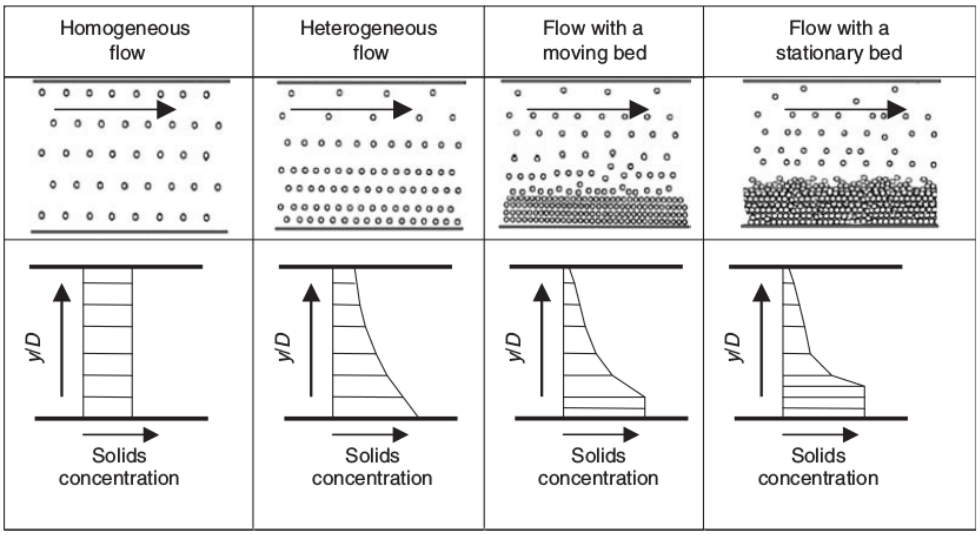

Figure 1.1: Illustration of particle distribution and concentration profile for different slurry flow regimes in a pipe. Figure taken from Crowe [2005].

There are three main methods for modeling and predicting the detailed behaviour of these multiphase flows: experimentally through laboratory scaled equipment and instrumentation [Carey et al., 1988], theoretically using mathematical equations and models for the flow [Kartashev et al., 2017] or computationally where the system is modelled numerically and simulated using high performance computers [Jacobs et al., 2013, Parsi et al., 2019]. Laboratory experiments and theoretical models alone can be limited in accurately capturing the full dynamics of the system, whereas taking a computational approach through the use of a numerical model may be the only viable way to model large scale dynamics [Brennen, 2005]. Another advantage of numerical models is the ability to explore a wide variety of parameters that may be infeasible or expensive to replicate in a laboratory setting.

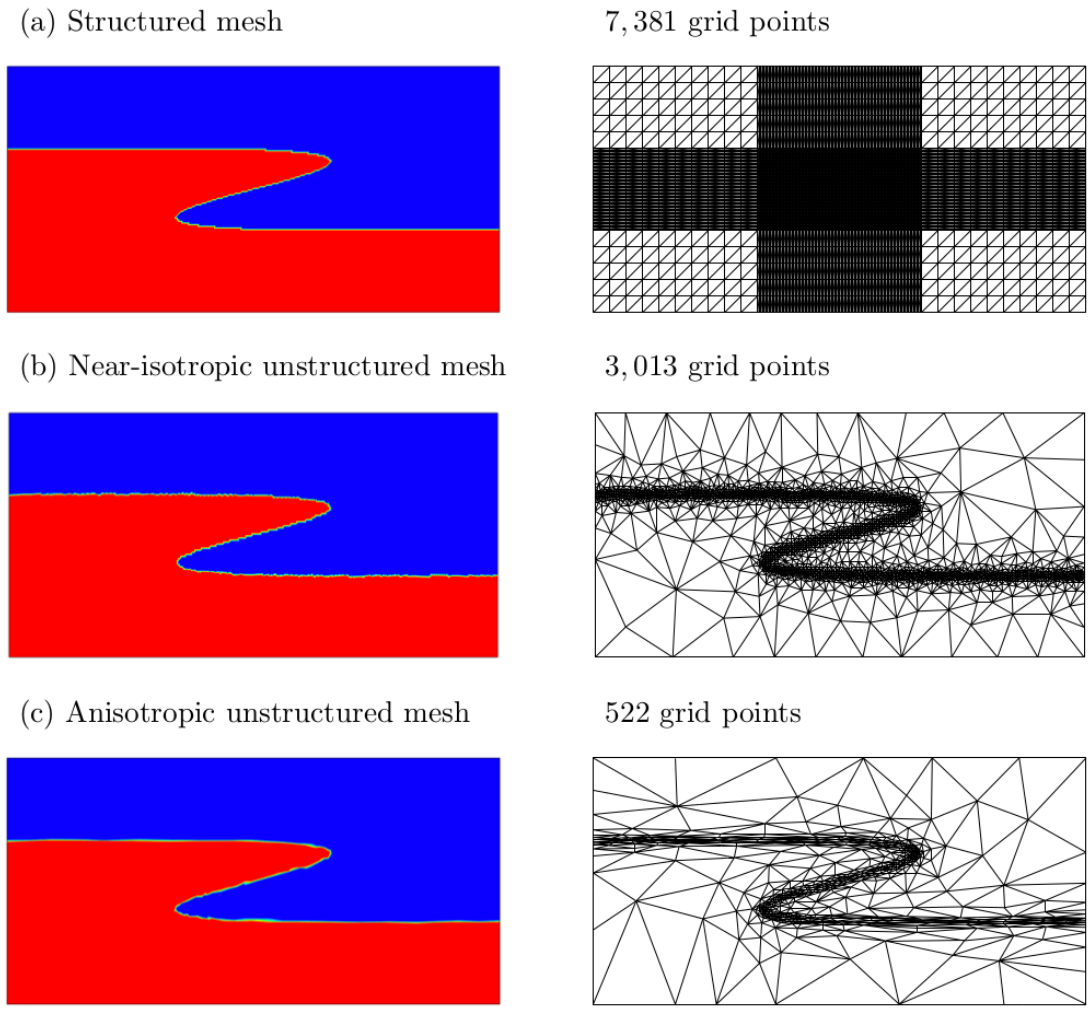

Figure 1.2: Illustrations of a rapidly varying field represented on different meshes and the corresponding solution field. Figure taken from Wilson [2009].

Numerical models describe fluid flow dynamics as a set of continuous equations over a domain or system. These equations in general do not have analytical solutions so therefore will involve the discretisation of the domain forming a mesh where the properties of the flow are approximated on each of the solution nodes in the mesh. A higher resolution of the mesh equates to better accuracy of the solution but at the cost of increased computational footprint and longer simulation time. The computational mesh can take many forms, structured or unstructured, isotropic or anisotropic and fixed or adaptive. Structured meshes are the easiest to implement with each node connected to another using a simple formula which determines the shape of the cell, this means that variations in resolution is difficult to support and increasing resolution in one area would require increasing resolution in areas where it may not be required (see Figure 1.2(a)). As a result, structured meshes are not suitable for complex geometries and becomes inefficient where the same resolution is not required throughout the domain [Pain et al., 2005]. With unstructured meshes, the constraint where nodes are defined by a simple formula is removed and nodes can be arbitrarily connected with one another providing the freedom to provide resolution where required [Piggott et al., 2005]. The rate of which the resolution of the unstructured mesh can vary depends on its isotropy, isotropic and near-isotropic meshes enforces approximately the same node spacing in all directions (see Figure 1.2(b)), whereas an anisotropic mesh allows the resolution to vary across the different directions (see Figure 1.2(c)). An anisotropic unstructured mesh allows for the best use of computational resources in the three examples as it can represent distinct fields with the minimum number of nodes whilst retaining the same degree of accuracy as structured meshes [Wilson, 2009].

Finally, fixed structured or unstructured meshes remain the same throughout a simulation, therefore if the area of interest moves during the simulation, the solution will no longer be optimally represented based on the fixed mesh as the mesh was designed based on the initial conditions. To mitigate this limitation, the use of an adaptive, unstructured, anisotropic mesh can offer the ability to refine the original mesh as the simulation progresses, adapting accordingly and providing resolution where required. Other benefits include faster runtimes as well as reduced

computational costs whilst producing equally accuracy results when compared with a uniform mesh [Piggott et al., 2009]. For example, when studying the effect of wear in slurry flow where resolution is needed along system boundaries experiencing wear whilst reducing computational cost when simulating large scale domains such as that of an entire centrifugal pump. Xie et al. [2014] was able to show an adaptive, anisotropic unstructured mesh was able to yield a more accurate result than a fixed mesh whilst using only 10% of the nodes compared to that of a fixed mesh as seen in Figure 1.3 where the interface of the rising bubble is clearly captured as the simulation progresses compared to the fixed mesh.

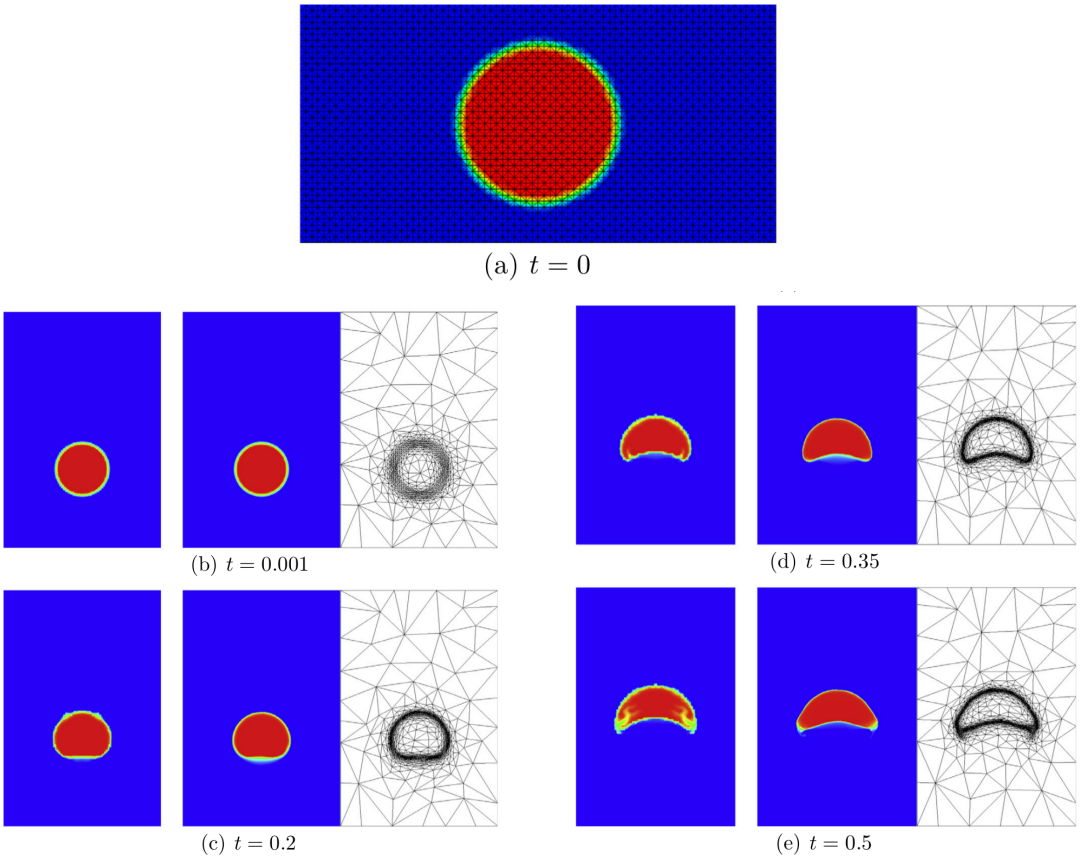

Figure 1.3: Numerical simulation of bubble rising with a comparison with structured and unstructured solution fields on the left and middle columns of panels (b)-(e) with the corresponding adaptive, unstructured, anisotropic mesh on the respective right columns. Panel (a) denotes the same mesh used to initialise the simulations. Figure taken from Xie et al. [2014].

The work in this thesis takes advantage of the adaptive, unstructured anisotropic mesh approach to allow for the flow to be resolved with the minimum number of nodes whilst able to dynamically respond to the flow and the surfaces.

1.3 Wear modelling

Wear of materials due to solid particle impingement places the integrity of many industrial processes at risk when considering the transport of slurries in pipes or in more complex geometries such as that of a centrifugal pump. Transport of solids as a slurry mixture has been used as an effective and economic form of transport of solids over short and medium distances, however, given then abrasive nature of the slurries, it is subject to a large amount of wear. Figure 1.4 displays the effect of wear in a worn centrifugal pump subject, it can be observed that the wear profile is not evenly distributed across the pump with some areas that are subject to substantially more wear than others.

Wear occurs when a particle impacts a surface creating a scar. The shape and size of this scar caused by a single impact depends on many parameters such as surface material properties and particle size, velocity and impact angle. Wear mechanisms are generally considered to be based on the ductility of the surface material, whether it is ductile or brittle. Finnie [1960] first proposed a model for erosion in ductile materials where he suggested it was the result of micro-cutting caused when a particle impacts the surface at a low angle creating a crater. Erosion in brittle materials is due to crack formation, this occurs when a particle hits the brittle surface, creating lateral and radial cracks. Further impacts causes these cracks to grow until these cracks divide the surface into smaller pieces which are then removed by subsequent particles impacting the surface [Parsi, 2015].

Wear in the form of erosion has been studied extensively when applied to simple, stationary geometries such as that of a pipe or elbows (pipe bends), yet according to Meng and Ludema [1995], who surveyed over 5000 papers across two journals, no single predictive equation or group of equations could be found for general use. Wear models can generally be divided into three main categories and are derived either

(a) Volute

(b) Impeller

(c) Impeller from the side

Figure 1.4: Photos illustrating the affect of wear on centrifugal pumps with typical wear patterns. Photos provided by Weir Minerals.

empirically, mechanistically or CFD-based [Parsi et al., 2014]. Wear models based on empirical erosion equations are constructed from data obtained experimentally, Zhang et al. [2007] derived an empirical erosion equation obtained from gas testing and Haugen et al. [1995] derived the coefficients of the general correlation of erosion empirically through the examination of 28 different material types for which they varied particle impact speed and angle.

Empirical equations are simple to implement but uncertainties arise when trying to apply these equations outside of the parameter space used to determine them. As such, they can only be valid for a small use case of scenarios. As a result, mechanistic models based on the physics and mechanisms of erosion were developed for both single phase and multiphase flows. Shirazi et al. [1995] created a mechanistic single phase model where particles decelerate when entering a "stagnation" region close to the wall prior to impact and accounted for many key flow properties such as fluid density, particle velocity, shape, size and density. The model proposed by Shirazi et al. [1995] suffers from two drawbacks; firstly, it assumes that erosion is caused by direct impingement where particle trajectory is a straight line and secondly, this model also does not account for the effect of turbulence on the particle trajectory [Parsi et al., 2014]. In multiphase flow, McLaury and Shirazi [2000] developed a model based on the single phase model by Shirazi et al. [1995], however rather than the characteristic velocity being set to be equal the average flow velocity, it is formed as a mixture of the velocity of the two phases. Parsi et al. [2014] reviewed and categorised multiphase erosion models based on the flow pattern, all of which are based on the model proposed by McLaury and Shirazi [2000] with the exception of Chen et al. [2006]. Chen et al. [2006]'s model estimates erosion for gas/liquid/sand flows by assuming the gas/liquid droplets can be treated as a homogeneous flow and erosion caused by particles in the liquid film is negligible, thus the core gas region can be treated as a single phase model.

Finally, the third type of wear model is that of the CFD-based erosion model. Leveraging a CFD-based model provides the ability to study the effect of different parameters and its interaction with each other in the study of erosion. Clark [2002] summarises the main parameters that can influence erosion to be solid concentration,

particle impact speed, impact angle, size, shape, effects of turbulence and nature of the material properties. This method is particularly useful when exploring complex geometries where it is difficult to set up experimental studies. In general, CFD-based erosion modelling consists of three steps:

- Flow modelling
- Particle tracking
- Application of particle trajectory information to erosion equation

There has been many researchers studying erosion in elbow bends with the use of CFD (Zhang et al. [2007], Chen et al. [2004, 2006], Fan et al. [2001]), and Gandhi et al. [2012], Ferng [2008] and Atkinson et al. [2007] studied erosion in complex geometries. However, with these CFD based models they fail to take into account the effect of surface profile changes on subsequent erosion events. Nguyen et al. [2014] identified that surface profile changes has a significant impact on wear mechanisms. Despite Nguyen et al. [2014]'s investigation, Messa and Malavasi [2018] reported few attempts made to take into account geometry changes in response to wear prediction models. Parsi et al. [2019] and Agrawal et al. [2019] took into account surface deformation on erosion prediction by leveraging the Moving Deforming Mesh (MDM) approach within ANSYS 19.1, however, the limitation in both these studies is the flow is assumed to be steady, dilute and one-way coupled. This thesis aims to address the gap by presenting a fully coupled multiphase wear prediction models with the use of moving geometries discussed in Section 1.4 and details of the coupling strategy in Section 2.4.

1.4 Moving Geometries

Moving geometries have many important industrial and geophysical applications, such as in the study of land slides [Wilson, 2009, Nian et al., 2021], modelling of turbomachinery [Tyacke et al., 2019, Odier et al., 2021] and rotating geometries such as tidal turbines [Mcnaughton et al., 2014] and the study of erosion [Agrawal et al., 2019, Parsi et al., 2019]. It is a difficult problem to solve when simulating flow

problems as the domain cannot be easily represented using a single structured or unstructured mesh. In many cases, these geometries needs to be broken down and represented by different mesh types. There are four main approaches when dealing with moving geometries in terms of mesh approaches. These are:

- Multiple reference frame (MRF)
- Sliding mesh method
- Chimera method
- Dynamic mesh method

The multiple reference frame approach, also known as the frozen rotor approach is the simplest approach where geometries are represented either as a stationary zone or moving reference frame zone as depicted in Figure 1.5. The flow properties are translated across the interface between the static and the moving reference frames with steady state flow conditions assumed at the interface between the two reference frames. This method provides a fast approximation for use in turbomachinery modelling. Although simple to implement, the meshes remain fixed and do not take into account the relative motion of the moving zone [Luo and Gosman, 1994]. As a result, this method cannot be used where the motion of the moving zone is required to calculate the effect of wear and particle collisions with the moving geometry.

Another method for modelling rotating geometries or geometries where there exists a zone between a moving and stationary domain is with the use of the sliding mesh. This approach uses two or more regions joined via an overlapping interface region where the flow properties are interpolated between the stationary and moving regions as seen in Figure 1.6. Unlike the MRF approach, the moving frame or region represents genuine motion, however the interpolation between the regions over the interface is often expensive and can be non conservative resulting in the generation of artifacts. [Mcnaughton et al., 2014].

When complex geometries need to be modelled as a complete system, the Chimera or overset approach can be adopted. This approach takes a complex geometry and

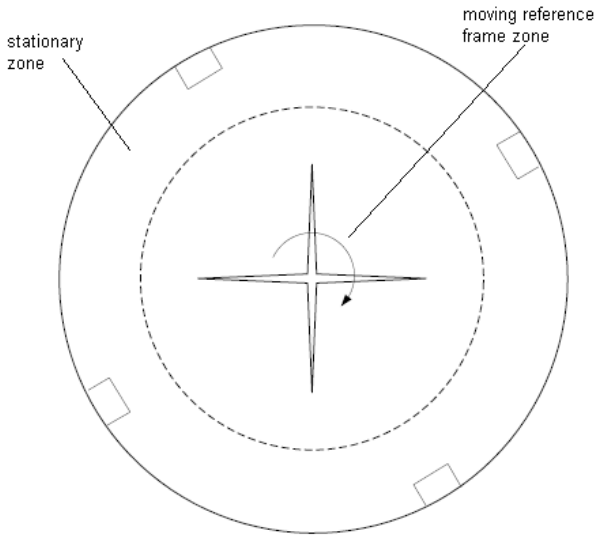

Figure 1.5: Illustration of a geometry using MRF approach with one rotating impeller modelled using a single moving reference frame zone, the dotted line represents the interface where flow properties are translated between the two reference frames. Figure taken from ANSYS Inc. [2009].

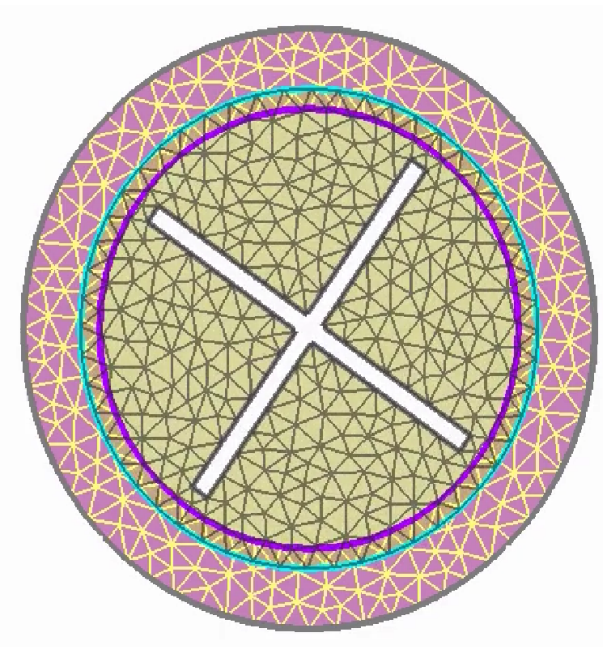

Figure 1.6: Illustration of a geometry using sliding mesh approach, consists of an external static region in red, yellow rotating region and an overlapping interfaces represented in the region between turquoise and purple.

decomposes it into smaller systems, typically made up of unstructured meshes overlapping an overall background grid made up of a simple structured mesh. Flow properties between the background and the decomposed components are the interpolated across the interface with the boundary condition at the interface taken as that of the overset component [Meakin, 1999]. Figure 1.7 represents the grid generation of a wind turbine consisting of 13 decomposed components made up of blades, tower, floor and hub Li et al. [2012]. This is a very powerful technique and can be used in the modelling of overlapping boundaries or geometries with shared wall boundaries, however, it comes at a high computational cost.

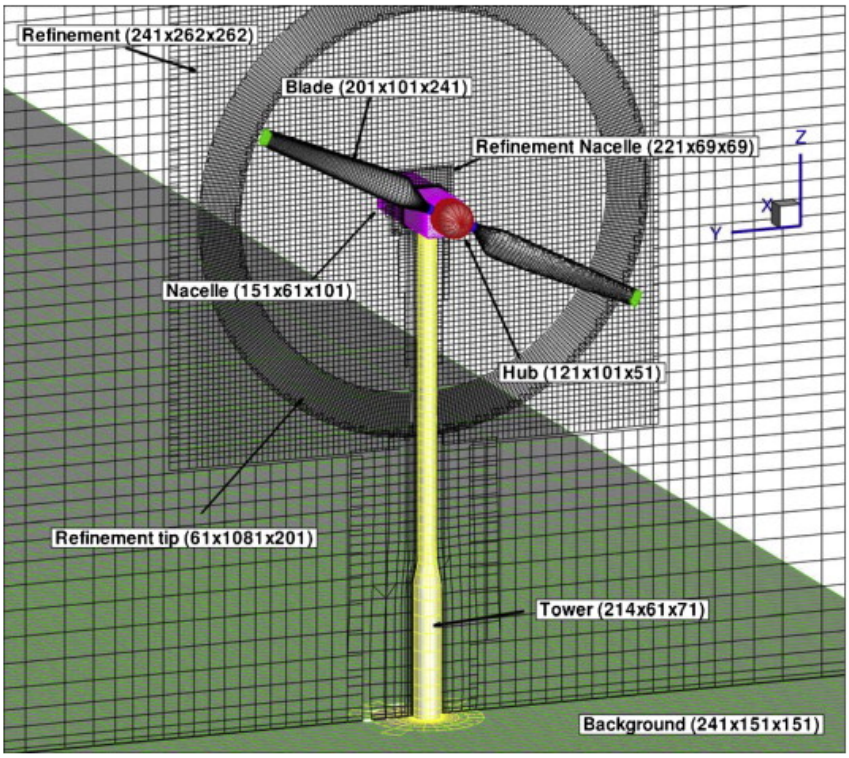

Figure 1.7: Example of the Chimera approach in grid design for a complex system. Figure taken from Li et al. [2012].

Finally, there is the dynamic mesh movement method where the shape of the system changes over time in response to motion along the boundaries of the domain. For example, in the modelling of the rotating centrifugal pump, the motion must describe the rotating impeller and when modelling wear, this should describe the wear velocity experienced along the boundary due to the impact of solid particles. Mesh movement methods that describe the deformation and movement of the mesh

include Laplacian smoothing, the spring-based smoothing method and elasticity based methods and is summarised in Mcmanus et al. [2017]. Figure 1.4 illustrates a 2D adaptation of a centrifugal pump with a rotating impeller modelled using the dynamic mesh movement method available within Fluidity, a finite element/control volume based CFD framework described in detail in Section 1.5. Dynamic mesh movement methods provide the ability to solve complex geometries without the need for the computational overhead of interpolation and the risk of generating artifacts as interpolation is non conservative, however, it does come with an overhead when performing the mesh movement. For the purpose of surface deformation in response to wear both Agrawal et al. [2019] and Parsi et al. [2019] deployed their model using the dynamic mesh movement method and for the purpose of this thesis, the mesh movement and adaptivity methods available within Fluidity will be leveraged.

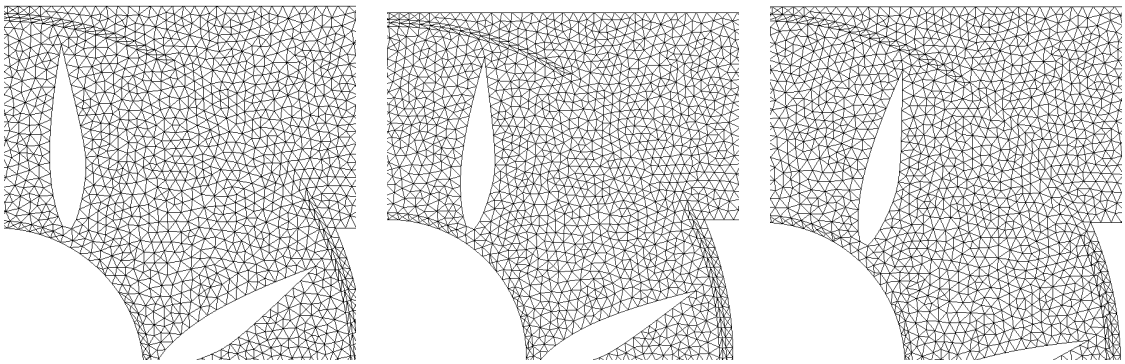

(a) Timestep = 1 (b) Timestep = 5 (c) Timestep = 10

Figure 1.8: Close up of 2D representation of centrifugal pump over 10 timesteps with remeshing of the cells as the impeller rotates. The simulation is set to remesh every 2 time steps to account for the rotating impeller ensuring the cells remains well formed.

1.5 Fluidity - an anisotropic unstructured adaptive mesh framework

Fluidity is a flexible, massively parallel finite element/control volume based CFD framework developed at Imperial College London [Piggott et al., 2008, Imperial

College London, 2014]. It contains the capability to produce adaptive, anisotropic, unstructured meshes and is also capable of executing parallel workloads with the use of an Message Passing Interface (MPI) library making the study of many multiphase problems with complex geometries feasible [Imperial College London, 2014, Pain et al., 2001, Piggott et al., 2009]. Fluidity is also well tested throughout its continued development, test cases are created ranging from unit tests of individual subroutines to full simulations of an analytical cases to maintain its validity as it continues to be developed. Automated testing of builds occur before its release through Jenkins, an open source continuous integration/continuous development automation server, has been implemented thus ensuring software development best practices are followed and the results of simulations conducted using this framework can be trusted Farrell et al. [2010].

Fluidity has proven to be a powerful tool in the modelling of complex domains through its use of the adaptive, anisotropic, unstructured mesh. Jacobs et al. [2013] simulated the transport of volcanic ash plumes, Wilson [2009] developed a novel mutliphase approach for simulating landslide generated tsunamis and Bhutani [2016] modelled the polydispersity of the gas bubbles in froth flotation. The adaptive anisotropic unstructured mesh technology and multiphase capabilities along with the framework's robustness and flexibility for continued development makes Fluidity the ideal framework to develop a new multiphase wear model with moving geometries.

1.6 Statement of Novel Contribution and Structure of Thesis

In this thesis, the aim is to create a single modelling framework that is capable of

- Modelling a fully coupled multiphase flow
- Track particle trajectories
- Calculate wear on target material
- Dynamically deform surface in response to wear

This would create the first known approach of modelling wear in a fully coupled multiphase flow with dynamically deforming boundaries within a single modelling framework. The new wear modelling framework leverages Fluidity's adaptive unstructured mesh technology, for the study of wear due to solid particle impingement. The application of this model concerns the simulation of complex fully coupled multiphase flows with surfaces of the system that can dynamically deform in response to wear applicable to many industrially relevant processes.

The model builds upon an existing Lagrangian particle model that is coupled to the well developed Fluidity framework. The new modelling framework is implemented across the Lagrangian particle model as well as modifications made within Fluidity to allow for coupling between the two frameworks. Existing wear prediction in literature is mainly conducted empirically with limited models that fully couple fluid flow and consider particle motion and wear within a single model. No models exists before this thesis that combines all the elements together in addition to boundary deformation in response to wear [Parsi et al., 2014, Vieira and Shirazi, 2021, Meng and Ludema, 1995, Messa and Malavasi, 2018].

Chapter 2 reviews the fundamentals aspects of multiphase flow modelling and wear modelling. It starts with the introduction of basic concepts and definitions taken from literature. Different multiphase modelling approaches are discussed and the governing equations describing the motion of multiphase flows are given. Interaction terms used to fully couple the phases are presented. Chapter 3 discusses the discretisation of the model equations. The Galerkin finite element method is used to discretise the momentum and continuity equations while the control volume method is used for the discretisation of the particle volume fraction within Fluidity. The chapter ends with an overview of Fluidity's adaptive mesh approaches.

In Chapter 4, I introduce the new wear modelling framework. It starts with the adaptations of the governing equations presented in Chapter 2 and a description of how it is adapted and applied within the model along with the associated initial conditions and boundary conditions. The solution method is presented highlighting the main algorithm with which the wear model is coupled with the particle and fluid models. Discretisation of the Lagrangian particles is provided here as well as

methods to smooth out the wear across the control volume. Scaling parameters that accelerate the effect of wear and the number of particles are provided here. Model verification in the form of mesh and time convergence is conducted. Validation test in the form of a 3D sedimentation simulation confirms the behaviour of the solid-fluid coupling when compared with analytical results. A jet impingement simulation conducted with surface deformation in response to wear confirms the importance that changes to the surface can have on future wear behaviour.

In Chapter 5, I bring all the individual components of the wear modelling framework together to conduct a thorough investigation into the modelling of multiphase flow with boundary movement in response to wear. The simulation setup is provided in the form of a 3D backward facing step along with the surface material and particle properties considered as part of this investigation. Validation of the simulations is compared with experimental data and results discussed. I show that the wear modelling framework simulations agree well with experimental data and observations. In Chapter 6, the sensitivity of modelling parameters and the effects of varying physical parameters are studied.

Finally in Chapter 7, I summarise the main developments of the thesis along with the main findings and conclusions of the simulations conducted. I discuss possible future developments and industrial applications of the model. This includes the extension of the work to more complicated and industrially relevant geometries, such as wear within a centrifugal slurry pump.

Chapter 2

Fundamentals of Multiphase Flow and Wear Modelling

Contents

2.1 Overview

This chapter provides an overview of the fundamentals of multiphase flow and wear modelling. It describes general definitions for multiphase flow, the frames of reference used in the modelling of these flows before focusing on the solid fluid coupling of dispersed multiphase flow and the integration of impingement wear models used within this thesis. The set of equations governing the motion of multiphase flow, the interaction terms coupling phases through the use of inter-phase drag and kinetic theory of granular flow as well as the semi-empirical impingement wear model are discussed and introduced in Sections 2.3 and 2.4 with a summary of all equations used in Section 2.5.

2.2 Fundamental Definitions

2.2.1 Multiphase Flow

Multiphase flow is defined as the flow of a mixture of two or more phases (gas, liquid, solid etc.). Each phase can be considered as dispersed or continuous. Disperse phase flows are ones in which individual or discrete elements, generally referred to as particles, are finite and not connected. The continuous or carrier phase is a connected liquid or gas in which the dispersed phase is transported and immersed [Crowe, 2005]. Examples of multiphase flows is summarised in Table 2.1.

Disperse flows can be further separated into dense and dilute flows where each type of flow can require different approaches to model their behaviour. They are mainly classed by the dominating interactions that occurs within the system. A dilute flow is one where the particle motion is dominated by the fluid forces such as drag and lift which can be considered as fluid-particle interactions. Whereas a dense flow is one where the particle motion is controlled by collisions within or between dispersed phases. These are considered as particle-particle interactions when it is within the same disperse phase or inter-particle interactions when it is between different dispersed phases. It is said that particle-particle and inter-particle interactions becomes important enough to be considered when the particle volume

Continuous-dispersed phase	**Industrial and technical application**
Gas-solid flows	Pneumatic conveying, particle separation in cyclones and filters, fluidised beds
Liquid-solid flows	Hydraulic conveying, liquid-solid separation, particle dispersion in stirred vessels
Gas-droplet flows	Spray drying, spray cooling, spray painting, spray scrubbers
Liquid-droplet flows	Mixing of immiscible liquids, liquid-liquid extraction
Liquid-gas flows	Bubble columns, aeration of sewage water, flotation

Table 2.1: Summary of two-phase flow systems and important industrial and technical processes. Table from Sommerfeld [2017].

fraction exceeds 10^{-3} [Elghobashi, 1994].

In real life applications, dispersed phases can contain a wide range of physical particle properties, such as a variety of material properties or particle sizes within the continuous fluid phase. This can be simplified and taken to be an average of the particle properties, such as taking a mean particle diameter. However, if these properties are too wide ranging, it can affect the dynamics and accuracy of the model when modelled as a single collection of particles. Thus, it can be necessary to consider particle properties and group each collection of particles into separate dispersed phases. Similarly, extensions can be made to consider three phase flows, for example bubbles forming in a slurry mixture [Crowe, 2005].

The work presented in this thesis focuses on dispersed multiphase flow consisting of a single liquid continuous phase and a single dispersed phase made up of particles of the same size and material.

2.2.2 Coupling

When considering dispersed multiphase flows, the transport of the particles by the continuous fluid phase and their interactions are important considerations. These inter-phase interactions can be characterised depending on the concentration of the particles as the concentration of particles will affect the fluid dynamic interactions, collisions and cohesions within the carrier fluid as depicted in Figure 2.1 [Sommerfeld, 2017].

The types of coupling between the phases is illustrated in Figure 2.2 and summarised in Table 2.2. Three-way coupling can be considered as a special case of two-way coupling where particle disturbances of the local fluid can affect other particles locally, for example drafting of a trailing particle Crowe [2005].

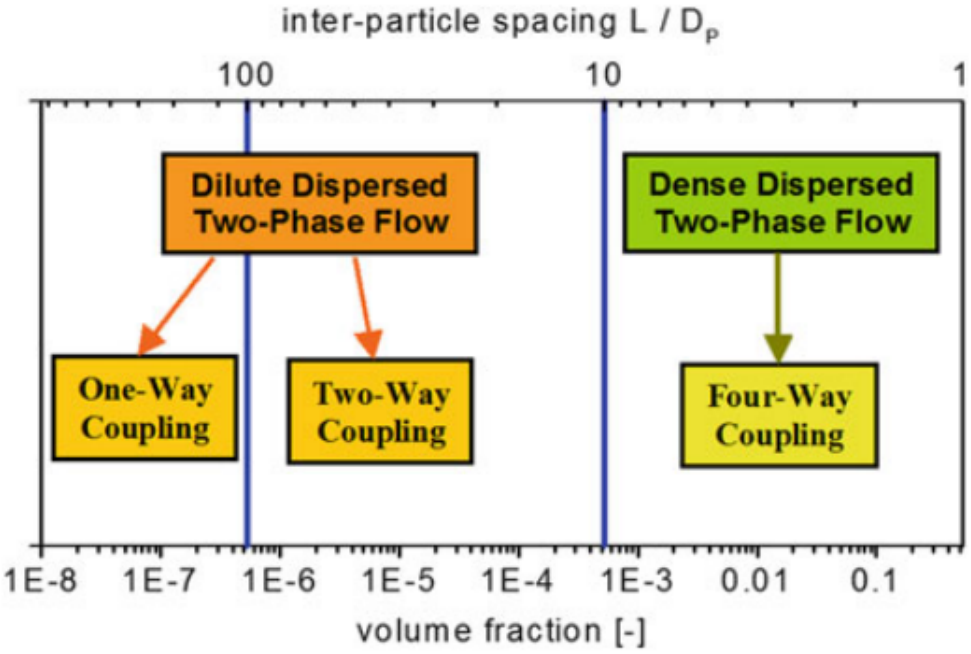

Figure 2.1: Two phase flow regimes and coupling as a function of particle volume fraction. [Sommerfeld, 2017].

For this thesis, a four-way coupling modelling approach is adopted. This four-way coupling takes into account particle-fluid, fluid-particle interactions modelled through the use of drag terms, and particle-particle interactions through the use of solid pressure controlled by granular temperature. Details of the drag and granular

Coupling level	Description
One-way	Flow of the continuous phase affecting the only the dispersed phase with no reverse effect. This type of coupling is suitable for very dilute flows where the particles in the dispersed phase has negligible influence on the flow in the continuous phase.
Two-way	There exists a mutual effect between the flows in the continuous and disperse phase, where in addition to one-way coupling, the particles in the disperse phase can influence the fluid flow and the effects needs to be accounted for.
Four-way	Occurs when particle-particle interactions also affects the multiphase motion in addition to two-way particle-fluid coupling. For example, particle collisions affecting the motion of both particles.

Table 2.2: Summary of the different levels of coupling describing the interactions between the disperse and continuous phases [Crowe, 2005, Sommerfeld, 2017, Elghobashi, 1994, Loth, 2000].

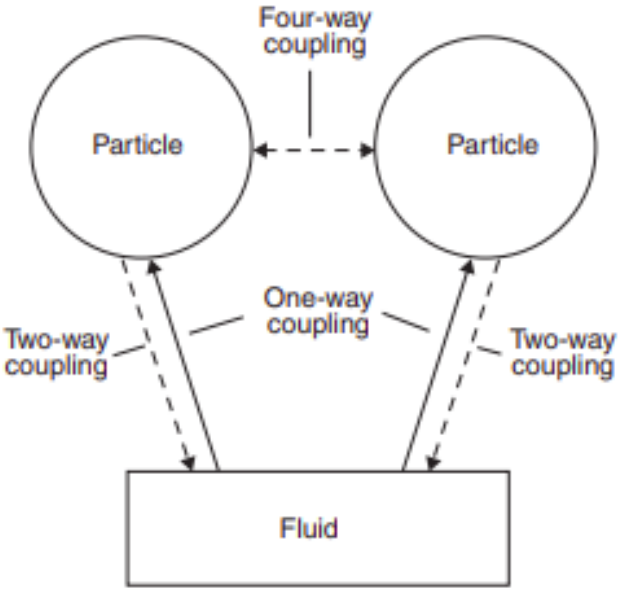

Figure 2.2: Illustration of inter-phase interactions through coupling. [Crowe, 2005]

temperature interactions are discussed in Section 2.4.

2.2.3 Particle Laden Wear

Particles in a fluid can also interact with the walls of the domain. These interactions can not only influence the particle motion but can also result in wear and deformation of the walls themselves. Particle-laden wear of materials is a complex problem involving the modelling of flow, tracking of particles and adopting an appropriate wear prediction. There are no universally accepted models for particle-laden wear prediction and most models are derived from experimental data [Meng and Ludema, 1995]. Wear rate prediction is dependent on a number of factors including particle impact angle, impact velocity, surface material properties and particle properties such as size, shape and hardness [Oka and Yoshida, 2005, Oka et al., 2005].

Meng and Ludema [1995] conducted an analysis into wear models, with the models being categorised by the methods of wear into mechanical, chemical or thermal which is summarised in Table 2.3. The cutting mechanism is caused by an oblique impact where a particle impacts the surface material at shallow, grazing angles.

Deformation is caused by head on collisions of particles normal to the surface of the material [Arabnejad et al., 2015b, Meng and Ludema, 1995]. For the purpose of this thesis, chemical and thermal wear actions are out of scope and the choice of mechanistic wear model will be ones based on material loss due to cutting and deformation. Details of the selected wear model and its associated equations are discussed in Section 2.4.3.

Wear mechanism	**Description**
Chemical	Loss of material through chemical dissolution or reaction with the surface materials causing formation of a new substance that is more readily removed.
Thermal	Loss of material due to melting or change in material properties increasing the rate of wear.
Mechanical	Loss of material due to cutting, deformation and fatigue of the material.

Table 2.3: Summary of the different methods of wear mechanisms adapted from[Meng and Ludema, 1995].

2.3 Governing Equations

The governing equations describing multiphase flow are presented here. The standard equations, such as the Navier-Stokes equation for single phase flows needs to be adapted to account for the presence of a second phase. Parameters such as velocity and density associated with a particular phase is identified with a subscript. For example, ρ_p will denote the density of the particles in the dispersed phase and ρ_f the fluid density of the continuous phase. It is important to note that although the governing equations described below are written for 2 phases (solid and fluid), general multiphase flow models such as that implemented in Fluidity are valid for an arbitrary number of dispersed phases and thus each phase can be identified using an index $i = 1, 2, 3...n$, where n is the total number of phases modelled in the flow.

Additional interaction and parameterisation terms that makes up the complete wear model are provided in Section 2.4.

2.3.1 Reference Frames

The frames of reference determines the method with which the motion for the particle or fluid phase is described through space and time. The choice of appropriate reference frames is an important consideration as it can have implications on the information available to the system when combined as well as having an impact when solving the equations numerically.

The Eulerian reference frame determines flow properties by looking at the flow at fixed points in the domain [Batchelor, 1967]. The Eulerian frame of reference considers the phase as a continuum, which allows a small volume of the domain known as a control volume to be considered and averaging applied to flow properties. This can be seen with the introduction of volume fractions α_f or α_p, denoting the fraction or concentration of the fluid or particle where $\alpha_f + \alpha_p = 1$ Crowe [2005].

The Lagrangian reference frame considers the flow properties by observing an individual particle as it moves through time and space and is able to track the trajectory of the particle [Batchelor, 1967].When a Lagrangian frame of reference is applied to the dispersed phase, the coupling with the fluid usually relates to the density of the number of particles. This can be used to obtain local particle concentration within the fluid phase such that $\alpha_p = n_p V_p$, where n_p is the particle number density and V_p the average particle volume [Crowe, 2005].

Two approaches are generally used when modelling two-phase flow problems. These are the Eulerian-Eulerian and the Eulerian-Lagrangian model. The Eulerian-Eulerian model is also known as the two-fluid model (TFM) and treats both the fluid and particle phases as continuums. The TFM normally requires fewer computational resources compared to Eulerian-Lagrangian models, however, modelling the particle phase as a continuum loses important particle information such as particle trajectory. To overcome this limitation, three main Eulerian-Lagrangian methods can be adopted. These are the discrete element method (DEM), the multiphase particle-in-cell (MP-PIC) method and the dense discrete phase model (DDPM) [Chen and

Wang, 2014]. DEM tracks solid particles individually and is able to obtain detailed particle-particle interactions and particle-wall collisions. However, this comes with a high computational demand and is limited to small scale simulations [Nguyen et al., 2014, Xu et al., 2012]. MP-PIC method groups particles into parcel representing a collection of real particles with identical properties and particle-particle interactions are modelled through a solid stress tensor [Andrews and O'Rourke, 1996, Adnan et al., 2020]. DDPM is a new hybrid Eulerian-Lagrangian approach which models particle-particle interactions statistically in the averaged sense instead of tracking individual particles through the use of the kinetic theory of granular flow (KTGF) with the probability of a particle being present at a given location equal to the local particle volume fraction within the cell [Chen and Wang, 2014]. This is achieved in DDPM by solving the fluid phase in the Eulerian frame of reference while the motion of solid phase is solved on the Lagrangian frame of reference with the use of Newton's second law of motion. DDPM incorporates the effects of the particle phase with the fluid by sharing the pressure term, while particle-particle interactions are handled through the use of a solid pressure modelled by the KTGF using expressions defined by Lun et al. [1984]. Similar to the MI-PIC method, DDPM tracks representative Lagrangian particles instead of individual particles [Arabnejad et al., 2017, Adnan et al., 2020].

The work presented in this thesis adopts the hybrid Eulerian-Lagrangian DDPM as the Lagrangian frame of reference in the particle phase is essential in obtaining the trajectory information required for the wear model and this is still modelled directly. Tracking the particle-particle interactions statistically through the use of KTGF allows for simulations of large domains whilst remaining computationally feasible [Chen and Wang, 2014, Cloete et al., 2012].

2.3.2 Averaging (Control Volume for Particles)

When describing the dispersed particle phase using DDPM, a hybrid Eulerian-Lagrangian approach, the Eulerian frame of reference is used to obtain averaged values for the representative particles through the use of control volumes. The control volume requires the length scale of the particles when compared to the control

volume to be carefully considered. The control volume should be at the mesoscale, set as the size of a collection of particles which is much smaller than whole domain which is at the macroscale but larger than that of the individual particles. The particles should then be at a microscale (molecular level), so that a representative amount of particles can be considered within each control volume [Michaelides et al., 2017].

There are three methods of averaging the Eulerian phase equations, namely time, volume and ensemble averaging. Time averaging averages the flow properties over time at a specific point in the flow, this is constrained by the property that the averaged time T must be at a larger scale when compared to the local fluctuating time t', yet smaller than the time associated with the whole system T' [Ishii, 1975]. Volume averaging averages the flow properties at a point in time over a volume, then assigning the averaged value back to a point in the flow. This is constrained with similar length scale properties as with time averaging where the averaging volume L^3 must be larger than the characteristic distance between particles [Soo, 1990]. Figure 2.3 illustrates the requirements of the control volume where L_{p-p} is the length scale of the characteristic distance between particles and Δx the length scale of the control volume. Finally ensemble averaging avoids the constraints of time and volume averaging and is based on the probability of the flow field being in a specific configuration at a given time [Drew and Passman, 1999]. The governing equations presented in this thesis follow the volume averaging approach.

2.3.3 Conservation of mass

As mass of a fluid must be conserved, this fundamental principal can be expressed in the form of the conservation of mass, also known as the continuity equation. For a multiphase system using the DDPM approach, the conservation of mass for the fluid phase is [Chen and Wang, 2014].

$$\frac{\partial(\alpha_f \rho_f)}{\partial t} + \boldsymbol{\nabla} \cdot (\alpha_f \rho_f \boldsymbol{u}_f) = 0. \tag{2.1}$$

The term α_i is the volume fraction of the fluid phase i and is introduced by the averaging process when working with control volumes in order to define what fraction

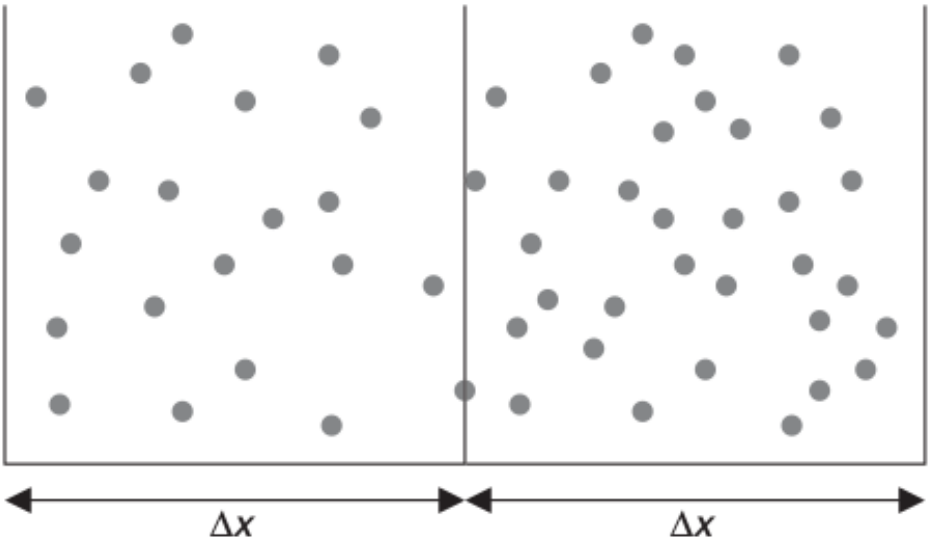

Figure 2.3: Two-dimensional representation of discrete particles in adjoining computational cells where >> L_{p-p} [Crowe, 2005].

of the entire volume is occupied by phase i The volume fraction can be expressed as

$$\alpha_i = \frac{V_i}{V} \tag{2.2}$$

where V_i is the volume of phase i and V is the total volume of the control volume, the volume fraction of the phases is subject to the constraint

$$\sum_{i=1}^{N_{phases}} \alpha_i = 1. \tag{2.3}$$

The work in this thesis is limited to a fluid phase and a particle phase with volume fractions denoted as α_f and α_p respectively and thus has the constraint

$$\alpha_f + \alpha_p = 1. \tag{2.4}$$

Furthermore, the fluid is assumed to be incompressible, thus the conservation of mass takes the form

$$\boldsymbol{\nabla} \cdot (\alpha_f \boldsymbol{u}_f) + \boldsymbol{\nabla} \cdot (\alpha_p \boldsymbol{u}_p) = 0. \tag{2.5}$$

2.3.4 Conservation of momentum

The equations describing the conservation of momentum for the fluid phase is given by [Chen and Wang, 2014]

$$\frac{\partial(\alpha_f \rho_f \boldsymbol{u}_f)}{\partial t} + \alpha_f \rho_f \boldsymbol{u}_f \cdot \boldsymbol{\nabla} \boldsymbol{u}_f = -\alpha_f \boldsymbol{\nabla} p + \boldsymbol{\nabla} \cdot \bar{\bar{\tau}}_f + \alpha_f \rho_f \boldsymbol{g} + K(\boldsymbol{u}_p - \boldsymbol{u}_f) \tag{2.6}$$

where p is the pressure shared by both fluid and particle phases, $\bar{\bar{\tau}}_f$ is the viscous stress tensor, $\boldsymbol{g}$ the gravitational acceleration and $K(\boldsymbol{u}_p - \boldsymbol{u}_f)$ the drag force describing the momentum exchange between the two phases.

To consider the effect of viscosity on the fluid, the viscous stress tensor for the a Newtonian fluid such as water is defined as

$$\bar{\bar{\tau}}_f = \mu_f(\boldsymbol{\nabla} \boldsymbol{u}_f + \boldsymbol{\nabla}(\boldsymbol{u}_f)^T) - \frac{2}{3}\mu_f(\boldsymbol{\nabla} \cdot \boldsymbol{u}_f)\mathbb{I}, \tag{2.7}$$

where μ_f is the dynamic viscosity and $\mathbb{I}$ the identity matrix. Taking the assumption that the viscosity is constant and the flow is incompressible, the stress tensor becomes

$$\boldsymbol{\nabla} \cdot \bar{\bar{\tau}}_f = \mu_f \boldsymbol{\nabla}^2 \boldsymbol{u}_f. \tag{2.8}$$

Substitution Equation 2.8 into Equation 2.6 gives the incompressible Navier-Stokes equation

$$\frac{\partial(\alpha_f \rho_f \boldsymbol{u}_f)}{\partial t} + \boldsymbol{\nabla} \cdot (\alpha_f \rho_f \boldsymbol{u}_f \otimes \boldsymbol{u}_f) = -\alpha_f \boldsymbol{\nabla} p + \mu_f \boldsymbol{\nabla}^2 \boldsymbol{u}_f + \alpha_f \rho_f \boldsymbol{g} + K(\boldsymbol{u}_p - \boldsymbol{u}_f). \tag{2.9}$$

The inter-phase drag in the momentum equation is obtained from summing up the drag forces acting on all the particles within a control volume. This is defined by

$$K(\boldsymbol{u}_p - \boldsymbol{u}_f) = \sum_{i=1}^{N} m_i \beta \frac{(\boldsymbol{u}_{pi} - \boldsymbol{u}_f)}{V}, \tag{2.10}$$

where N is the total number of particles in a control volume V, m_i the mass of the particle, $\boldsymbol{u}_{pi}$ the velocity of particle i and finally the drag coefficient β is described in Section 2.4.1.

2.3.5 Representative particles

The representative particle phase satisfies an additional set of equations described by Newton's second equation of motion for each representative particle in the system.

Trajectory of the particle required for the calculation for particle wall collisions is calculated by a force balance given by [Chen and Wang, 2014]

$$\rho_p \frac{\mathrm{d}\boldsymbol{u}_p}{\mathrm{d}t} = \boldsymbol{g}(\rho_p - \rho_f) + \beta(\boldsymbol{u}_f - \boldsymbol{u}_p) + \boldsymbol{F}_{\boldsymbol{KTGF}}, \tag{2.11}$$

where the terms on the right hand side represents the force contributions due to gravity, inter-phase drag and inter-particle interactions respectively. The inter-particle interactions in DDPM, $\boldsymbol{F}_{\boldsymbol{KTGF}}$, is derived from solid particle pressure using the kinetic theory of granular flow defined in Section 2.4.2 and is of the form:

$$\boldsymbol{F}_{\boldsymbol{KTGF}} = \boldsymbol{\nabla}\overline{\overline{\tau}}_p, \tag{2.12}$$

where $\overline{\overline{\tau}}_p$ is the particle phase stress tensor. Finally the position of representative particle position $\boldsymbol{x_p}$ is tracked by integrating the particle equation of motion (2.11):

$$\frac{\mathrm{d}\boldsymbol{x}_p}{\mathrm{d}t} = \boldsymbol{u}_p. \tag{2.13}$$

2.4 Interaction Terms

2.4.1 Drag model

The primary method of coupling fluid and particle interactions is through the use of drag terms. This models the transfer of momentum between the continuous fluid phase with the averaged particle flow. There are many drag laws existing in the literature that can be employed as part of the model. Stokes [1851] drag correlation provides sufficient accuracy for gravity driven particle settling and when dealing with particle Reynolds number < 1. Wen and Yu [1966] drag correlation uses the experimental data from Richardson and Zaki and is valid when the flow is out of the Stokes regime and viscous forces dominate the flow behaviour [Lundberg and Halvorsen, 2008]. The Ergun [1952] drag model can be used for dense beds where particle volume fractions within the fluid raises above $\alpha_p \geq 0.2$. This is valid when the drag coefficient drops in dense beds as observed in Figure 2.4. There are also drag correlations derived from Lattice-Boltzmann numerical simulations by Hill et al. [2001] known for showing good agreement in the transition between low and high particle Reynolds number flow at moderate particle volume fractions.

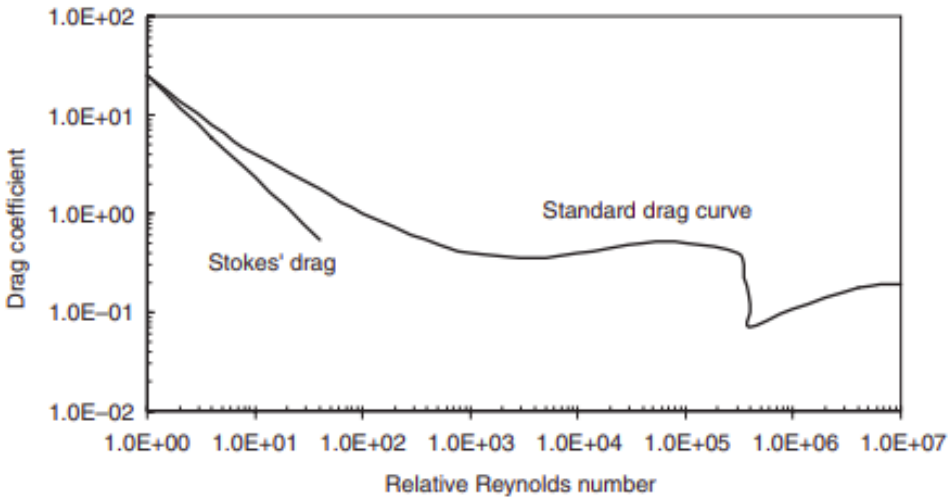

Figure 2.4: The standard drag coefficient curve for a spherical particle in steady flow [Crowe, 2005].

For the simulations performed in Chapter 5, a transitional drag model by Gidaspow [1994] is used which contains a combination of the Wen and Yu and Ergun drag correlations and switches between the two based on the particle volume fraction Lundberg and Halvorsen [2008]. The simulations mainly deals with dilute disperse flows leveraging the Wen and Yu model across the majority of the system. The Ergun drag model will only come into effect towards the boundary where the majority of the particle-wall collisions occur as the particles are more densely packed in this region.

Drag force used within the momentum equations to couple the fluid-solid interactions is defined by $\beta(u_p - u_f)$. The drag coefficient c_d requires the particle Reynolds number Re_p defined by

$$Re_p = \frac{\alpha_f \rho_f |\boldsymbol{u}_p - \boldsymbol{u}_f| d_p}{\mu_f}, \tag{2.14}$$

where $|\boldsymbol{u}_p - \boldsymbol{u}_f|$ is the mean relative velocity between the particle and the fluid, d_p the particle diameter, ρ_f the fluid density, α_f the fluid volume fraction and μ_f the fluid viscosity.

For fluid volume fractions of $\alpha_f \leq 0.8$, the Ergun drag law is used and the drag

coefficient β is defined as

$$\beta = 150\frac{\alpha_p^2\mu_f}{\alpha_f d_p^2} + 1.75\frac{\rho_f\alpha_p|\boldsymbol{u}_p - \boldsymbol{u}_f|}{d_p}. \tag{2.15}$$

The empirical Wen and Yu drag correlation is used for $\alpha_f > 0.8$ with the drag coefficient defined as

$$\beta = \frac{3}{4}C_d\frac{\alpha_f\alpha_p\rho_f|\boldsymbol{u}_p - \boldsymbol{u}_f|}{d_p}\alpha_f^{-2.65}, \tag{2.16}$$

where

$$C_d = \begin{cases} \frac{24}{Re}[1 + 0.15Re^{0.687}] & Re < 1000, \\ 0.44 & Re \geq 1000. \end{cases} \tag{2.17}$$

2.4.2 The Kinetic Theory of Granular Flow

In order to account for the the particle-particle interactions experienced in the 4-way coupling of this model. The concept of the kinetic theory approach of granular flow is adopted in this thesis. It is based on the kinetic theory of dense gases defined by Chapman [1970], where the approach is to model and describe densely packed macroscopic particles as microscopic molecules that are in constant random motion. Using this approach, the thermal temperature is replaced by a granular flow temperature and the temperature term is used to express the energy contained in the random motion of the particles [Cloete et al., 2012]. The theory assumes particles in a high particle volume fraction will exert a solid pressure which will prevent these particles becoming too densely packed together [Gidaspow, 1994].

Using the DDPM approach, the hybrid Eulerian-Lagrangian model uses the concept of KTGF to model particles as averaged quantities acting as a middle ground between the two fluid Eulerian-Eulerian model and DEM. This approach has the fluid solved on the fixed Eulerian grid and representative particles are tracked using the Lagrangian framework maintaining the discrete particle information whilst also being represented on the Eulerian grid as averaged quantities. The mapping of representative particles onto the Eulerian grid groups together a collection particles and models them as point particles travelling through the domain and cannot interact directly with each other as in DEM simulations. Therefore, the volume fraction

of particle phase is captured through the interpolation of the volume fraction that would be occupied by all the particles within the cell and mapped onto the Eulerian grid and particle particle interactions are modelled through the use of KTGF. This approach maintains the discrete particle information in an averaged sense, incorporates particle-particle interactions parameterisations using solid pressure, but also reduces computational cost compared to when achieving the same goal using DEM [Chen and Wang, 2014].

The sub-grid scale fluctuating of particle velocities around the mean particle velocity is based on Maxwell's velocity distribution function [Jenkins, 1992, Ding and Gidaspow, 1990]:

$$f\left(\boldsymbol{c}-\boldsymbol{u}_p\right) \propto \left(\frac{1}{2\pi\Theta}\right)^{\frac{3}{2}} \exp\left(-\frac{\left(\boldsymbol{c}-\boldsymbol{u}_p\right)\cdot\left(\boldsymbol{c}-\boldsymbol{u}_p\right)}{2\Theta}\right), \tag{2.18}$$

where $\boldsymbol{c}$ is the mean particle velocity from the Eulerian frame of reference and Θ the granular temperature analogous to the kinetic theory of gases defined by

$$\Theta = \frac{\left\langle \left\| \boldsymbol{c}-\boldsymbol{u}_p \right\|^2 \right\rangle}{3}. \tag{2.19}$$

From Equation 2.12, the solid stress tensor $\overline{\overline{\tau}}_p$ is modelled from the expression from Lun et al. [1984]

$$\overline{\overline{\tau}}_p = -p_p\mathbb{I} + \alpha_p\mu_p\boldsymbol{\nabla}^2\boldsymbol{u}_p + \alpha_p\left(\lambda_p - \frac{2}{3}\mu_p\right)\boldsymbol{\nabla}\cdot\boldsymbol{u}_p\mathbb{I}, \tag{2.20}$$

where μ_p is the shear viscosity, λ_p the bulk viscosity and $\boldsymbol{u}_p$ the average velocity vector.

The solid pressure, shear and bulk viscosity making up the solid stress tensor in Equation 2.20 are all calculated from the KTGF, and depends on the conservation of kinetic energy contained within these particles. This conservation of kinetic energy is known as the granular temperature provided in Equation 2.19

$\boldsymbol{u}_p$ in Equation 2.19 is the individual particle velocity, not averaged in the case of Eulerian-Eulerian simulations as we are not solving particles as a continuum. $\boldsymbol{c}$, the mean particle velocity is calculated as the average velocity.

The shear and bulk viscosity arises from the momentum exchange due to translation and collision between particles. The shear viscosity contains the kinetic and

collision part of the particle-particle momentum exchange, whereas the bulk viscosity accounts for the resistance of these particles to compression and expansion. The shear viscosity, μ_p, is composed of collisional and kinetic parts modelled using expressions from [Gidaspow, 1994]

$$\mu_p = \mu_{col} + \mu_{kin} \tag{2.21}$$

The collisional part of the shear viscosity, μ_{col}, is modelled as

$$\mu_{col} = \frac{4}{5}\alpha_p d g_0 (1+e)\left(\frac{\Theta}{\pi}\right)^{\frac{1}{2}}. \tag{2.22}$$

The kinetic part of the shear viscosity, μ_{kin}, is modelled as

$$\mu_{kin} = \frac{10\rho_p d\sqrt{\Theta\pi}}{96\alpha_p(1+e)g_0}\left[1+\frac{4}{5}g_0\alpha_p(1+e)\right]^2 \tag{2.23}$$

The bulk viscosity accounts for the resistance of the particles to compression and expansion has the below form from Lun et al. [1984]

$$\lambda_p = \frac{4}{3}\alpha_p^2\rho_p d g_0(1+e)\left(\frac{\Theta}{\pi}\right)^{\frac{1}{2}}, \tag{2.24}$$

where d is the particle diameter, e is the coefficient of restitution for particle collision. The solid pressure, p_p, modelled using expressions from Lun et al. [1984], Ding and Gidaspow [1990] is given as:

$$p_p = \alpha_p\rho_p\Theta + 2\rho_p(1+e)\alpha_p^2 g_0\Theta, \tag{2.25}$$

where g_0 is the radial distribution function given by

$$g_0 = \left[1-\left(\frac{\alpha_p}{\alpha_{max}}\right)^{\frac{1}{3}}\right]^{-1}. \tag{2.26}$$

The radial distribution function models the probability of collisions between particles at a given packing ratio and acts to resist the particles from becoming very densely packed. It is controlled by a maximum packing fraction α_{max} and is designed to grow large asymptotically as the solid volume fraction approaches this maximum packing fraction. This value is taken to be 0.6 from studies conducted by Ding and Gidaspow [1990].

For this thesis, the solid stress tensor given in Equation 2.20 has been simplified to only include the solid pressure term. It does not consider the resistance of particles to compression and expression, shear components of particle-particle collision or how they are moving relative to one another. Implementing the shear components requires the added complexity of calculating the local average strain rate for particles. The effects of these components are negligible as the vast proportion of the fluid considered in this thesis is dilute and shear stress is negligible when compared to the viscous drag associated with the particle-fluid interactions provided in Section 2.4.1. Particle-particle shear stress becomes significant at high particle volume fractions near the walls, however, the particle-particle behaviour of importance in this thesis is the ability to describe the behaviour of the particles slowing down as it approaches the wall due to the solid pressure mimicking the effect of particle-particle collisions close to the wall reducing the effects of particle-wall collisions.

2.4.3 Wear model

Introduced in Section 2.2.3 wear models consists of wear mechanisms composed of chemical, thermal and mechanical wear. For the scope of this thesis, a semi-mechanistic wear model based on contributions from cutting and deformation is selected and incorporated in the CFD-based wear modelling framework. Many different forms of wear equations exist in literature as discussed by Meng and Ludema [1995], these consists of empirical models based on experimental data and mechanistic models based on the physics and mechanisms of wear.

Other CFD-based wear prediction models include Chen et al. [2004], Zhang et al. [2007] and Agrawal et al. [2019]. Chen et al. [2004]'s model is based on a one-way coupled approach over a fixed computation mesh and the erosion ratio defined as the mass loss of the material divided by the mass of the particles impacting the wall is given by

$$ER = AF_s V^n f(\theta) \tag{2.27}$$

where A is an empirical constant derived for specific materials, V the particle impact velocity, n an empirical coefficient, F_s the particle sharpness factor and $f(\theta)$ the

function of impact angle derived from empirical constants based on the material being eroded. The particle rebound model used to describe particle-wall collision includes impact angle dependent coefficient of restitution based on empirical data, an example of this is that of Grant and Tabakoff [1975] and Forder et al. [1997].

Zhang et al. [2007] compared various CFD- based wear models against experimental data, the model is one-way coupled and no particle-particle interactions were considered. Through the results Zhang et al. [2007] showed that two empirically derived wear models had the best correlation with experimental data. These are give by the E/CRC erosion model and the erosion model of Oka and Yoshida [2005]. Furthermore, Zhang et al. [2007] stated that simulation results showed that the choice of rebound model and namely the treatment of the coefficient of restitution had little or no influence on particle trajectory and wear, thus contradicting the work of Chen et al. [2004].

Agrawal et al. [2019] created a one-way coupled wear model that is capable of mesh deformation based on the erosion rate calculated for each node. The same E/CRC erosion model as that of Zhang et al. [2007] was used and is given by

$$ER = C(BH)^{-0.59} F_s V_p^n F(\alpha) \tag{2.28}$$

where C is an empirical constant, BH the Brinell Hardness of the target material and α is the particle impact angle with function $F(\alpha)$ defined as

$$F(\alpha) = 5.4\alpha - 10.11\alpha^2 + 10.93\alpha^3 - 6.33\alpha^4 + 1.42\alpha^5. \tag{2.29}$$

One of the draw backs of the above CFD-based wear models is the choice of empirically derived wear equations, while it is easy to use, there are uncertainties in extrapolating these correlations for different material properties.

A semi-mechanistic impingement wear model by Arabnejad et al. [2015b] was determined to be the most suitable for use in this for the wear modelling framework. Arabnejad et al. [2015b]'s model is developed through a combination of mechanistic and empirical methods and considers mechanical wear for ductile materials from both cutting and deformation mechanisms. Target materials were selected based on the distribution density, hardness and their prevalence in the oil and gas industries.

Arabnejad et al. [2015b] was able to show the ratio of contact increased from 0.4 for sand particles to 1 for rounded glass beads, which in turn altered the angle dependency leading to higher impact angles for maximum wear. The particle sharpness factor alters the effectiveness of overall wear. Bahadur and Badruddin [1990] and Liebhard and Levy [1991] demonstrated that angular particles can cause up to an order of magnitude more wear than spherical particles.

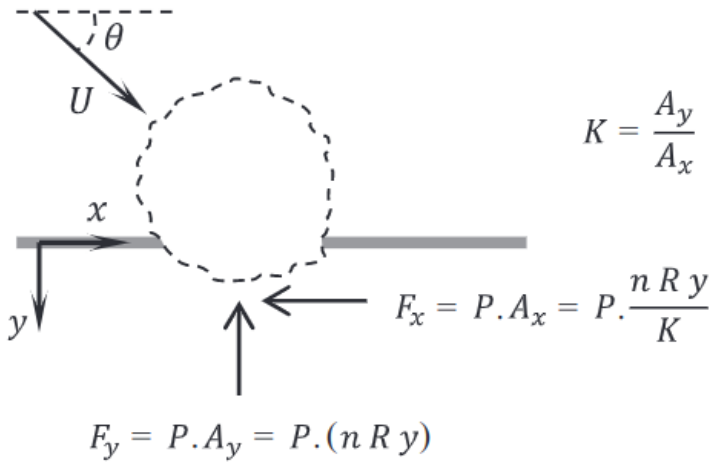

Figure 2.5: Force balance of a particle with an arbitrary shape cutting into a surface [Arabnejad et al., 2015b].

In addition, this model implements a novel approach where the particle shape has an influence on the ratio of contact parameter used to determine the critical impact angle. The ratio of contact (K) is obtained experimentally for each specific material with Figure 2.5 illustrating the forces that resists the particles as it cuts into the surface where K is the empirically defined ratio of vertical to horizontal contact area between the particle and the surface given by A_y and A_x respectively. This differs from Finnie and McFadden [1978]'s mechanistic model where ratio of contact is an assigned constant. F_y and F_x are the forces resisting the motion of particle with the equations of motion of the particle in the vertical and horizontal directions defined by Finnie and McFadden [1978] as:

$$m\frac{\mathrm{d}^2y}{\mathrm{d}t^2} = PnRy = 0 \tag{2.30}$$

$$m\frac{\mathrm{d}^2x}{\mathrm{d}t^2} + \frac{PnRy}{K} = 0 \tag{2.31}$$

where m is the mass of the particle, P the flow pressure of the material assumed to be the square root of the Vickers hardness of the material ($P = \sqrt{Hv}$), n the ratio of contact area to the removed area and R the particle size so that according to Hertz contact stress Andrews [1930]

$$A_y = 2\pi Ry. \tag{2.32}$$

Integrating both Equations 2.30 and 2.31 and using the inbound velocity and particle position gives

$$y = \frac{U\sin(\theta)}{\beta}\sin(\beta t) \tag{2.33}$$

$$x = tU\cos(\theta) - \frac{U\sin(\theta)[t\beta - \sin(\beta t)]}{K\beta}, \tag{2.34}$$

where θ is the impact angle, U the inbound velocity and $\beta = \sqrt{\frac{PnR}{m}}$.

Volumetric loss for wear observed from cutting is therefore

$$Vol_C = \int A_x dx = \frac{mF_sCU^{2.41}f(\theta)}{2\sqrt{Hv}}, \tag{2.35}$$

where C is the cutting coefficient, F_s the particle sharpness factor and the angle function $f(\theta)$ is given by Equation 2.36 and through experimentation $Vol_C \propto U^{2.41}$.

$$f(\theta) = \begin{cases} \frac{1}{2K^2}(K\sin(2\theta) - \sin^2(\theta)) & \theta \leq \tan^{-1}K \\ \cos(\theta)^2 & \theta \geq \tan^{-1}K. \end{cases} \tag{2.36}$$

The volumetric loss due to deformation is obtained from Bitter [1963] and is given as

$$Vol_D = \frac{1}{2}\frac{mF_sg(\theta)}{\epsilon}, \tag{2.37}$$

where ϵ is the deformation coefficient and the angle function for deformation erosion $g(\theta)$ defined as

$$g(\theta) = max(0, (U\sin(\theta) - U_{tsh})^2). \tag{2.38}$$

U_{tsh} is the threshold velocity determined from experimental data below which deformation erosion is considered negligible.

Total volume loss term for a given impact event when considering erosion from both cutting and deformation mechanisms is summarised as a combination of Equations 2.35 and 2.37. The equation can be written as

$$W_i = \frac{mF_s}{2}\left[\frac{U^{2.41}f(\theta)}{\sqrt{Hv}} + \frac{g(\theta)}{\epsilon}\right]. \tag{2.39}$$

The value of K is obtained through experimentation in this model is 0.4 for materials eroded with sand. The sharpness of the particle changes the effectiveness of the particle at causing volume loss at when colliding with the wall, therefore the sharpness factor F_s ranges from 0.25 for rounded particles to 1 for fully sharp particles.

For this thesis, it is important to note that mass transport due to wear has not been accounted for as including the material lost through wear would add significant computational cost and increases the complexity of the wear modelling framework with little gain as the magnitude of wear due to the amount of solids from the scoured surface is significantly lower than the magnitude of wear introduced by the flow. In addition, there would always be the limitation of the use of empirical data in the model equations as this would generate uncertainty in the results when trying to extrapolate the model to other material properties, while the wear equation used is based on a semi-mechanistic model, there still exist the need to rely on empirical data for certain material properties.

2.5 Summary of Equations

A summary of the equations used in this thesis is given below. Implementation of these equations as well as the assumptions made in creating the set of model equations, initial and boundary conditions are presented in Chapter 4.

1. Conservation of mass (E.q 2.5)

$$\boldsymbol{\nabla} \cdot (\alpha_f \boldsymbol{u}_f)(\alpha_p \boldsymbol{u}_p) = 0.$$

2. Conservation of momentum (Eq.2.9)

$$\frac{\partial(\alpha_f \rho_f \boldsymbol{u}_f)}{\partial t} + \boldsymbol{\nabla} \cdot (\alpha_f \rho_f \boldsymbol{u}_f \otimes \boldsymbol{u}_f) = -\alpha_f \boldsymbol{\nabla} p + \mu_f \boldsymbol{\nabla}^2 \boldsymbol{u}_f + \alpha_f \rho_f \boldsymbol{g} + K(\boldsymbol{u}_p - \boldsymbol{u}_f).$$

3. Particle equation of motion (Eq. 2.11)

$$\rho_p \frac{\mathrm{d}\boldsymbol{u}_p}{\mathrm{d}t} = \boldsymbol{g}(\rho_p - \rho_f) + \beta(\boldsymbol{u}_f - \boldsymbol{u}_p) + \boldsymbol{F}_{\boldsymbol{KTGF}},$$

where

$$\boldsymbol{F}_{\boldsymbol{KTGF}} = \boldsymbol{\nabla} p_p.$$

4. Particle position (Eq. 2.13)

$$\frac{\mathrm{d}\boldsymbol{x}_p}{\mathrm{d}t} = \boldsymbol{u}_p.$$

5. Fluid phase drag force (Eq. 2.10)

$$K(\boldsymbol{u}_p - \boldsymbol{u}_f) = \sum_{i=1}^{N} m_i \beta \frac{(\boldsymbol{u}_{p,i} - \boldsymbol{u}_f)}{V}.$$

6. Particle Reynolds number (Eq. 2.14)

$$Re_p = \frac{\alpha_f \rho_f |\boldsymbol{u}_p - \boldsymbol{u}_f| d_p}{\mu_f}.$$

7. Drag coefficient for $\alpha_f \leq 0.8$ (Eq. 2.15)

$$\beta = 150 \frac{\alpha_p^2 \mu_f}{\alpha_f d_p^2} + 1.75 \frac{\rho_f \alpha_p |\boldsymbol{u}_p - \boldsymbol{u}_f|}{d_p}.$$

8. Drag coefficient for $\alpha_f > 0.8$ (Eq. 2.16)

$$\beta = \frac{3}{4} C_d \frac{\alpha_f \alpha_p \rho_f |\boldsymbol{u}_p - \boldsymbol{u}_f|}{d_p} \alpha_f^{-2.65},$$

where

$$C_d = \begin{cases} \frac{24}{Re}[1 + 0.15 Re^{0.687}] & Re < 1000, \\ 0.44 & Re \geq 1000. \end{cases}$$

9. Solid pressure (Eq. 2.25)

$$p_p = \alpha_p \rho_p \Theta + 2\rho_p (1 + e) \alpha_p^2 g_0 \Theta,$$

where

$$g_0 = \left[1 - \left(\frac{\alpha_p}{\alpha_{max}} \right)^{\frac{1}{3}} \right]^{-1},$$

$$\Theta = \frac{\left\langle \|\boldsymbol{c} - \boldsymbol{u}_p\|^2 \right\rangle}{3}.$$

10. Wear equation (Eq. 2.39)

$$W_i = \frac{\rho_p F_s}{2}\left[\frac{U^{2.41} f(\theta)}{\sqrt{Hv}} + \frac{g(\theta)}{\epsilon}\right],$$

where

$$f(\theta) = \begin{cases} \frac{1}{2K^2}(K\sin(2\theta) - \sin^2(\theta)) & \theta \leq \tan^{-1} K \\ \cos(\theta)^2 & \theta \geq \tan^{-1} K. \end{cases}$$

$$g(\theta) = max(0, U\sin(\theta) - U_{tsh}).$$

Chapter 3

Numerical methods

Contents

3.1 Overview

This chapter covers the numerical methods required in the computational aspects of multiphase flow modelling. As the governing equations described in section 2.3 cannot typically be solved analytically, a numerical method is required to form an approximation of the exact solution. This chapter begins with the discussion of the discretisation methods used within this work to convert PDEs into discrete equations that are solvable computationally. In section 3.2 the numerical discretisation methods using the continuous Galerkin (CG), the discontinuous Galerkin (DG) and the control volume (CV) finite element methods for spatial discretisation are discussed using the advection-diffusion equation as a representative equation. Temporal discretisation using the theta-scheme is then described in section 3.3. An outline of the linear solvers used to obtain the solution to the discretised equations are presented in section 3.4. Finally, the process of mesh adaptivity used within Fluidity is described in section 3.5 as the application of mesh adaptivity is crucial to this thesis.

3.2 Spatial Discretisation

In order to demonstrate the Galerkin finite element and control volume discretisations, the standard advection-diffusion in its conservative form will be used as a representative equation in this chapter. The governing equations used within this thesis can be applied using the same principles as described for advection-diffusion. The discretisation to the Navier-Stokes equation is very similar to that of the advection-diffusion equation represented below as the key terms in the Navier-Stokes equation represents the advection and diffusion of momentum, the description of which will be provided at the end of the section.

The advection-diffusion equation can be written as [Elman, 2014]:

$$\frac{\partial c}{\partial t} + \boldsymbol{\nabla} \cdot \boldsymbol{u} c - \boldsymbol{\nabla} \cdot (\overline{\overline{k}} \boldsymbol{\nabla} c) = 0 \tag{3.1}$$

where c is the unknown scalar, $\boldsymbol{u}$ is the velocity vector and $\overline{\overline{k}}$ is the diffusivity tensor.

3.2.1 Galerkin Finite Element method

The aim of the Galerkin finite element method is to take differential equations where solutions exists in an infinitely large problem space and transform them into discrete linear equations where the solution can be approximated by a computer over a finite subspace defined by a mesh. This choice of method for solving multiphase flows is preferred over the finite difference method as it makes few assumptions over the the structure of the underlying mesh, making it more suitable for problems with unstructured meshes [Zienkiewicz, 2014].

The first step in the finite element method is to write Equation 3.1 in its weak form. This is achieved by first multiplying both sides with a test function $\boldsymbol{w}$ before integrating over the space domain Ω [Zienkiewicz, 2013].

$$\int_{\Omega} \boldsymbol{w} \left(\frac{\partial c}{\partial t} + \boldsymbol{\nabla} \cdot \boldsymbol{u}c - \boldsymbol{\nabla} \cdot (\overline{\overline{k}} \boldsymbol{\nabla} c) \right) = 0 \tag{3.2}$$

Integrating 3.2 by parts and using the divergence theorem gives

$$\int_{\Omega} \boldsymbol{w} \frac{\partial c}{\partial t} - \boldsymbol{\nabla} \boldsymbol{w} \cdot \boldsymbol{u}c + \boldsymbol{\nabla} \boldsymbol{w} \cdot \overline{\overline{k}} \cdot \boldsymbol{\nabla} c + \int_{\delta\Omega} \boldsymbol{w} (\boldsymbol{n} \cdot \boldsymbol{u}c - \boldsymbol{n} \cdot \overline{\overline{k}} \cdot \boldsymbol{\nabla} c) = 0 \tag{3.3}$$

where $\boldsymbol{n}$ is the outward facing unit normal vector to $\delta\Omega$. As $\boldsymbol{w} \in H^1(\Omega)$ where $H^1(\Omega)$ is the first-order Sobolev space and the highest (weak) derivative of the scalar field c in equation 3.3 is first order, it justifies the search of a solution to the field c to be within the same Sobolev space [Elman, 2014].

Rather than searching the entire Sobolev space for a solution to the weak form. Finite element discretisation restricts the space of the solution to a finite-dimensional subspace where the test function $\boldsymbol{w}$ and the field c can be written as a linear combination of basis functions such that

$$\boldsymbol{w} = \sum_{i=1}^{N} \phi_i \boldsymbol{w}_i, \tag{3.4}$$

$$c = \sum_{j=1}^{N} \phi_j c_j, \tag{3.5}$$

where N is the total number of solution nodes and $\boldsymbol{w}_i$ and c_j are values of the test function and solution for field c at nodes i and j respectively. In addition, basis functions are defined such that ϕ_k has a value of one at node k and zero at all other nodes giving $c_i = c(x_i)$ [Elman, 2014]. As the test function and solution are chosen to use the same basis functions from the same Sobolev space, this results in the so-called Galerkin finite element method.

The basis functions used within Fluidity are taken as piecewise continuous and piecewise discontinuous polynomial functions and have a narrow support which allows them to act as interpolating functions [Imperial College London, 2014].

Substituting equations 3.4 and 3.5 into 3.3, and using the fact that $\boldsymbol{w}_i$ is arbitrary [Zienkiewicz, 2013] gives the discretised version of the advection-diffusion equation in the weak form.

3.2.2 Continuous Galerkin discretisation

In the case of continuous Galerkin discretisation, continuous basis functions are chosen. Figure 3.1 shows the piecewise-linear (P1) and piecewise-quadratic (P2) basis functions along with the support nodes for one and two dimensional meshes. If the solution to 3.3 is satisfied for all basis functions ϕ_i then the discretised version of the weak form advection-diffusion equation becomes

$$\begin{aligned}\sum_{j}^{N_{nodes}} \left\{ \int_{\Omega} \phi_i \phi_j \frac{\partial c_j}{\partial t} - \boldsymbol{\nabla}\phi_i \cdot \boldsymbol{u}\phi_j c_j + \boldsymbol{\nabla}\phi_i \cdot \bar{\bar{k}} \cdot \boldsymbol{\nabla}\phi_j c_j \right\} + \\ \sum_{j}^{N_{nodes}} \left\{ \int_{\delta\Omega} \phi_i (\boldsymbol{n} \cdot \boldsymbol{u}\phi_j c_j - \boldsymbol{n} \cdot \bar{\bar{k}} \cdot \boldsymbol{\nabla}\phi_j c_j) \right\} = 0, \, for \, all \, \phi_i.\end{aligned} \tag{3.6}$$

This discretised advection-diffusion equation gives a systems of linear equations that can be solved once appropriate time discretisation has been applied. For simplicity, assuming the boundaries are closed and applying Neumann boundary conditions such that $\boldsymbol{u} \cdot \boldsymbol{n} = 0$ and $\frac{\partial c}{\partial n} = 0$. We obtain the following written in matrix form

$$M\frac{\partial \underline{c}}{\partial t} + A(\boldsymbol{u})\underline{c} + K\underline{c} = 0, \tag{3.7}$$

where M, A and K are matrices

$$M_{ij} = \int_\Omega \phi_i \phi_j, A_{ij} = -\int_\Omega \boldsymbol{\nabla}\phi_i \cdot \boldsymbol{u}\phi_j, K_{ij} = \int_\Omega \boldsymbol{\nabla}\phi_i \cdot \overline{\overline{k}} \cdot \boldsymbol{\nabla}\phi_j. \tag{3.8}$$

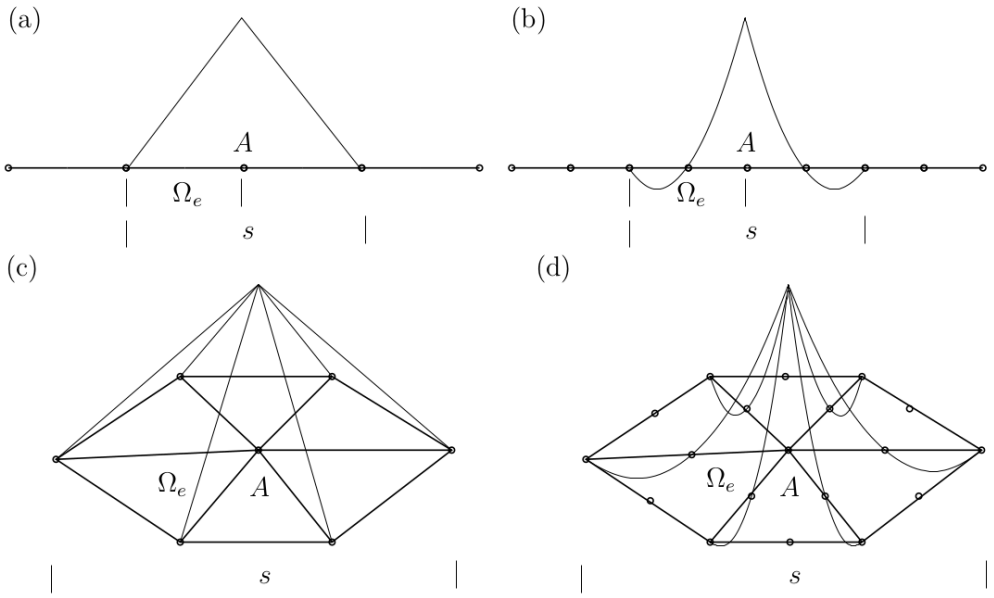

Figure 3.1: One-dimensional (a,b) and two-dimensional (c,d) schematics of piecewise linear (a,c) and piecewise quadratic (b,d) continuous basis functions and their support, s, which extends to all elements surrounding node A. The basis function has a value of 1 at node A and 0 at all surrounding nodes with the number of nodes per element Ω_e depends on the polynomial order. [Wilson, 2009]

Stabilisation

It is known that a continuous Galerkin discretisation of an advection-diffusion equation can result in truncation errors in the form of a diffusion operator when dealing with flows dominated with high advection. The truncation error in the advection term can lead to a negative diffusivity term. This results in the grid Péclet number becoming greater than one making the discretisation unstable. In order to achieve stability, stabilisation methods can be applied or model resolution increased to reduce the grid Péclet number.

An example of the stabilisation method Fluidity implements is the streamline-upwind Petrov-Galerkin (SUPG) method. The SUPG method is a consistent scheme

which introduces stabilisation in the form of a weighed residual which is equivalent to replacing test function $\boldsymbol{w}$ with $\hat{\boldsymbol{w}} = \boldsymbol{w} + \tau P(\boldsymbol{w})$ where τ is some stabilisation parameter and $P(\boldsymbol{w})$ some operator [Donea and Huerta, 2003, Imperial College London, 2014].

3.2.3 Discontinuous Galerkin discretisation

The discontinuous Galerkin discretisation shares a similar approach to the continuous discretisation method, however, the solution nodes are not shared across the element boundaries resulting in each element being its own isolated problem. Thus, the surface integral needs to be evaluated across all elements and not just those along the mesh boundary. As a result, solutions does not have to be continuous across all the edges, it has the property of being locally mass conservative offering more flexibility allowing for higher order local approximations. Figure 3.2 shows the piecewise-linear ($\mathrm{P1_{DG}}$) and piecewise-quadratic ($\mathrm{P2_{DG}}$) basis functions along with the support nodes for one and two dimensional meshes.

Within an arbitrary individual element, the weak form of the advection-diffusion equation using the discontinuous Galerkin discretisation becomes:

$$\int_{\Omega_{e_i}} \boldsymbol{w}\frac{\partial c}{\partial t} - \boldsymbol{\nabla w}\cdot\boldsymbol{u}c + \boldsymbol{\nabla w}\cdot\bar{\bar{k}}\cdot\boldsymbol{\nabla}c + \int_{\delta\Omega_{e_i}} \boldsymbol{w}(\widehat{\boldsymbol{n}\cdot\boldsymbol{u}c} - \boldsymbol{n}\cdot\widehat{\bar{\bar{k}}\cdot\boldsymbol{\nabla}c}) = 0, \quad for\ i = 1, ..., N_e, \tag{3.9}$$

where Ω_{e_i} is the element volume, N_e is the total number of elements and the hatted terms represents the advection and diffusion flux terms.

As communication between elements occur through the flux terms, these needs to be well defined along each element face. In this work, Fluidity supports the use of a upwinding scheme to define the advective flux. The average value for velocity is used between each side of the face and the value of c is taken to be the upwinded value [Wilson, 2009]. For the diffusive flux, the Bassi-Rebay scheme is used [Bassi and Rebay, 1997].

The choice of the order of basis functions determines the velocity and pressure element pairs. An example is the $\mathrm{P1}_{DG}$-P2 element pair used in this thesis due to its

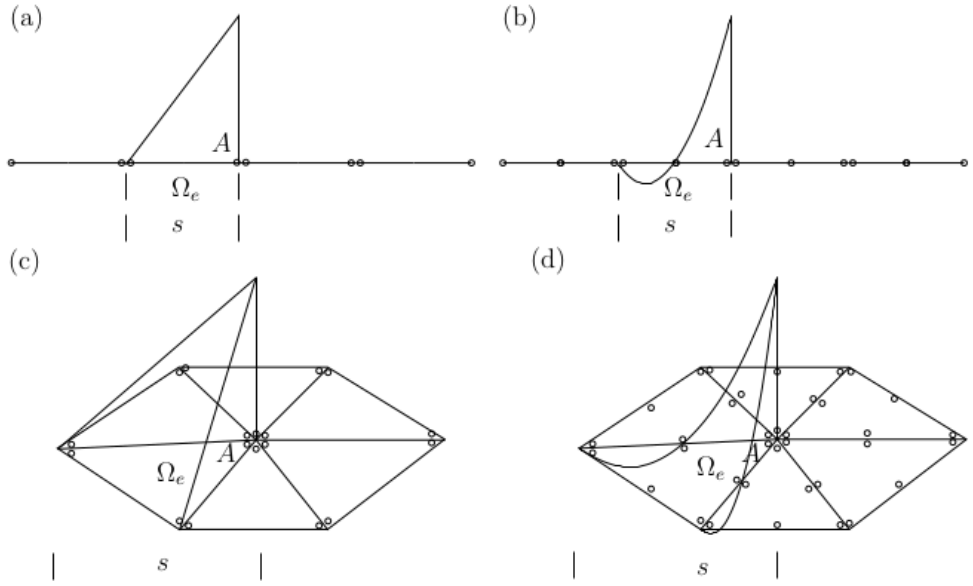

Figure 3.2: One-dimensional (a,b) and two-dimensional (c,d) schematics of piecewise linear (a,c) and piecewise quadratic (b,d) discontinuous basis functions and their support, s, which extends to all elements surrounding node A. The basis function has a value of 1 at node A and 0 at all surrounding nodes with the number of nodes per element Ω_e depends on the polynomial order. [Wilson, 2009]

numerical stability properties [Cotter et al., 2009]. $\mathrm{P1}_{DG}$ denotes that piecewise discontinuous linear polynomial basis functions are used to represent the velocity field while P2 denotes that piecewise continuous quadratic polynomial basis functions are used to represent the pressure field.

3.2.4 Control volume

In addition to CG and DG discretisation methods, Fluidity also supports the use of control volume discretisation with the advection-diffusion equation and scalar fields. This method is used to discretise the particle volume fraction within this thesis as control volume methods can guarantee a bounded, explicitly conservative solution [Wilson, 2009]. This property is important for fields like the particle volume fraction where a positive solution is required.

As per the Galerkin finite element method, the advection-diffusion equation is

first transformed from the strong form (3.1)into its weak form (3.3). A dual mesh is constructed from the original mesh to define the control volumes centered around the parent node in the original finite element mesh as seen in Figure 3.3. Across each control volume, the test and field solution are chosen to be piecewise constant. The basis function in the control volume discretisation has a value of 1 inside the control volume and zero elsewhere.

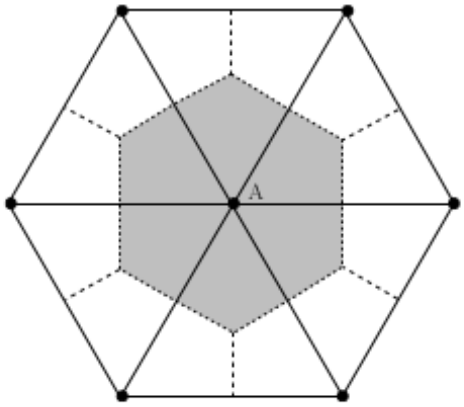

Figure 3.3: A two-dimensional control volume (shaded grey). Back lines denotes the original finite element mesh with nodes represented by black circles. Dashed lines denote the dual control volume mesh with the shaded grey area denoting the control volume for central node A. [Hiester, 2012]

Similar to DG discretisation, the weak form of the CV discretisation can be written as

$$\int_{\Omega_{v_i}} \boldsymbol{w}\frac{\partial c}{\partial t} - \boldsymbol{\nabla w}\cdot\boldsymbol{u}c + \boldsymbol{\nabla w}\cdot\bar{\bar{k}}\cdot\boldsymbol{\nabla}c + \int_{\delta\Omega_{v_i}} \boldsymbol{w}(\widehat{\boldsymbol{n}\cdot\boldsymbol{u}c} - \boldsymbol{n}\cdot\widehat{\bar{\bar{k}}\cdot\boldsymbol{\nabla}c}) = 0, \quad for\ i = 1, ..., N_v, \tag{3.10}$$

where N_v is the total number of control volumes (equal to the number of parent FE nodes) and the hatted terms represents the advection and diffusion flux terms across the volume boundaries.

Using the properties of the CV basis functions and the fact that the test function $\boldsymbol{w}$ is arbitrary [Jacobs, 2013], equation 3.10 can be simplified down to

$$\frac{\partial c_v}{\partial t}\int_{\Omega_v} 1 dV + \int_{\delta\Omega_v} \widehat{\boldsymbol{n}\cdot\boldsymbol{u}c_v} - \boldsymbol{n}\cdot\widehat{\bar{\bar{k}}\cdot\boldsymbol{\nabla}c_v} dS = 0. \tag{3.11}$$

Like the DG method, advection and diffusion terms needs to be well defined along the control volume boundary. Unlike DG, the velocity $\boldsymbol{u}$ is continuous on the control volume boundary and this boundary lies within the original finite element mesh, therefore, it is only necessary to describe how the face value of c is defined. Within Fludity, many different methods for advective flux discretisation are supported for CV methods. An indepth discussion of these methods can be found in Imperial College London [2014].

Two diffusive flux discretisations are supported within Fluidity; an element gradient approach and the Bassi-Rebay method. The element gradient method estimates the gradient of c on the CV boundary using the fact that the CV boundary intersects the parent elements where the parent FE basis functions are continuous. The Bassi-Rebay method is similar to that of the one used for DG discretisation.

3.2.5 Discretisation of the Navier-Stokes equation

The discretisation of the incompressible Navier-Stokes equation used in this thesis is similar to that of the advection-diffusion equation used as a representative example. The description of the discretised Navier-Stokes equation is provided as follows

$$\boldsymbol{M}\boldsymbol{u}_f + \boldsymbol{A}\boldsymbol{u}_f - \boldsymbol{K}\boldsymbol{u}_f - \boldsymbol{C}p = \boldsymbol{b} + \boldsymbol{F} \tag{3.12}$$

where matrices $\boldsymbol{M}$, $\boldsymbol{A}$, $\boldsymbol{K}$, $\boldsymbol{C}$ and $\boldsymbol{F}$ are the mass, advection, stress, gradient and drag force matrices and vector $\boldsymbol{b}$ represents the gravitational force. Their components are defined as

$$\boldsymbol{M}_{ij} = \int_\Omega \phi_i \rho_f \phi_j, \tag{3.13}$$

$$\boldsymbol{A}_{ij} = \int_\Omega \boldsymbol{\nabla}\phi_i \cdot \rho_f \boldsymbol{u}_f \phi_j, \tag{3.14}$$

$$\boldsymbol{K}_{ij} = \int_\Omega \boldsymbol{\nabla}\phi_i \cdot \mu \boldsymbol{\nabla}\phi_j, \tag{3.15}$$

$$\boldsymbol{C}_{ij} = \int_\Omega \phi_i \alpha_f \boldsymbol{\nabla}\psi_j, \tag{3.16}$$

$$\boldsymbol{F}_{ij} = \int_{\Omega} \phi_i \beta \phi_j, \tag{3.17}$$

$$\boldsymbol{b} = \int_{\Omega} \phi_i \alpha_f \rho_f \boldsymbol{g}. \tag{3.18}$$

3.3 Temporal Discretisation

A θ timestepping scheme is used to discretise all model equations within Fluidity. For this thesis, an implicit, first order accurate time discretisation is performed ($\theta_t = 1$). Taking an example equation for some field c and function f, an equation of the form

$$\frac{\partial c}{\partial t} = f(c, t) \tag{3.19}$$

is discretised as

$$\frac{c^{n+1} - c^n}{\Delta t} = f(c^{n+\theta_t}, t^{n+\theta_t}) \tag{3.20}$$

where $c^{n+\theta_t}$ is defined as $c^{n+\theta_t = \theta_t c^{n+1} + (1-\theta_t)c^n}$ with $\theta_t \in [0, 1]$, n denotes the current time step and Δt denotes the time-step size [Ferziger, 2002].

3.4 Linear Solvers

Discretised equations, such as equation 3.7, form a system of linear equations that can be written in the form $\boldsymbol{A}\underline{x} = \underline{b}$, which can then be solved for an unknown $\underline{x}$. There are two methods of solving these linear systems, using either direct methods or iterative methods. Direct methods are typically more computationally expensive for large systems when compared to iterative methods. In addition, matrices corresponding to finite element systems are generally sparse, resulting in a dense inverse matrix requiring more storage in memory [Zienkiewicz, 2013]. Thus, iterative methods are chosen to solve such system of equations.

Iterative methods solve a linear system using a sequence of approximations $\underline{x}^k$ such that it converges to the exact solution $\underline{x}$. The iterations are repeated until the residual $\mid \underline{x}^k - \underline{x} \mid$ is within the user specified tolerance.

Within Fluidity, an external open-sourced library, PETSc, is used to solve these linear systems. PETSc consists of a range of parallelised iterative methods and pre-

conditioners which aims to make the matrix $\boldsymbol{A}$ easier to solve [Balay et al., 2016]. Throughout this thesis, a generalised minimal residual method (GMRES) [Saad and Schultz, 1986] solver with a successive over-relaxation (SOR) preconditioner are used for both the velocity and wear fields and a conjugate gradient [Hestenes and Stiefel, 1952] solver with a multigrid preconditioner [Kramer et al., 2010] are used for the pressure field. User specified relative tolerance is set to 10^{-7} with number of maximum iterations set to 1000.

3.5 Mesh Adaptivity

Mesh adaptivity or adaptive mesh refinement is a technique to find an accurate and computationally effective way to represent the flow dynamics as time progresses by optimising the mesh at given intervals such that resolution is placed where necessary. This will provide good accuracy of small-scale flow dynamics without the need for a high mesh resolution throughout the domain.

Fluidity carries out mesh adaptivity to specific solution fields achieved through the use of an interpolation-based method that creates a metric which guides the mesh adapt via the Hessian. The metric is then adapted and the mesh modified until a specified tolerance is reached.

The process of mesh adaptivity can be divided into three main operations [Imperial College London, 2014]:

- Metric formation - defining the mesh required and criteria on adaptivity.
- Mesh optimisation - optimising the mesh for the current state based on the metric.
- Interpolation - transferring all fields from the old to the new mesh.

Each of these steps will be described in the subsections that follow.

For this thesis, mesh adaptivity was utilised to allow surface mesh movement and to describe boundary deformation in response to wear in 2D and 3D. Boundary deformation using mesh adaptivity is based on the grid velocity for the wear velocity field. The libmba2d library was used for 2D [Vasilevskii and Lipnikov, 1999] and the

libadaptivity library used in 3D [Pain et al., 2001]. The adaptive mesh functionality was taken fully from the Fluidity framework with no new functionality regarding mesh adaptivity developed within as part of this thesis. Full description of a typical adaptive time loop through the use of the lock-exchange example is provided within the Fluidity manual [Imperial College London, 2014]

3.5.1 Metric formation

The first step in mesh adaptivity within Fluidity is the construction of a metric, M, which controls the interpolation error of the field being adapted. This metric contains information of the system that defines the criteria for the generation of a new mesh. Within Fluidity, mesh optimisation method is used and the aim of mesh optimisation is to form a mesh $\mathcal{M}$ with edges $\boldsymbol{v}$ such that

$$\|\boldsymbol{v}\|_M = \sqrt{\boldsymbol{v}^T M \boldsymbol{v}} = 1, \ for\ all\ \boldsymbol{v} \in \mathcal{M}. \tag{3.21}$$

Therefore, all edges in the mesh will have unit length when measured against the metric, thus the metric is crucial in how the mesh adapts and where resolution placed [Hiester, 2012].

The metrics can be divided into three categories based on their choice of norms, these are referred to as the absolute metric based on the L_∞ norm, the relative metric based on a relative user defined interpolation error of the L_∞ norm, and the p-metric based on the L_p norm. In Fluidity, functionality for all 3 choices of metrics are available, however, only the absolute metric was implemented within this thesis and will be described below, all other metric formulations can be found in the Fluidity manual [Imperial College London, 2014].

The absolute metric is based on a modified Hessian and takes the form

$$M = \frac{|H|}{\varepsilon} \tag{3.22}$$

where ϵ is the user defined target interpolation error and the modified Hessian $|H|$ is defined as

$$|H| = Q^T |\Lambda| Q, \quad |\Lambda|_{ij} = \begin{cases} |\lambda_i| & i = j \\ 0 & i \neq j \end{cases} \tag{3.23}$$

with $\{\lambda_i\}$ the eigenvalues of Hessian H and Q the corresponding matrix of normalised eigenvectors [Pain et al., 2001]. When using the absolute metric for mesh adaptivity, maximum and minimum edge lengths needs to be specified in order to place a restriction on $\{\lambda_i\}$. This restriction mitigates the risk of infeasible values of edge lengths [Hiester, 2012].

3.5.2 Mesh optimisation

For a given metric from Section 3.5.1, there are then 3 main methods to generate a mesh that could satisfy this metric. These methods are global remeshing, local remeshing and mesh optimisation. Global remeshing creates an entirely new mesh on the same domain that satisfies the sizing requirements using an automatic mesh generator. Local remeshing is a method where cavities of elements are removed and then the whole is remeshed, the cavities are identified by measuring their conformance to the sizing requirements. Finally, there is mesh optimisation which deforms the previous mesh to the new mesh through a sequence of local operations defined by the functional (determining the quality of the element) and the set of operators the algorithm can perform. Detailed discussion of these approaches can be found in Farrell [2009].

Within Fluidity, mesh optimisation is used to generate a new mesh to satisfy the metric. The goal of mesh optimisation for the current state is to optimise the mesh based on the criteria given in 3.21. The mesh is optimised through a series of local topological operations, each type of operation is described below and illustrated in figures 3.4 and 3.5.

- **Node insertion** - also known as edge splitting where an additional node is inserted at the midpoint of an edge. This creates new elements and increases numerical resolution.

- **Node deletion** - also known as edge collapsing where a node is removed from an element, merging the elements and decreasing numerical resolution of the mesh.

- **Edge swapping** - the number of nodes are preserved in this operation, but an edge is connected to a different pair of nodes, changing the edge lengths and element shape. Can be conducted in 2D when performed on two elements and in 3D when performed on four elements.
- **Node movement** - the number of nodes are preserved but the position of the node is moved such that the quality of the surrounding elements are improved.
- **Face to edge swapping** - only available for 3D elements where a face can be converted to an edge (and vice versa) on a tetrahedron.

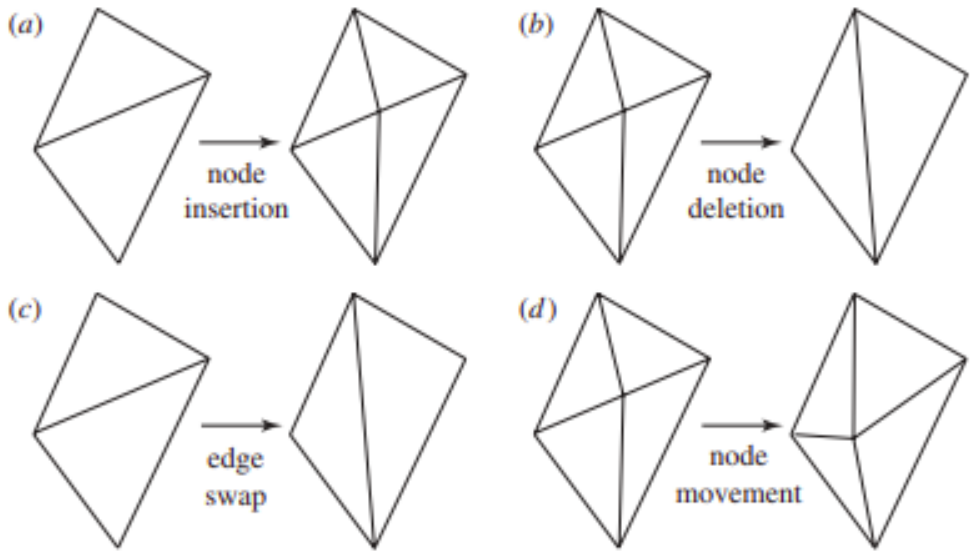

Figure 3.4: Topological operations used to optimise the mesh in two dimensions. (a) node insertion, (b) node deletion, (c) edge swap and (d) node movement. [Piggott et al., 2009]

3.5.3 Interpolation

Once the mesh adaptivity step has occurred, the solution field will need to be interpolated between the pre and post adapt meshes. Within Fluidity, many interpolation scheme can be used and can be referenced in the Fluidity manual [Imperial College London, 2014]. The work presented in this thesis adopts the use of consistent interpolation, a linear interpolation scheme.

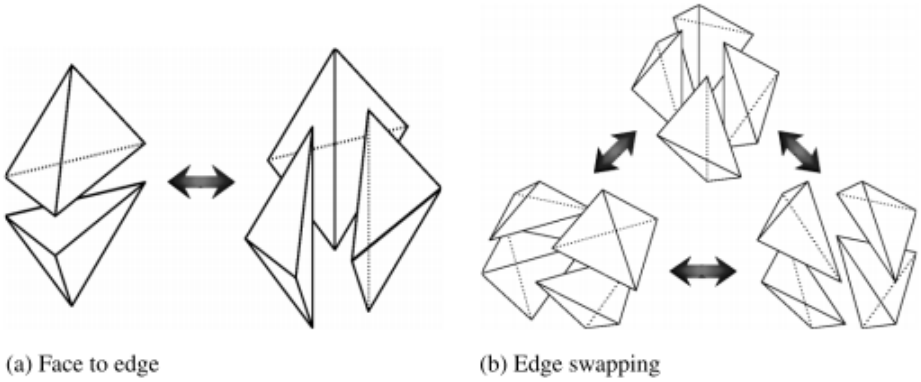

Figure 3.5: Diagram depicting (a) face to edge and edge to face swapping and (b) edge to edge swapping of 4 elements in three dimensions. [Pain et al., 2001]

Consistent interpolation transfers the data between mesh I and mesh II by using the solution nodes from the post adapt mesh as interpolation points and the underlying basis functions of each fields as the interpolants as described in figure 3.6. Mesh I was designed to be the optimal mesh when the last mesh optimisation was performed but still contains the up to date information of the fields at the current time and mesh II is the newly created mesh designed to be optimal for current condition of the fields. This scheme was chosen due to its simplicity to implement whilst producing fast and bounded results with low computational cost when compared to other methods available within Fluidity, however interpolating between the two meshes creates the disadvantage that the scheme is not explicitly conservative [Wilson, 2009].

3.6 Conclusion

In this chapter, the discretisation methods used to convert PDEs into discrete equations that can be solved computationally was presented. The continuous Galerkin, the discontinuous Galerkin and the control volume finite element methods were presented using the advection-diffusion equation as a representative example. These methods were used to discretise the fluid velocity and pressure field in the form of the $P1_{DG}$-P2 element pair with the control volume method used to calculate the

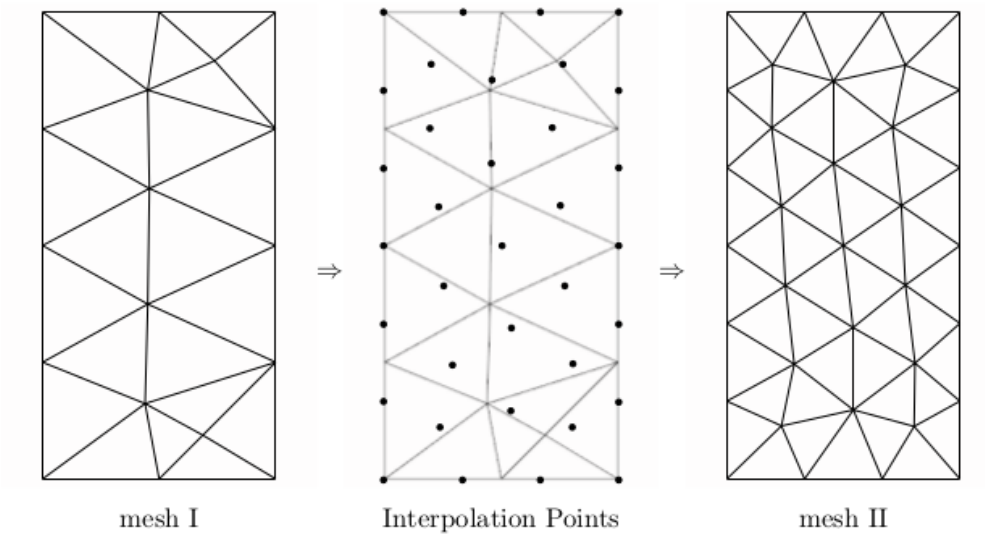

Figure 3.6: Consistent interpolation of a piecewise linear continuous field. Field data are interpolated from mesh I onto the nodal points of mesh II. [Wilson, 2009]

particle volume fraction. The discontinuous Galerkin method is computationally more expensive as the surface integral needs to be evaluated across all elements since the solution does not have to be continuous across the edges. However, this provides more flexibility and allows for higher order approximations locally. Temporal discretisation in the form of the implicit backward Euler ($\theta = 1$) used within this thesis was introduced. Finally the steps involved in mesh adaptivity used within this thesis to both optimise the mesh as well as deform the surface mesh in response to wear was presented.

Chapter 4

The Wear Modelling Framework

Contents

4.1 Overview

This chapter describes the particle laden wear modelling framework developed within Fluidity coupled with a Python based Lagrangian particle module. The model equations described in Chapter 2 are modified where necessary based on the assumptions within the wear modelling framework. Additional equations for the interpolation of wear rates for a given impact event, particle rebound velocity and particle scaling factor are introduced. The solution method and the discretisation of the particle module are described. Verification of the model was conducted in the form of a mesh and time convergence study on a static domain. The model was validated against two test cases, the first being particle settling under gravity validating the particle-fluid coupling against analytical solutions and the second being a jet impingement simulation confirming the qualitative verification that all the components of the framework combined shows the expected behaviour of boundary deformation in response to wear.

4.2 Model Equations

The governing equations describing the motion of the fluid, particles and their interaction terms used within the wear model are summarised in Section 2.5. Additional equations specific to the development of the wear model are provided here along with the assumptions made based on the problems considered within this thesis and described in each of the sections below.

4.2.1 Wear smoothing

The model uses a representative particles approach where only a representative portion of the actual number of particles are present in each control volume within the domain. In each wear impact event derived from Section 2.4.3 would therefore need to be smoothed out in time and space as there are far fewer particles than there are in the real system. This is achieved through the use of a damped diffusive

equation for the wear defined by Equation 2.39.

The damped diffusive equation for the wear experienced at the boundary is

$$\frac{\partial w}{\partial t} + \boldsymbol{\nabla} \cdot \kappa_{wear} \boldsymbol{\nabla} w = -\lambda \left[w + \sum_{i=1}^{N_{collisions}} W_i \delta(t - t_i) \delta(\boldsymbol{x} - \boldsymbol{x}_i) \right], \tag{4.1}$$

where κ_{wear} is the pseudo-diffusivity for the volume loss for the wear experienced, λ is the damping frequency and W_i's are impulsive wear source terms derived from the wear equation. κ_{wear} and λ are used to spread the point-wise wear source terms out in time and space respectively.

Integration of 4.1 gives the analytical solution of the wear profile of a single collision ($n = 1$)

$$w(\boldsymbol{x}, t) = \frac{\lambda W_i}{4\pi\kappa(t - t_i)} \exp\left(-\frac{|\boldsymbol{x} - \boldsymbol{x}_i|^2}{4\kappa(t - t_i)} - \lambda(t - t_i) \right). \tag{4.2}$$

An illustrative example of a normalised wear profile following a Gaussian distribution for a selection of $\frac{\kappa}{\lambda}$ values can be observed in Figure 4.1. The larger the choice of κ, the smoother the wear profile. This smoothness is reduces the effect of under sampling the total number of particles in the system due to the use of representative particles. However, this also reduces the sensitivity of the model to genuine variance predicted using the wear model.

4.2.2 Particle collision and rebound

When tracking particle trajectory for the simulation of wear, the framework needs to understand when a collision event has occurred between a particle and the system boundary and calculate the rebound trajectory needed for the wear equation. In order to verify when a collision event between a particle and the system boundary has occurred, a linearised search path is used to test for the intersection between the position of the particle and the boundary. This is denoted by the definition of particle position as a line segment

$$\boldsymbol{r} = (1 - s)\boldsymbol{r}^n + s\boldsymbol{r}^{n+1}, s \in [0, 1], \tag{4.3}$$

where n and $n + 1$ are the time steps immediately before and after the collision event and s the parametric distance between 0 and 1 along the line representing the

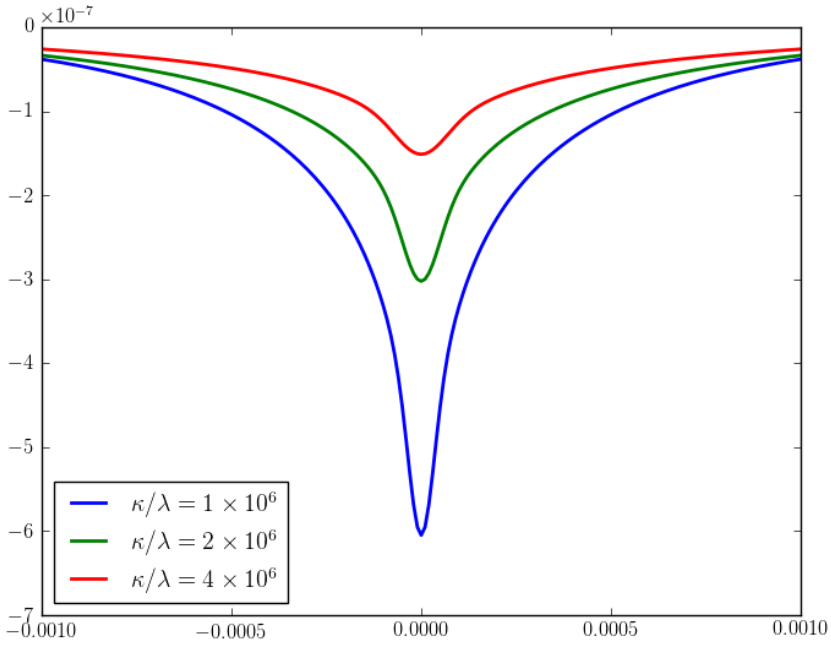

Figure 4.1: Wear profiles from a single impact event for different choices of parameter $\frac{\kappa}{\lambda}$.

intersection point. Should a collision event occur, the appropriate particle rebound velocity and trajectory needs to be accurately updated in order to account for future particle-fluid and particle-wall interactions. To achieve this, particle collisions with the boundary of the domain are assumed to be near elastic, such that the velocity of a particle immediately after a collision is given by

$$\boldsymbol{v}_{out} = \boldsymbol{v}_{in} - (1+e)(\boldsymbol{v}_{in} \cdot \boldsymbol{n})\boldsymbol{n}, \tag{4.4}$$

where $\boldsymbol{n}$ is the unit vector normal to the boundary and e the coefficient of restitution. $\boldsymbol{v}_{in}$ is the particle velocity immediately before a collision event which is given by

$$\boldsymbol{v}_{in} = (1-s)\boldsymbol{v}^n + s\boldsymbol{v}^{n+1}, s \in [0,1]. \tag{4.5}$$

Figure 4.2 shows an illustrative example of the particle rebounding off a domain boundary after approaching at an angle of θ.

For simplicity, and through the investigation performed by Zhang et al. [2007], the coefficient of restitution that accounts for the changes of the particle's momentum following particle-wall impact is kept as a constant and not based on a

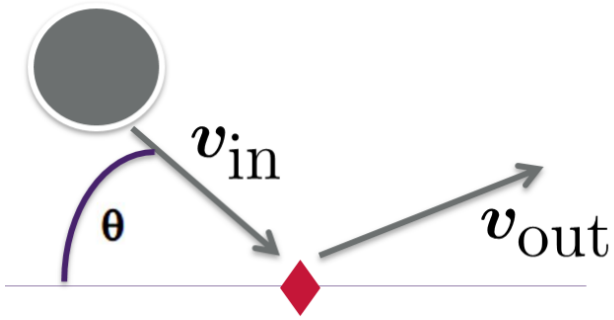

Figure 4.2: Rebound of particle approaching at an angle of θ with velocity $\boldsymbol{v}_{in}$.

stochastic rebound model based on the particle impact angle given by Grant and Tabakoff [1975]. This is due to the negligible loss of momentum of the particle from particle-wall collisions along with the dominating drag term describing the momentum exchange between the particle and the fluid [Zhang et al., 2007].

4.2.3 Scaling Factors

When simulating wear using representative Lagrangian particles, two scaling factors needs to be considered. The first is the appropriate scaling of particles as only a representative number are simulated within the domain, therefore particle numbers needs to be artificially scaled using by a modifier to account for the actual number of particles within the system. The second scaling factor is an acceleration factor used to increase the rate of wear and thus decreasing the time taken to study the effect of wear numerically when compared to physical scenario. This acceleration factor is required as wear is a comparatively slow process

The modifier to account for particle scaling is calculated by finding the rate of actual number of particles flowing through the system through the following relationship

$$Q_p = Q_f \phi_p, \tag{4.6}$$

where Q_p is the particle flow rate, Q_f the fluid flow rate and ϕ_p the particle volume fraction. The number of actual particles flowing through the system can therefore

be denoted by

$$N_p = \frac{Q_p}{V}, \tag{4.7}$$

where N_p is the number of actual particles and V the volume of a single particle. The particle volume fraction ϕ_p can be found using the relationship of particle concentration by weight within the system

$$\phi_p \rho_p + (1 - \phi_p)\rho_f = \rho_m = \frac{1}{\frac{C_w}{\rho_p} + \frac{1-C_w}{\rho_f}}, \tag{4.8}$$

where ρ_m is the density of the slurry mixture and C_w the concentration of the particles by weight in the slurry. The modifier defining particle scaling is then obtained through

$$Modifier = \frac{N_p}{Insertion\ rate}. \tag{4.9}$$

A high modifier is obtained where there are lower insertion rates of simulated particles compared to actual number of particles in the system, therefore each representative particle in the simulation accounts for a greater number of real particles in the actual system. Simulations with a high modifier will be computationally less expensive but at a cost to sensitivities to individual particle's contribution to wear.

The acceleration factor used to increase the rate of wear must be derived from the time scale with which the surface erodes in real time versus the time scale at which the boundary is set to erode in the numerical simulation. The acceleration factor can be expressed as

$$Acceleration = \frac{Simulation\ time\ scale}{Actual\ time\ scale}. \tag{4.10}$$

The acceleration factor needs to be carefully adjusted so a balance is reached in obtaining simulation wear profiles over a feasible time frame yet not too large where the wear affects the overall multiphase flow. This sensitivity of the acceleration factor is analysed and discussed in Section 6.2.2.

4.2.4 Model assumptions

Throughout the application of the wear model used within this thesis, the following assumptions have been made to the model equations. Whilst the wear model have

the capability of adopting different values of the assumptions given below, the selected values are generally accepted within the industry and literature and the study of the effect of these parameters remains out of scope of this thesis.

- Fluid is incompressible.
- Gravity is assumed to be near the Earth's surface, $\boldsymbol{g} = 9.8\text{ms}^{-2}$.
- In the Kinetic Theory of Granular Flow, the radial distribution function controlled by the maximum packing fraction takes the value $\alpha_{max} = 0.6$ [Ding and Gidaspow, 1990].
- The solid stress tensor for KTGF is simplifed to only include the solid pressure term defined in Equation 2.25.
- Particles are defined as point particles.
- Particles are assumed to be spherical within the wear equation, thus the particle sharpness factor can be taken as $F_s = 0.5$ [Arabnejad et al., 2015b].
- Particle wall collisions are near elastic, $e = 0.99$.

4.3 Solution Method

Within Fluidity, the solution method considers the momentum equation that has been discretised in space using the Galerkin finite element method and in time using the implicit backward Euler scheme with $\theta = 1$ (see Section 3.3) such that the momentum equation becomes

$$\begin{aligned}\boldsymbol{M}(\alpha_f^{n+1})\frac{\boldsymbol{u}_f^{n+1}-\boldsymbol{u}_f^n}{\Delta t} + \boldsymbol{A}(\alpha_f^{n+1},\boldsymbol{u}_f^{n+1})\boldsymbol{u}^{n+1} - \boldsymbol{K}(\alpha_f^{n+1})\boldsymbol{u}_f^{n+1} \\ -\boldsymbol{C}(\alpha_f^{n+1})p^{n+1} = \boldsymbol{b}(\alpha_f^{n+1}) + \boldsymbol{F}(\alpha_f^{n+1},\boldsymbol{u}_f^{n+1},\boldsymbol{u}_p^{n+1}),\end{aligned} \tag{4.11}$$

where matrices $\boldsymbol{M}$, $\boldsymbol{A}$, $\boldsymbol{K}$, $\boldsymbol{C}$ and $\boldsymbol{F}$ are the mass, advection, stress, gradient and drag force matrices and vector $\boldsymbol{b}$ represents the gravitational force. Their components are defined as

$$\boldsymbol{M}_{ij} = \int_\Omega \phi_i \alpha_f^{n+1} \rho \phi_j, \tag{4.12}$$

$$\boldsymbol{A}_{ij} = \int_{\Omega} \boldsymbol{\nabla}\phi_i \cdot \alpha_f^{n+1} \rho_f \boldsymbol{u}_f^{n+1} \phi_j, \tag{4.13}$$

$$\boldsymbol{K}_{ij} = \int_{\Omega} \boldsymbol{\nabla}\phi_i \cdot \alpha_f^{n+1} \mu \boldsymbol{\nabla}\phi_j, \tag{4.14}$$

$$\boldsymbol{C}_{ij} = \int_{\Omega} \phi_i \alpha_f^{n+1} \boldsymbol{\nabla}\psi_j, \tag{4.15}$$

$$\boldsymbol{F}_{ij} = \int_{\Omega} \phi_i \beta \phi_j, \tag{4.16}$$

$$\boldsymbol{b} = \int_{\Omega} \phi_i \alpha_f^{n+1} \rho_f \boldsymbol{g}. \tag{4.17}$$

Particle motion equations are discretised using an operator splitting method, where the drag term is solved semi-implicitly and all other terms calculated explicitly using an arbitrary second order Adams-Bashforth scheme [MacNamara and Strang, 2016] An exception is the first timestep following a particle insertion or following a particle-wall collision when the explicit forward Euler scheme. For particle position, Equation 2.13 becomes

$$\boldsymbol{x}_p^{n+1} = \boldsymbol{x}_p + \frac{(t_{n+1} - t_n)}{2(t_n - t_{n-1})}(\boldsymbol{u}_p^n(t_{n+1} + t_n - 2t_{n-1}) - \boldsymbol{u}_p^{n-1}(t_{n+1} - t_n)), \tag{4.18}$$

and when using the forward Euler scheme, particle position is defined as

$$\boldsymbol{x}_p^{n+1} = \boldsymbol{x}_p^n + (t_{n+1} - t_n)\boldsymbol{u}_p^n. \tag{4.19}$$

The force balance equation (Equation 2.11) becomes

$$\begin{aligned} \left(1 + \frac{\rho_f}{2\rho_p} + \beta^* \Delta t\right) \boldsymbol{u}_{\boldsymbol{p}}^{n+1} &= \boldsymbol{u}_p^n + \frac{\rho_f}{2\rho_p}(\boldsymbol{u}_f^{n+1} - \boldsymbol{u}_f^n) \\ + \frac{(t_{n+1} - t_n)}{2(t_n - t_{n-1})}(\boldsymbol{f}^n(t_{n+1} + t_n - 2t_{n-1}) &- \boldsymbol{f}^{n-1}(t_{n+1} - t_n) + 2\beta^* \boldsymbol{u}_f^{n+1}), \end{aligned} \tag{4.20}$$

where $\beta^* = \beta(\boldsymbol{u}_f, \boldsymbol{u}_p)$ is the drag coefficient at the last timestep for which velocity data is available and

$$\boldsymbol{f}^n = -\boldsymbol{\nabla} p^n - \boldsymbol{g} \tag{4.21}$$

are the remaining body forces. This splitting of the drag term is chosen so that the drag from the fluid cannot artificially accelerate the particle above its own velocity whilst preserving the drag term at the same time level. This is an important factor as the particle impact velocity is crucial in predicting the wear rate.

To allow for the ability to fully couple the fluid and particle phases, velocities and pressures need to be calculated simultaneously between the phases. There is explicit coupling between the two phases based on the previous timesteps. Fluid velocity, pressure and domain boundary locations are used by the particle module for the Lagrangian particle tracking. Body forces consisting of gravity, solid pressure (Section 2.4.2) and drag forces (Section 2.4.1) are calculated along with collision events described in Section 4.2.2. Mesh movement on the boundary is calculated based on the wear velocity and the new boundary location along with the fluid velocity and pressure is then used for the next solid phase timestep. Mesh adaptivity is performed at specified timesteps on fluid phase fields enabled with the adaptivity option. The general process for the modelling framework is illustrated in Figure 4.3 and descriptions of the main elements provided in the steps below.

- Simulation initiated within Fluidity.
- Fluidity initialises fluid phase.
- Fluidity solves for fluid phase.
- Fluidity initialises the Particle Model through the use of a scalar python diagnostic algorithm by allowing direct access to the internal Fluidity data structures in the computation of a diagnostic field [Imperial College London, 2014].
- The particle module is initialised with fluid velocity, fluid pressure, timestep information and surface boundary information. Particle parameters are also obtained from the Fluidity options files, these include particle diameter, density, particle velocity at inlet, insertion rate, inlet and outlet surface IDs. For subsequent timesteps, no initialisation occurs and Fluidity passes through fluid velocity, pressure, timestep, time and boundary information. Particle information will already be available within the particle bucket after the first timestep.
- A particle bucket is created with the initial particle positions and velocities. For subsequent timesteps, the particle bucket contains the particles from the previous timestep.

- For each particle within the particle bucket, the state of the particle is updated to the next timestep using an arbitrary second order Adams-Bashforth scheme. During this update step, the model calculates the particle volume fraction, drag force (Equations 2.15, 2.16), solid pressure (Equation 2.25) and checks for collision against the deforming wall (see Section 4.2.2). After the first timestep, particles are also inserted from the inlet at the specified insertion rate. Checks are performed to remove any particles that is now outside the system boundary as a result of boundary deformation or exiting the defined outlet, these particles are then recycled to be reinserted at the inlet to reduce any additional computation cost.

- Particle volume fraction, wear rate and drag force is then passed back into fluidity and stored in relevant scalar and vector fields using the scalar python diagnostic algorithm field.

- The particle module ends its time loop by writing the output to a VTP file and advancing a timestep.

- Fluidity calculates the wear velocity based on the wear rate smoothed out using a damped diffusive equation described in Section 4.2.1.

- Fluidity checks if mesh adaptivity should occur on the wear velocity based on the parameters set within the options file.

- Fluidity writes the output to a VTU file and advances a timestep ending the time loop for the fluid phase.

4.4 Model Verification

In order to verify the accuracy and correctness of the wear modelling framework, a convergence analysis was conducted on a small scale numerical simulation on a simple static geometry. Convergence analysis checks that the errors in the numerical

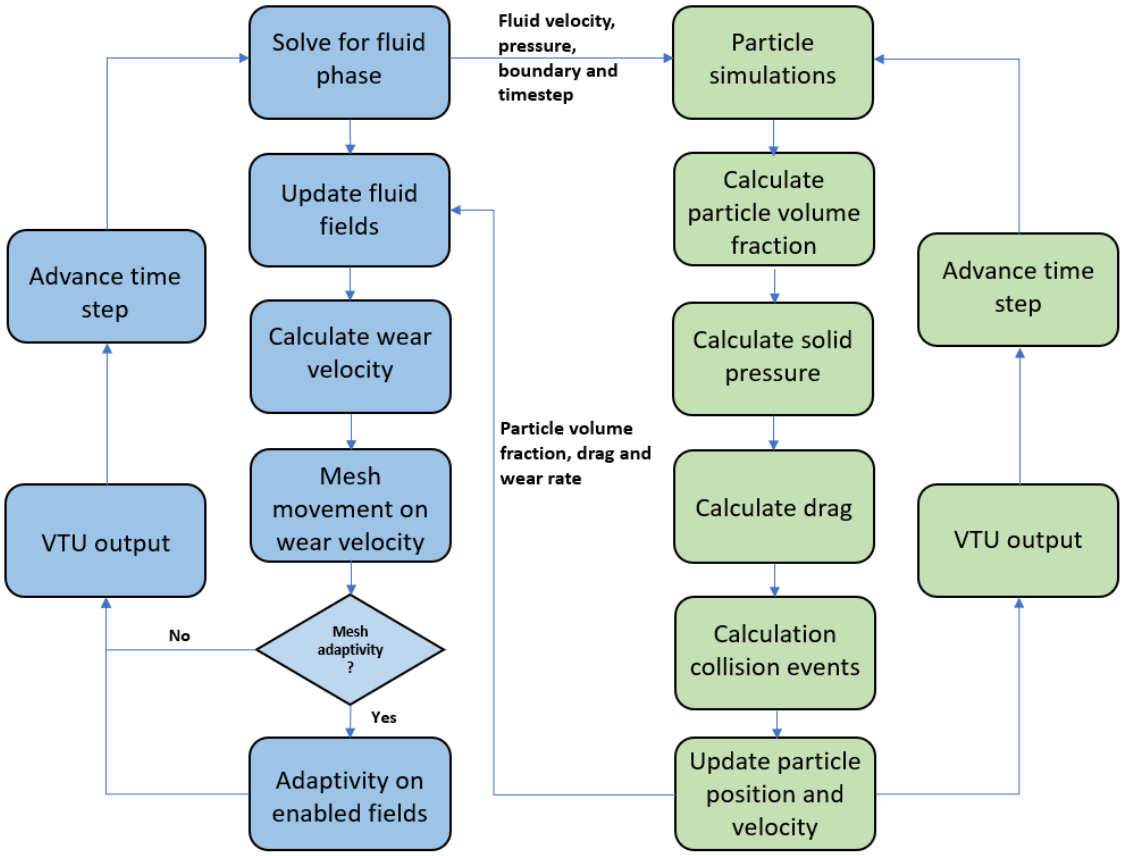

Figure 4.3: Process diagram describing the implementation of the fully coupled wear modelling framework. Boxes in blue denotes simulations conducted in Fluidity, boxes in green are calculations performed in the particle module.

solution decreases at the expected as the mesh resolution increases or as the time step sizes decreases [Ferziger, 2002].

The test case was created to verify the order of convergence of the spatial discretisation when using the $P1_{DG}$-P2 element pair in the fluid phase as well as the convergence of the discretisation performed on the particle phase. Time discretisation in the fluid phase was performed using a second order θ scheme with $\theta = 0.5$ also known as the Crank-Nicolson method. Particles were discretised using an arbitrary second order Adams-Bashforth scheme with a first order forward Euler scheme at first insertion or after a particle-wall collision event.

The domain, initial conditions, boundary conditions and physical parameters used in this case is similar to that of the jet impingement validation case in Section 4.5.2. However, the verification tests were performed on fixed structured meshes across the whole domain with fixed decreasing time step sizes and no mesh movement methods in order to accurately measure the correctness of the errors in the numerical solution.

The dimensions of the domain were $0 \leq x \leq 1$ and $0 \leq y \leq 1$ with initial fluid velocity and boundary condition along $x = 0$ as

$$\boldsymbol{u}_f = \left[2\pi \cos\left(\frac{\pi}{2}x\right) sin(\pi y), -\pi \cos\left(\frac{\pi}{2}x\right) sin(\pi y)\right]^{\boldsymbol{T}}. \tag{4.22}$$

No normal flow was imposed along $x = 1$ with no slip boundary conditions and zero pressure along $y = 0$ and $y = 1$. Boundary condition for fluid velocity along $x = 0$ was the same as that of the initial condition across the whole field. Particles were inserted between $[0, \frac{1}{3}]$ and $[0, \frac{2}{3}]$ at a rate of $1x10^5$ particles per second with velocity matching that of the fluid. Physical parameters for the fluid and particles were chosen arbitrarily with erosion factors based on experimental values obtained for Carbon Steel 1018 from Arabnejad et al. [2015b], these are summarised in Table 4.1.

For the mesh convergence study, 5 fixed structured meshes composed of triangular elements were produced with Gmsh [Geuzaine and Remacle, 2009] using element lengths of $l = 0.1, 0.05, 0.025, 0.0125$ and 0.001 with decreasing time step size of $t = 0.05, 0.025, 0.01250.00625$ and 0.005 to maintain a constant Courant num-

Parameter	**Name**	**Value**
D	Particle diameter	0.0004 m
ρ_p	Particle density	2500 kgm^{-3}
ρ_f	Fluid density	1000 kgm^{-3}
μ_f	Fluid viscosity	0.001 Pas
C	Cutting erosion factor	0.01
H	Vickers hardness coefficient	131 GPa
F_S	Particle sharpness factor	0.5
K	Ratio of contact	0.4
ϵ	Deformation erosion factor	$4.2\text{x}10^{11}$
U_0	Threshold velocity	0.5ms^{-1}

Table 4.1: Physical parameters of particle and fluid properties used within the jet impingement verification and validation case.

ber of 0.5. Time convergence was studied at fixed decreasing time step sizes of $\Delta t = 0.1, 0.05, 0.025, 0.0125$ and 0.001 over a fixed structured mesh with element length $l = 0.025$m. Simulations for all convergence studies ran for a total time of $t = 1$s. Error in L^2 norms were calculated against the finest resolution mesh of $l = 0.001$m for mesh convergence and smallest time step size of $t = 0.001$s for time convergence.

Plots of the error in the velocity fields in Figures 4.4(a) and 4.4(b) shows the successful convergence at second order as expected when using the $P1_{DG}$-P2 element pair [Cotter and Ham, 2011]. The pressure field shows the same second order convergence. Convergence of the particle volume fraction calculated within the particle module coupled to Fluidity shows a convergence rate between first and second order as seen in Figures 4.4(c) and 4.4(d). Figures 4.5(a) and 4.5(b) shows the successful time convergence at second order for fluid velocity and pressure fields using the Crank-Nicholson method ($\theta = 0.5$) and Figures 4.5(c) and 4.5(d) shows the convergence of the particle volume fraction to be between first and second order. The derivation from the second order convergence can be explained by the use of the first order explicit forward Euler scheme following a particle insertion or following a particle-wall collision.

4.5 Model Validation

Small scale numerical simulations were performed to validate the components of the wear model. This was to ensure that the model equations being solved accurately predicted the behaviour of the physical systems it was modelling. Two validation simulations were conducted within this thesis, each validating a different aspect of the overall particle wear model. First, the behaviour of particles settling in a fluid was numerically simulated. This validation case confirmed the accuracy of the particle-fluid coupling and time integration scheme. The second case considered an impingement jet simulation in 2 dimensions. The impingement jet simulation confirmed the wear model selected and showed the importance of coupling wear with boundary movement when considering surface wear profiles.

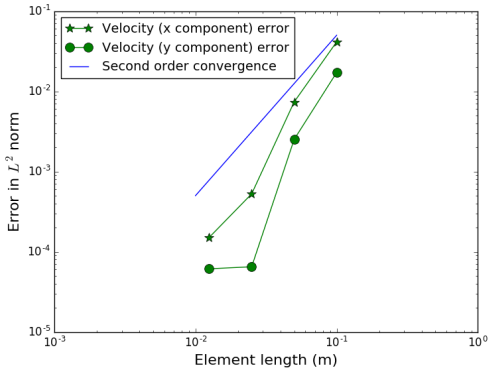

(a) Error in velocity field

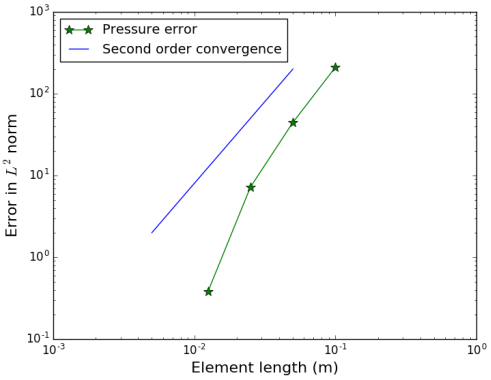

(b) Error in pressure field

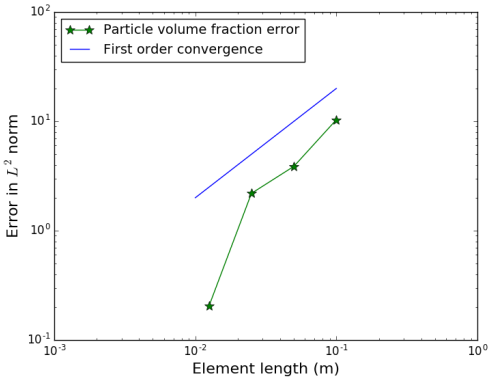

(c) Error in particle volume fraction at 1st order

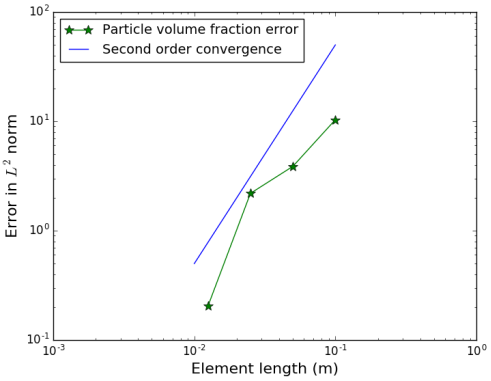

(d) Error in particle volume fraction at 2nd order

Figure 4.4: Mesh convergence plots for the jet impingement verification case. The velocity and pressure fields converged at second order as expected with $P1_{DG}$-P2 element pair. Particle volume fraction solved within the Python particle module and coupled in Fluidity converged between first and second order.

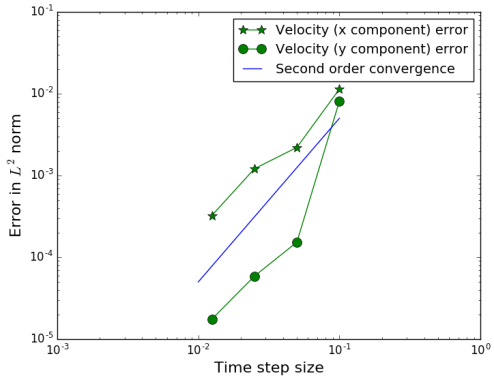

(a) Error in velocity field

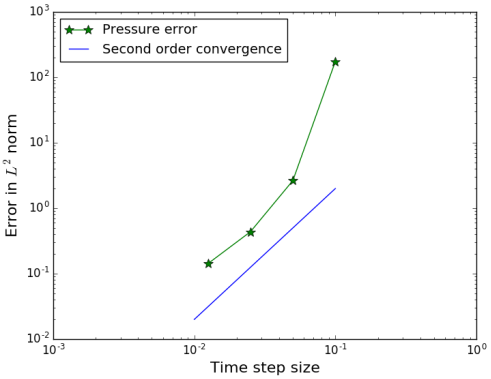

(b) Error in pressure field

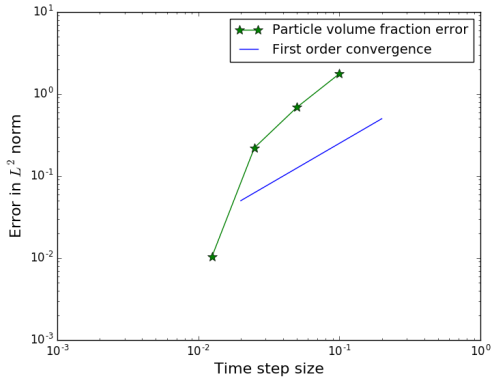

(c) Error in particle volume fraction at 1st order

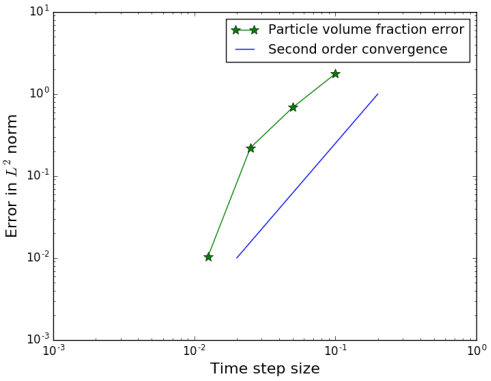

(d) Error in particle volume fraction at 2nd order

Figure 4.5: Time convergence plots for the jet impingement verification case. The velocity and pressure fields solved within Fluidity converged at second order as expected. Particle volume fraction solved within the Python particle module and coupled in Fluidity converged between first and second order.

4.5.1 Particle settling in fluid

Numerical simulation of gravity driven settling in a steady fluid provided the ability to validate the accuracy of the particle fluid coupling where an analytical solution exists through the application of Stokes' law. For spherical particles, this occurred when the particle Reynolds number < 1 [Crowe, 2005]. The simulation consisted of a spherical particle falling under the influence of gravity in a stationary fluid so the terminal velocity can be calculated.

While this test case focuses on low particle Reynolds number in order to verify the validity of particle-fluid coupling and time integration through an analytical solution, the particle model within this thesis is able to accommodate a range of particle Reynolds number and will choose an appropriate scheme as described in Equations 2.16 and 2.17.

The Stokes drag force was given by

$$\boldsymbol{F_d} = 6\pi\mu R\boldsymbol{v}, \tag{4.23}$$

where F_d is the drag force coupling the fluid and the particle, viscosity μ, particle radius r and $\boldsymbol{v}$ the relative velocity between the particle and the fluid [Stokes, 1851]. Net force acting on the particle is

$$\boldsymbol{F}_{net} = \boldsymbol{F}_g - \boldsymbol{F}_d, \tag{4.24}$$

which can be written as

$$m\frac{\mathrm{d}\boldsymbol{v}}{\mathrm{d}t} = m\boldsymbol{g} - 6\pi\mu R\boldsymbol{v}. \tag{4.25}$$

Substituting $m = (\rho_p - \rho_f)\frac{4}{3}\pi R^3$ and integrating with conditions $\boldsymbol{v} = 0$ at $t = 0$ gives the velocity profile of the falling particle under gravity as

$$\boldsymbol{v} = \frac{2}{9}\frac{(\rho_p - \rho_f)}{\mu}R^2\boldsymbol{g}\left(1 - \exp\left(-\frac{9\mu t}{2R^2(\rho_p - \rho_f)}\right)\right). \tag{4.26}$$

Terminal velocity of the particle was calculated when the gravitational force equals that of the drag force $\boldsymbol{F_g} = \boldsymbol{F_d}$, solving for velocity $\boldsymbol{v}$ gives a terminal velocity of

$$\boldsymbol{v} = \frac{2}{9}\frac{(\rho_p - \rho_f)}{\mu}\boldsymbol{g}R^2, \tag{4.27}$$

with the gravitational force defined by [Richardson, 2002]

$$\boldsymbol{F_g} = \frac{4}{3}\pi R^3(\rho_p - \rho_f)\boldsymbol{g}. \tag{4.28}$$

The numerical simulation took place in a fixed, structured, two dimensional square domain defined by $0.0 \leq x \leq 1.0$ and $0.0 \leq y \leq 1.0$ with the initial particle position at the centre of the domain. A zero velocity and pressure field was imposed at $t = 0s$ for both the particle and the fluid. Fixed time step size of $dt = 0.005s$ with an overall time of $t = 0.25s$. The physical parameters used are defined by Table 4.2.

Parameter	**Value**
R	200 x $10^{-6}m$
ρ_p	2500 kgm^{-3}
ρ_f	1000 kgm^{-3}
μ	0.001 Pas
$\boldsymbol{g}$	$[0,-9.8]^T ms^{-1}$

Table 4.2: Physical parameters of particle and fluid properties used within the particle settling in fluid under gravity validation case.

Numerical simulation results showed that the particle reached terminal velocity of $\boldsymbol{v} = [0, -0.1307]^T ms^{-1}$ at $t = 0.14s$. This corresponds well with the analytical solution. The velocity profile of the particle settling over time is presented in Figure 4.6. The maximum error between the analytical and numerical solution occurred at $t = 0.015s$ with an absolute error of $|error| = 0.00784ms^{-1}$.

Investigation of the numerical solution with varying particle sizes also showed good correlation with the analytical solution. It can be observed in Figure 4.7 that larger particle sizes had higher terminal velocities, time to reach terminal velocity converged at second order as seen in Figure 4.8. Finally, the error in the L^2 norm for the particle velocity can be observed to converge between first and second order

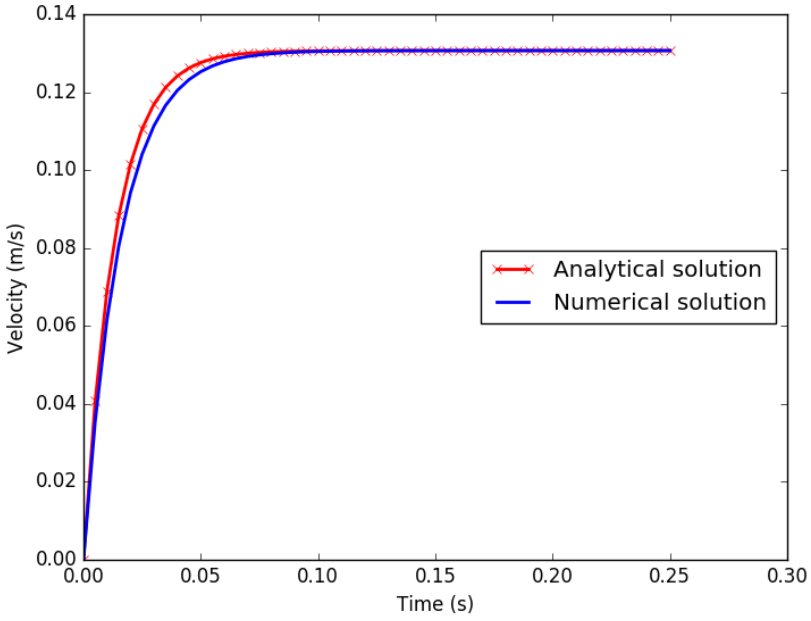

Figure 4.6: Velocity profile of a particle settling under gravity within the Stokes' regime for particle radius of R = 0.0002m.

when compared with the analytical result as shown in Figure 4.9. The derivation from second order can be explained by the explicit coupling at the previous time step.

4.5.2 Jet impingement

The numerical simulation of the 2 dimensional jet impingement is a test case that combines all the components of the wear model which then couples to boundary deformation. This test case brings together all the components of the wear modelling framework to show the expected behaviour is plausible using a simple, but industrially relevant geometry. The test will highlight the importance of surface deformation when considering wear in response to particle impingement through the coupling of the wear rate to moving geometries by considering the full coupling of particle-fluid interactions, a wear model and moving geometries in the form of mesh movement in response to wear velocity.

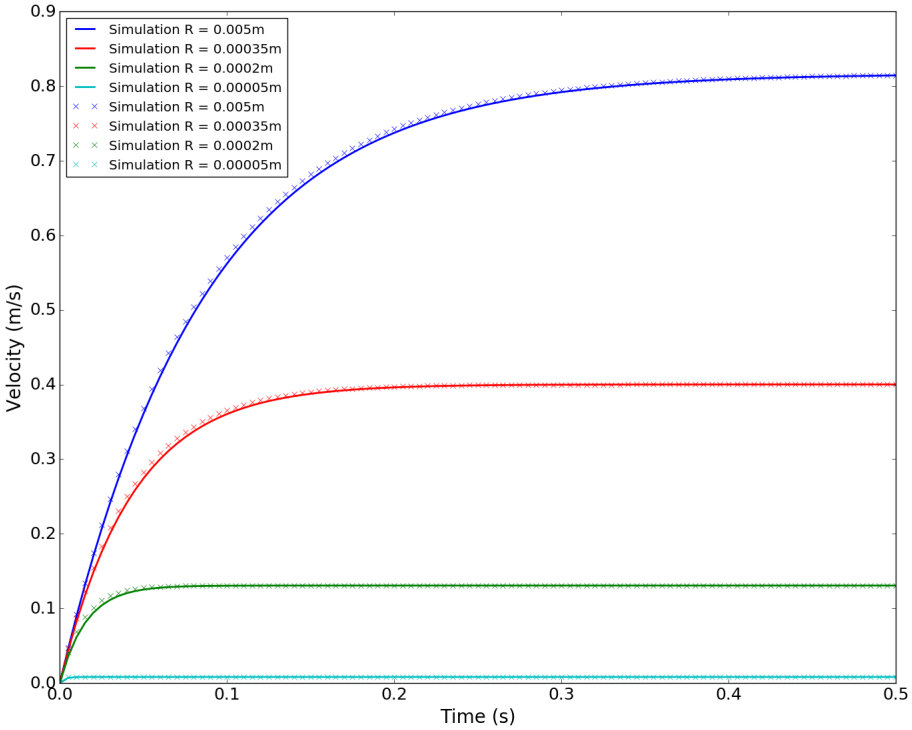

Figure 4.7: Velocity profile of varying particle sizes settling under gravity within the Stokes' regime.

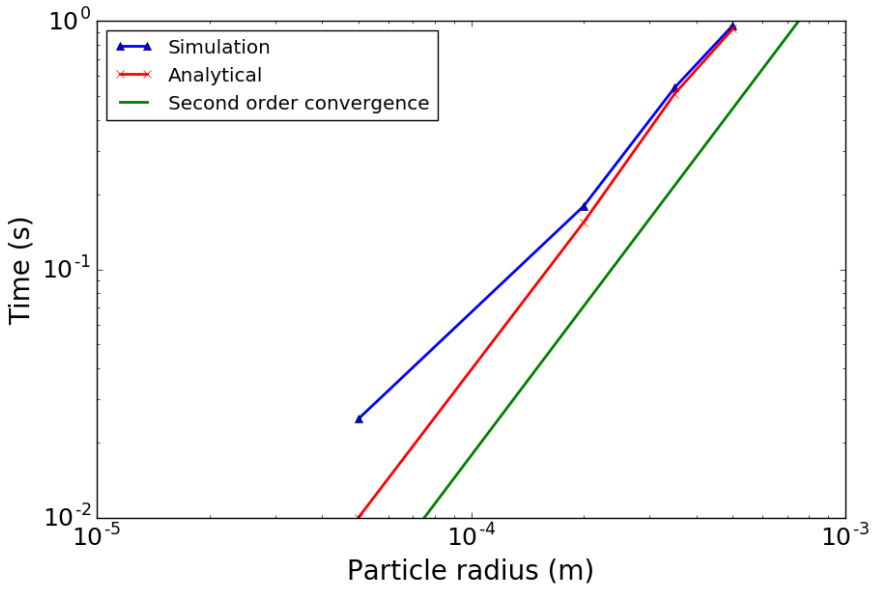

Figure 4.8: Time to reach terminal velocity with as particle sizes vary converges at second order for varying particle sizes settling under gravity within the Stoke's regime.

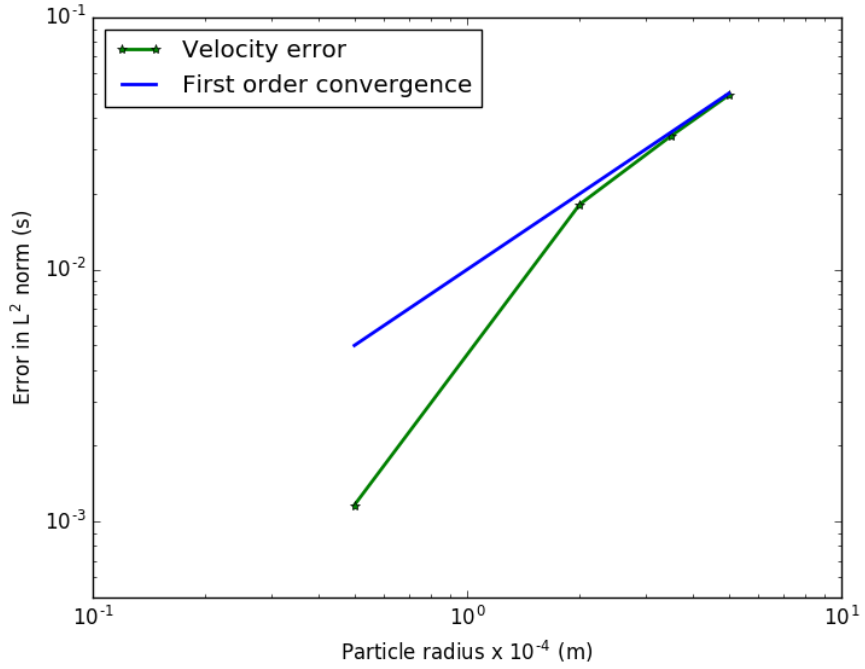

(a) First order convergence

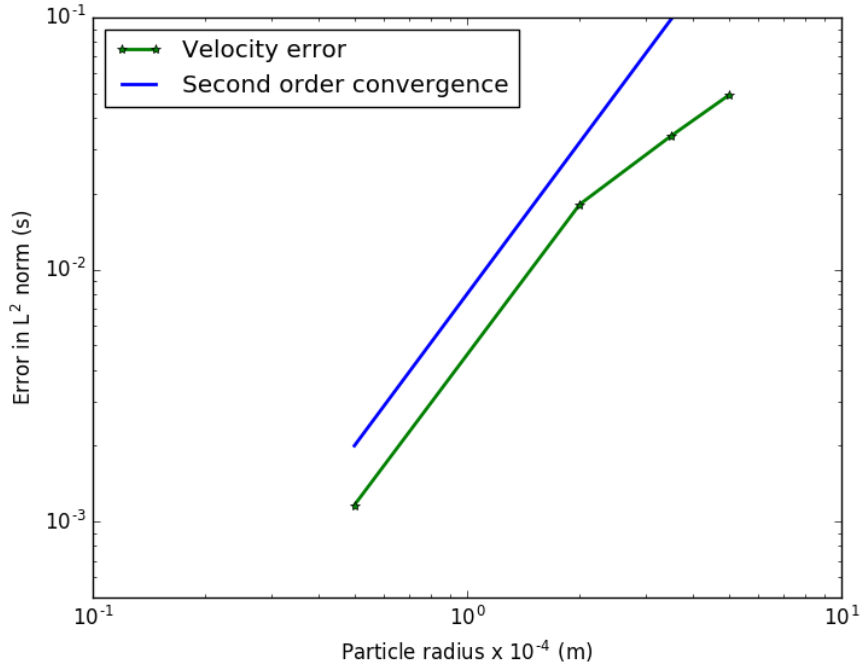

(b) Second order convergence

Figure 4.9: Error in L^2 norm of particle velocity at varying particle size converges between first and second order for gravity driven settling under the Stokes' regime.

The jet impingement case is a simplification of the abrasive slurry jet micro-machining (ASJM) process that uses a pressurised abrasive slurry to erode features with a high resolution on a variety of materials [Nouraei et al., 2014, Ghobeity et al., 2008, Matsumura et al., 2011, Nguyen et al., 2014]. An example of the ASJM apparatus with corresponding sample profiles created using ASJM is provided in Figure 4.10

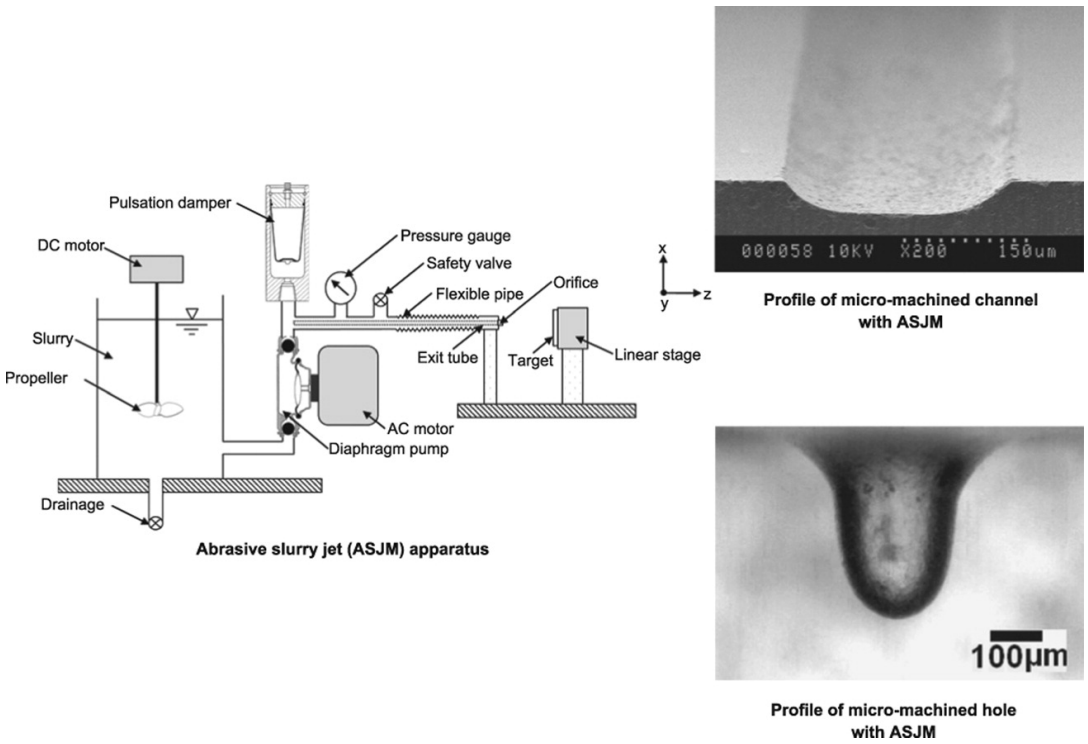

Figure 4.10: Abrasive slurry jet micro-machining apparatus with sample profiles of channels created by the abrasive jet. Figure obtained from Nouraei et al. [2014].

This test case takes a simplified version of the ASJM by considering a 2 dimensional model of the slurry jet in order to validate the expected behaviour of boundary deformation in response to wear.

Domain, Initial Conditions and Boundary Conditions

The numerical simulation takes place in the same domain as the jet impingement case defined in Section 4.5. The initial conditions and boundary conditions also matches that of the validation case with no-normal flow boundary conditions, $\boldsymbol{u}_f \cdot \boldsymbol{n} = 0$

exists along the deforming boundary along $x = 1$, with no slip boundary conditions along $y = 0$ and $y = 1$. Fluid velocity, $\boldsymbol{u}_f$, along the inlet ($x = 0$) was set to equal the initial condition defined in Equation 4.22, pressure was configured to be zero along $y = 0$ and $y = 1$. Figure 4.11 depicts the initial conditions of the fluid phase for the pressure and velocity fields.

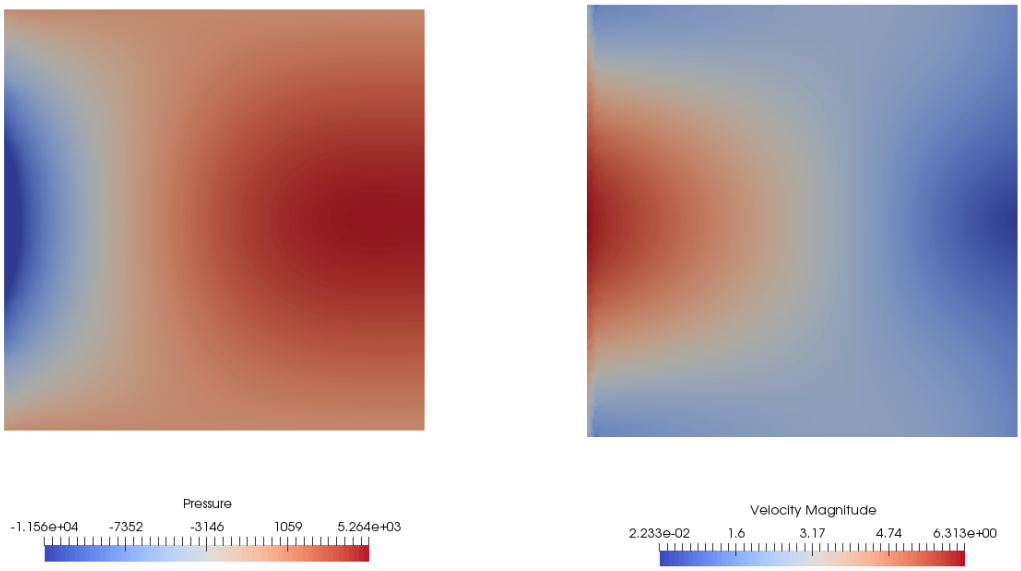

Figure 4.11: Initial conditions of the fluid phase for jet impingement study. Pressure field is illustrated on the left and the velocity field shown on the right.

Particles were inserted at the inlet ($x = 0$) at a rate of 1x10^5 particles per second, the particle velocity at the inlet was defined as

$$\boldsymbol{u}_p = \left[2\pi \cos\left(\frac{\pi}{2}x\right) sin(\pi y), -\pi \cos\left(\frac{\pi}{2}x\right) sin(\pi y)\right]^{\boldsymbol{T}}. \tag{4.29}$$

matching that of the fluid velocity at the inlet. To give the shape of the impingement jet, particles were only inserted along the inlet between $\frac{1}{3} \leq y \leq \frac{2}{3}$, this can be observed in Figure 4.12. Particles were configured to impact and rebound from the surface along $x = 1$ with the remaining boundaries ($x = 0$, $y = 0$ and $y = 1$) set as a possible outlet for particles to exit the domain. Interaction terms between the particle and the fluid exist through the use of the a transitional drag model as defined in Section 2.4.1 with particle particle interactions modelled using a solid pressure

taken from KTGF defined in Section 2.4.2. The pseudo-diffusivity parameter to smooth out wear was set to 0.001 with the wear rate artificially accelerated by a factor of 1000.

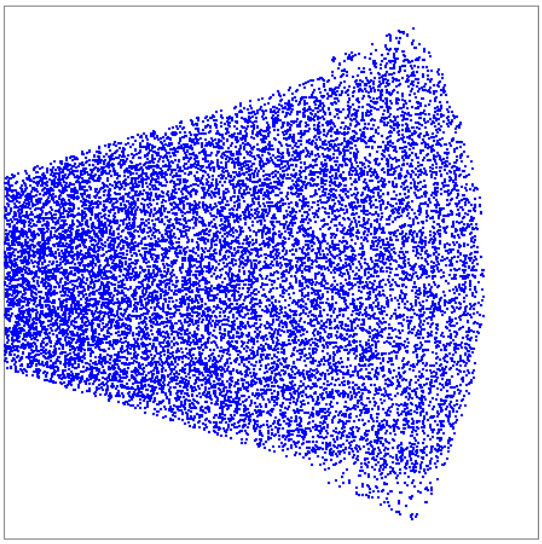

Figure 4.12: Particle profile for the impingement jet.

Physical Parameters

Physical parameters of the particle, fluid and surface material are defined in Table 4.1. Carbon Steel 1018 was selected as the reference surface material as it is widely used many industries. Its material properties and the empirical values used within the wear model were taken from Arabnejad et al. [2015b].

Spatial and Temporal Discretisation

For the fluid phase, the continuity and momentum equations were discretised in space using the Galerkin finite element method with the $P1_{DG}$-P2 element pair. The 2nd order Crank-Nicholson method ($\theta = 0.5$) was used to step the discretised equations forward in time with time step size of $t = 0.001s$.

As described in Section 4.3 the equations of motion for the particles follows the solution method for the Lagrangian particle modelling and discretised using an

operator splitting method and a second order Adams-Bashforth scheme was used to step the equations forward in time, unless at the first time step after particle insertion or after particle wall collision when a forward Euler scheme was used.

Mesh generation and movement

Gmsh [Geuzaine and Remacle, 2009] was used to generate the initial mesh of the domain composed of triangular elements with varying a characteristic element length. The characteristic element length, l, along the $x = 0$ boundary was set to be $l = 0.025$m, whereas a finer resolution was defined along the $x = 1$ boundary with $l = 0.001$m. The initial mesh of the domain can be observed in Figure 4.13. Mesh movement methods using the wear velocity as the chosen grid velocity were enabled to allow for the movement of the boundary in response to wear. No mesh adaptivity was enabled for this numerical simulation as the simulation took place over a simple 2D domain where the initial mesh provided sufficient resolution to conduct a short running validation case where the additional time taken in performing mesh adaptivity would out weigh the benefits in reducing computational cost.

A comparison numerical simulation with a static boundary was conducted using the same initial mesh without mesh movement and the results discussed in Section 4.5.2.

Results

The wear modelling framework with boundary movement in response to wear was able to confirm the importance of considering boundary deformation in response to wear over time and not just the initial wear. Figures 4.14 shows the simulated boundary deformation over time in response to wear and 4.15 shows the normalised surface wear profile over time. Initial wear when the particles first experienced particle-wall collisions occurred at $t = 0.2s$ highlights the static boundary with no deformation. As time progressed, maximum wear was observed to be off centre from the jet axis at $y = 0.5$m on the domain, most evident at $t = 0.28s$. This could be due non-uniform particle insertion as the particles were inserted into the domain at

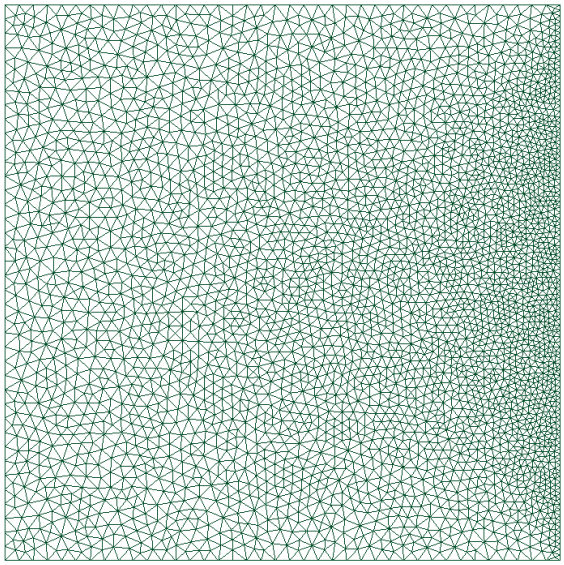

Figure 4.13: Initial mesh for jet impingement simulation.

random points following a specified velocity profile and insertion rate as defined by Equation 4.29. Along with Figure 4.16, wear velocity reduces as time progressed and becomes more evenly distributed along the deforming boundary. The shape of the wear profile also became less distinct, especially around a distance of 0.2m above the jet axis where the gradient of the wear profile starts to decrease as time progressed. This suggests that after the initial wear and boundary deformation, particles behaviour and trajectory changes and begins to smooth out the deforming boundary. However, the maximum wear over time remained unsymmetrical concentrated to the top of the jet axis.

Results of the deforming boundary were compared to that of a static boundary numerically simulated under the same simulation set configuration without mesh movement enabled. Figure 4.17 illustrates the difference between wear velocities when simulated under static and deforming boundaries. At first particle-wall collision ($t = 0.2s$) (Figure 4.17), both wear velocities between static and deforming simulations achieved the same wear velocity profile and magnitude as expected. At $t = 0.24s$, the wear velocities were still comparable in profile and magnitude between the two scenarios as the boundary begins to deform. As the boundary deformation continues, the wear velocity decreases and slowly becomes even as time

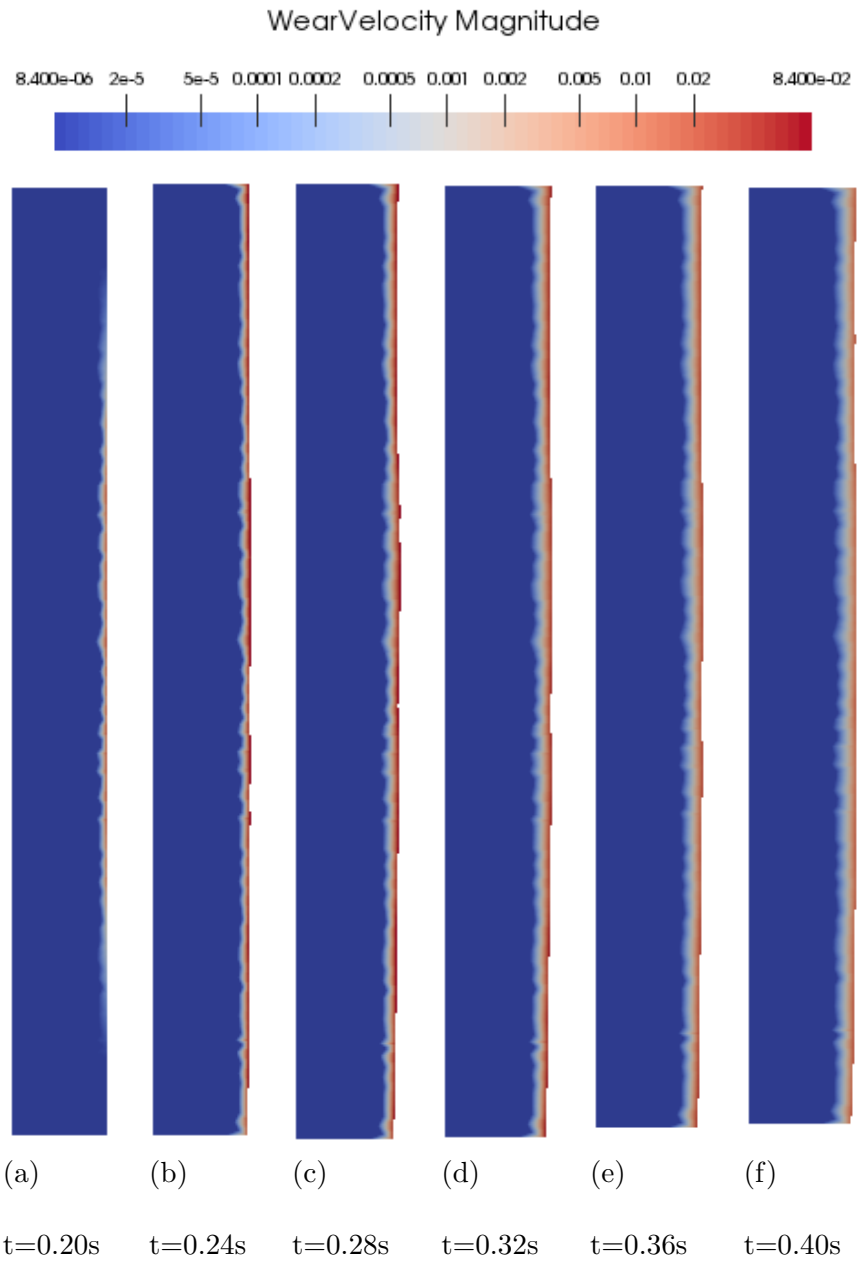

Figure 4.14: Images of wear velocity field with boundary deformation in the jet impingement validation case taken at specified time periods corresponding to the normalised surface wear profile in Figure 4.15. A section of the full domain was taken at x = 0.9m.

reaches $t = 0.4s$, this is due to the particles impacting across the entire length of the boundary by t=0.28s and smoothed out over time. The increase in distance of the deforming boundary from the initial jet due to wear also contributed to the decrease in particle velocity. However, static boundary wear velocities remains at a similar magnitude and profile as time progressed, this is as expected as there are no changes within the domain. This result highlights the significance of considering boundary movement within a wear modelling framework.

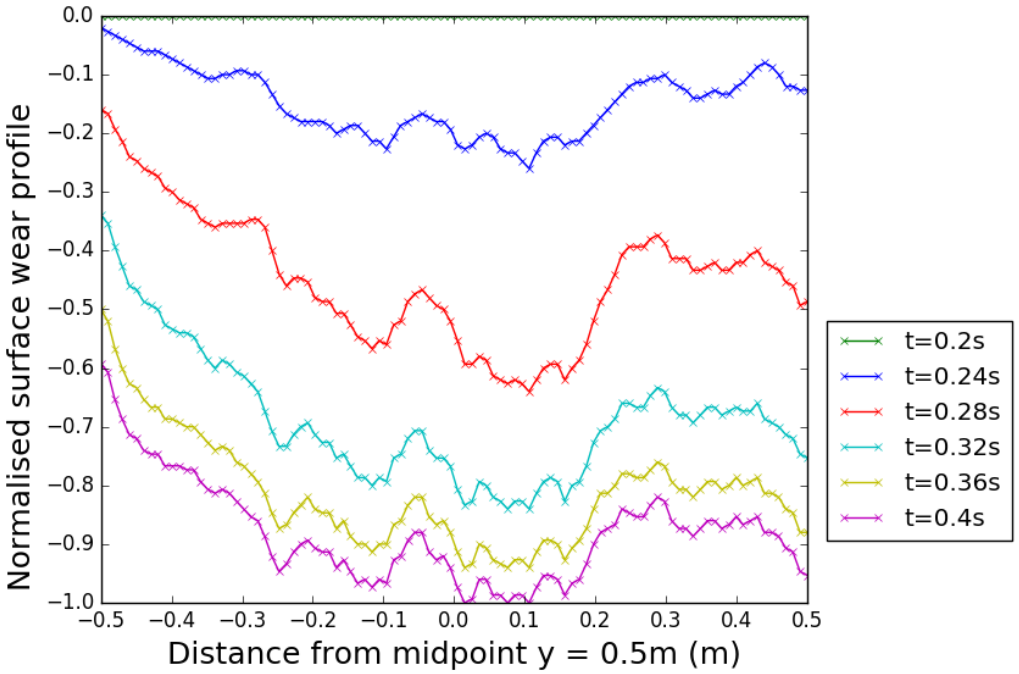

Figure 4.15: Normalised surface wear profile for jet impingement experiment at varying times with mesh movement enabled. Increase wear was observed off centre from the mid point increasing further with maximum wear to one side of the jet axis. Normalisation of surface wear profile is based on min-max normalisation across all time points.

The results shown for the 2 dimensional jet impingement case agrees with Nguyen et al. [2014]'s work in confirming wear and subsequent wear events is sensitive to changes to the surface profile of the target material, thus highlighting the need to

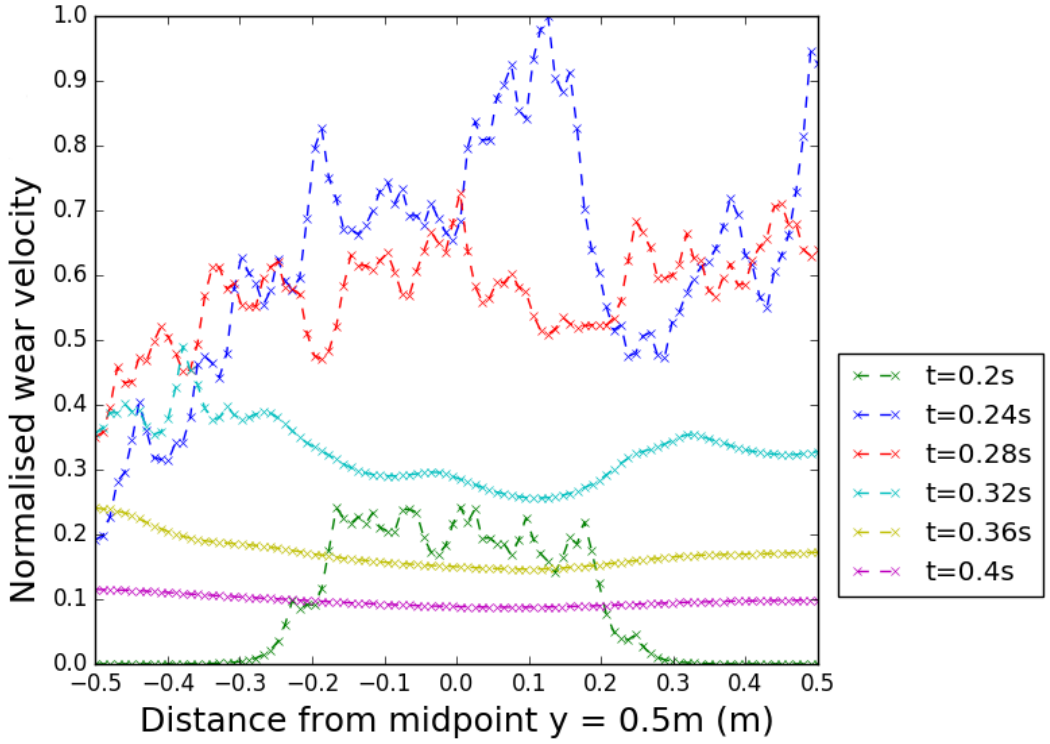

Figure 4.16: Normalised wear velocities at specified times measured at the boundary surface. Wear velocity begins evenly distributed at the jet axis of y = 0.5m. Maximum wear velocity becomes off centre to the axis before settling evenly across the boundary surface at t=0.4s. Normalisation of wear velocity is based on min-max normalisation across all time points.

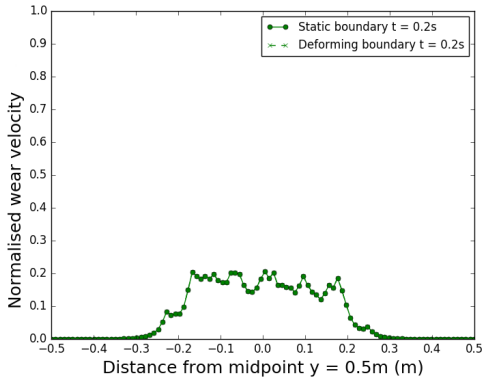

(a) t=0.2s

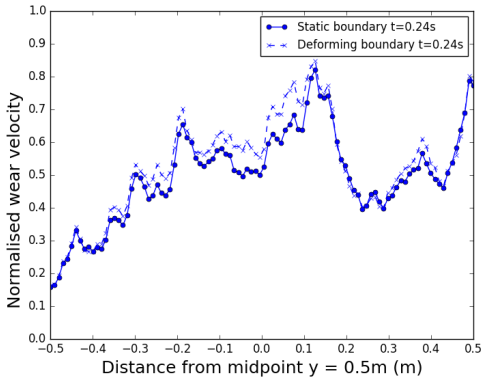

(b) t=0.24s

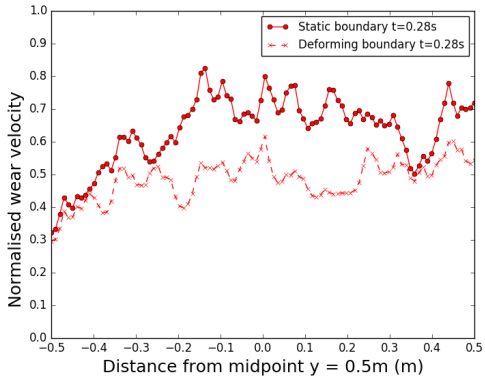

(c) t=0.28s

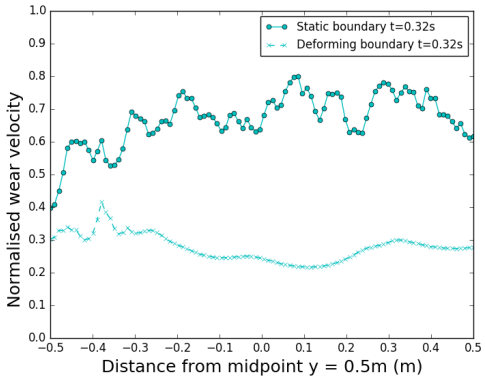

(d) t=0.32s

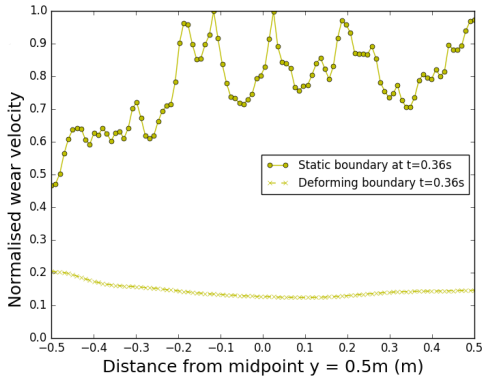

(e) t=0.36s

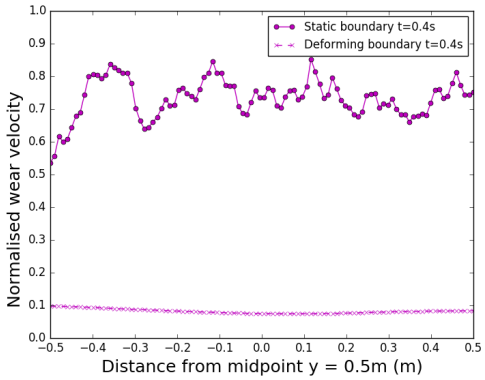

(f) t=0.4s

Figure 4.17: Comparison of normalised wear velocities measured at specified times between static and deforming boundaries. At first impact (t=0.2s), wear velocities between both static and deforming boundaries are equal (shown in green). Normalisation of wear velocity is based on min-max normalisation across all time points and boundary types.

consider surface deformation in response to wear. Whilst it was not possible to directly compare simulation results with that of other models due to the differences in material, particle and fluid properties, this test case was able to confirm the expected behaviour of the wear modelling framework as a whole when considering boundary deformation in response to wear.

4.6 Conclusion

This chapter introduced a wear modelling framework using mesh movement and mesh adaptivity methods. The fluid phase implemented in Fluidity was coupled with a Python based particle module. In addition to the governing equations summarised in 2.5, a series of additional equations for the interpolation of wear rates, particle rebound velocity and particle scaling factors were introduced. The model's correctness was verified through a mesh and time convergence study. Mesh convergence showed that velocity and pressure fields converged at second order as expected from the $P1_{DG}$-P2 element pair while particle volume fraction converged at a rate between first and second order. A time convergence study on a fixed mesh with decreasing time steps was able to verify the temporal discretisation of the θ scheme at $\theta = 0.5$ (Crank-Nicolson) of the fluid phase to be at second order as expected with the scheme. Time convergence of the particle volume fraction calculated using the particle module and coupled with Fluidity displayed a convergence rate between first and second order.

The validation case of particle settling in fluid under gravity provided the ability to validate the accuracy of the particle-fluid coupling where an analytical solution exists through the application of Stokes' law. The wear modelling framework showed the numerical solution compared well with that of the analytical solution through a variety of particle sizes.

The jet impingement case brought together all the particle model components and coupled it with Fluidity to form a wear modelling framework with the ability to deform and move its boundaries in response to wear. This test case highlighted the importance of accounting for surface deformation when modelling wear. Results

of surface wear profiles and wear velocity between static and deforming boundaries displayed the evolution of the wear velocity and surface profile for the deforming boundary whereas the static boundary fields remained at the same magnitude. Both simulations had the same initial wear velocity profile at $t = 0.2$s and the deforming boundary example showed the position of the maximum wear velocity and wear to occur off centre from the jet axis. Whilst it was not feasible to compare results of this numerical simulation with experimental data from literature due to the availability of material properties available for the wear model since it is a semi-empirical model obtained from literature. The jet impingement test case was still able to provide qualitative verification of the entire wear modelling framework in showing the expected behaviour of the wear profile.

Chapter 5

Modelling Multiphase Flow with Boundary Movement in Response to Wear

Contents

5.1 Overview

This chapter introduces the application of the wear modelling framework as described in Chapter 4 validated against the 3 dimensional Coriolis tester arm modelled in the form of the backward facing step. Simulation parameters are first provided before non-deforming boundary simulations are conducted and discussed. Deforming boundary simulations are then conducted and compared with that of the non-deforming boundary case. Finally, the wear modelling framework is then validated using wear profiles of the Coriolis tester rig obtained from lab-based experiments. Results of the numerical simulations show they compare well with that of the available experimental data.

5.2 Simulation Setup

The Coriolis tester arm is chosen to study the effects of the wear modelling framework on a simple but industrially relevant geometry where the geometry and application of the Coriolis tester arm can be extended further to that of complex rotating geometries, such as the centrifugal pump. In addition, the geometry of the tester arm takes the form of a backward facing step which is a commonly used test case for validating CFD code [Imperial College London, 2014]. This configuration includes additional body forces accounting for Coriolis and centrifugal forces experienced in rotating geometries. The governing equations describing the fluid and particle motion in a rotating frame with angular velocity $\boldsymbol{\Omega}$ is given in the form

- Conservation of mass

$$\boldsymbol{\nabla} \cdot (\alpha_f \boldsymbol{u}_f) + (\alpha_p \boldsymbol{u}_p) = 0. \tag{5.1}$$

- Conservation of momentum

$$\begin{aligned} \frac{\partial(\alpha_f \rho_f \boldsymbol{u}_f)}{\partial t} + \boldsymbol{\nabla} \cdot (\alpha_f \rho_f \boldsymbol{u}_f \otimes \boldsymbol{u}_f) + 2\alpha_f \rho_f \boldsymbol{\Omega} \times \boldsymbol{u} = \\ -\alpha_f \boldsymbol{\nabla} p - \alpha_f \rho_f \boldsymbol{g} + \boldsymbol{\Omega} \times \boldsymbol{\Omega} \times \boldsymbol{x} + \mu_f \boldsymbol{\nabla}^2 \boldsymbol{u}_f + K(\boldsymbol{u}_p - \boldsymbol{u}_f), \end{aligned} \tag{5.2}$$

  where $\boldsymbol{x}$ is the position in the rotating frame.

- Particle equation of motion

$$\rho_p \frac{\mathrm{d}\boldsymbol{u}_p}{\mathrm{d}t} + 2\rho_p \boldsymbol{\Omega} \times \boldsymbol{u}_p = \beta(\boldsymbol{u}_f - \boldsymbol{u}_p) + \boldsymbol{g}(\rho_p - \rho_f) + \boldsymbol{\Omega} \times \boldsymbol{\Omega} \times \boldsymbol{r} + \boldsymbol{F}_{KTGF}. \quad (5.3)$$

- Particle position

$$\frac{\mathrm{d}\boldsymbol{r}_p}{\mathrm{d}t} = \boldsymbol{u}_p. \quad (5.4)$$

The Coriolis tester from Weir Minerals consists of a large rotating basin into which a slurry is pumped as well as four arms through which the slurry mixture flows under centrifugal forces. Within each arm resides a polyurethane holder formed into a backward facing step which viewed in the direction of rotation. A sample of the test material is fitted into this holder below the step. Figure 5.1 shows a photo of the Coriolis tester from Weir Minerals with the associated CAD model.

For the simulations presented in this chapter and Chapter 6, simulation conditions and parameters are taken from data available from the laboratory based experiments where possible, with material properties obtained from Arabnejad et al. [2015b]'s wear equation. Experimental results of the Coriolis tester arm are also available for comparison from Weir Minerals and will be discussed in Section 5.4.

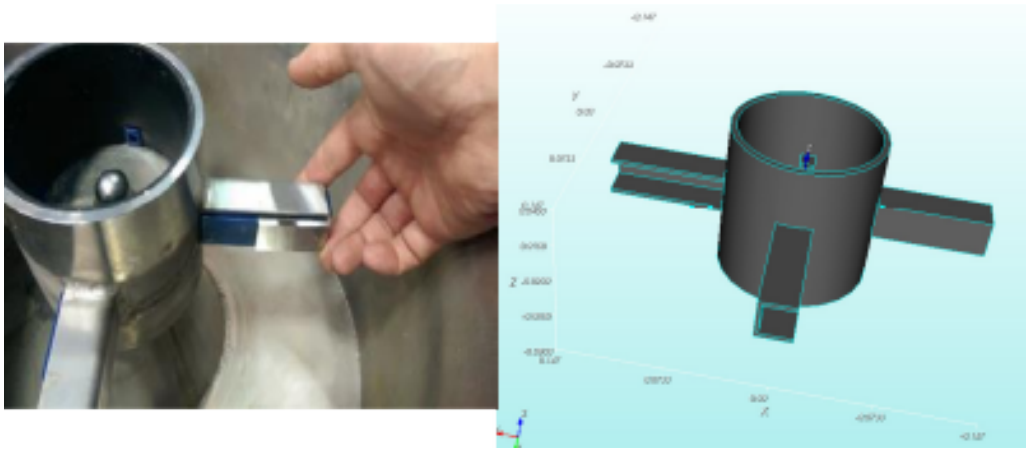

Figure 5.1: Weir Mineral's Coriolis tester and associated CAD model.

5.2.1 Domain, Initial Conditions and Boundary Conditions

The numerical simulation takes place in a three dimension domain defined by the schematic in Figure 5.2, with dimensions taken from the experimental Coriolis tester

arm given in Figure 5.3. Dimensions of the domain based on the schematics are $L_x = 0.092m$, $L_z = 0.006m$, $L_y = 0.008m$, $L_i = 0.0103m$ and $h = 0.002m$. This corresponds to dimensions $0.055 \leq x \leq 0.147$, $-0.005 \leq y \leq 0.003$, $-0.003 \leq z \leq 0.003$ with step height $-0.005 \leq y \leq -0.003$ along $x = 0.103$.

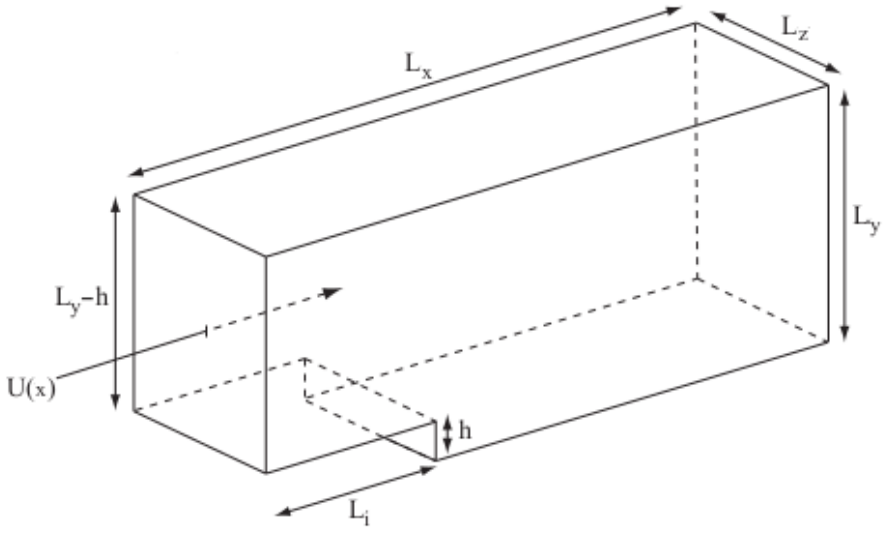

Figure 5.2: Schematic of the domain for the 3-dimensional backward facing step. Image adapted from Imperial College London [2014].

Initial conditions for the fluid velocity at $t = 0s$ and the boundary condition at the inlet is the flow rate for specific particle sizes provided Section 5.2.2. With the velocity profile taking the form $\boldsymbol{u}_x = (0.003 - y)(y + 0.003)$ between $-0.003 \leq y \leq 0.003$. No-normal flow conditions are applied at the step, upper, lower and lateral boundaries with $u = 0$ at the step, $v = 0$ along the upper and lower walls and $w = 0$ along the vertical walls. The boundary condition for the pressure field is that it is set to be zero at the outlet. Figure 5.4 illustrates the initial conditions for the fluid velocity.

The Coriolis force is applied to replicate the rotating Coriolis tester, rotating from the origin existing outside the domain with coordinates (0,0,0) at a speed of 50Hz (3000RPM) with the value taken from experimental set up. Particles are inserted at the inlet in the bottom quarter of the inlet ($-0.003 \leq y \leq -0.0015$) with particle velocities matching that of the fluid at the inlet. This mimics the location of

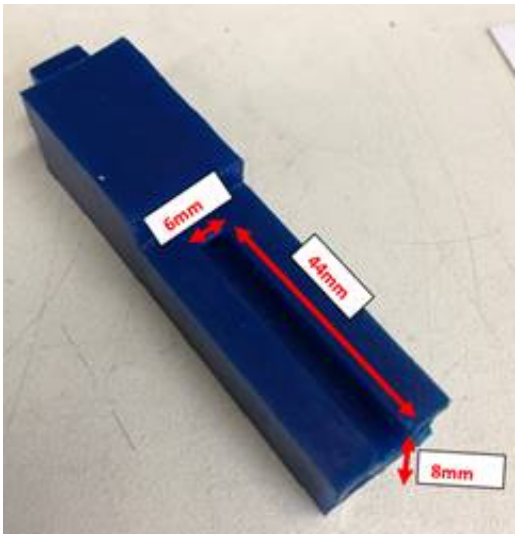

Figure 5.3: Dimensions of the Coriolis tester arm. Image supplied by Weir Minerals.

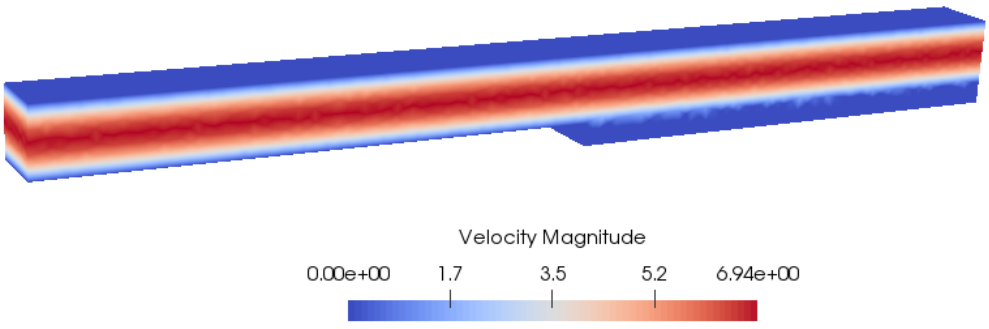

Figure 5.4: Initial fluid velocity profile for the Coriolis tester arm.

particles entering the Coriolis arm tester in experimental conditions as the particles are acting under the Coriolis force. Particles are able to exit the domain either from the inlet or the outlet. The diffusivity factor to smooth out wear as well as the acceleration factor to artificially increase the rate of wear take the default values of 0.001 and 1000 respectively for garnet sized particles. However, analysis of the effect of varying these parameters are discussed and studied in Section 6.2 with the varying values provided as part of the discussion.

5.2.2 Physical parameters

Physical parameters for the particle and fluid used within this chapter is given by Table 5.1 taken from experimental parameters for the Coriolis tester arm. Material properties and their associated empirical constants are provided in Table 5.2 with values taken from Arabnejad et al. [2015b]. The values defined in Table 5.1 and 5.2 represents the default values chosen for the standard simulation configuration. Similarly, the default particle and material for the standard simulation is chosen as garnet sized particles on Carbon Steel 1018. Analysis into the effect of varying these parameters will be studied and discussed in Section 6.2 and any changes in the default values will be provided as part of the study. The particle insertion rate and particle scaling modifier is calculated from solid concentration by weight and fluid flow rate with the equations provided in Section 4.2.3. The particle scaling modifier is required to scale up the number of representative particles in the simulation to match that of the actual number of particles in the system, and the acceleration factor increases the rate of wear so that numerical simulations can be completed over a feasible time frame. The diffusivity factor is required to increase the smoothness of the wear profile, diffusing out the effects of wear from the use of representative particles and acceleration factor.

Parameter	**Garnet**	**Medium sand**	**Fine sand**
Particle diameter, D (m)	1 x 10^{-3}	7 x 10^{-4}	1 x 10^{-4}
Particle density, ρ_p kgm^{-3}	2500	2500	2500
Solid concentration by weight, c_w %	20	20	20
Fluid flow rate, Q_f lmin^{-1}	49.2	34.8	25.2
Fluid density, ρ_f kgm^{-3}	1000	1000	1000
Fluid viscosity, μ Pas	0.001	0.001	0.001
Rotor speed, RPM	3000	3000	3000
Particle insertion rate, s^{-1}	1.4 x 10^5	2.9 x 10^5	7.2 x 10^5
Particle scaling	1	1	100
Diffusivity factor	0.001	0.001	0.001
Acceleration factor	1000	1000	1000

Table 5.1: Physical parameters of particle and fluid properties used within the experimental Coriolis tester arm simulations. particle scaling of 1 for garnet and medium size particle in the simulations denotes each simulated particle is representative of an actual particle.

Parameter	**Carbon Steel 1018**	**Stainless Steel 316**
Material density, ρ_{mat} kgm^{-3}	7870	8000
Cutting erosion factor, C	0.01	0.0125
Vickers hardness coefficient, H GPa	131	224
Particle sharpness factor, F_s	0.5	0.5
Ratio of contact, K	0.4	0.4
Deformation erosion factor, ϵ	4.2 x 10^{11}	1.4 x 10^{11}
Threshold velocity, U_0 ms^{-1}	0.5	5.7

Table 5.2: Material properties with associated empirical constants for wear equation used within the Coriolis tester arm simulations.

5.2.3 Spatial and Temporal Discretisation

For the fluid phase, the continuity and momentum equations are discretised in space using the Galerkin finite element method with the $\mathrm{P1_{DG}}$-P2 element pair. The first order backward Euler method ($\theta = 1$) was used to step the discretised equations forward in time while Fluidity's adaptive time-stepping method was enabled to allow for appropriately sized time steps to be taken after the initial time step of $t = 0.001s$ with a final time step of $t = 0.025s$. A Courant number of 1.5 was selected to enforce the size of the time steps to be taken and within each time step, a maximum of two non-linear time loops was chosen to resolve the non-linearity in the system [Imperial College London, 2014].

For the particle phase, the equations of motion are discretised using an operator splitting method and a second order Adams-Bashforth scheme was used to step forward the equations in time, except for the first time step following particle insertion or particle-wall collision when the explicit forward Euler scheme is used.

5.2.4 Mesh generation and movement

Gmsh [Geuzaine and Remacle, 2009] is used to generate the initial unstructured mesh of the domain composed with a characteristic element length of $l = 0.001m$ as shown in Figure 5.5.

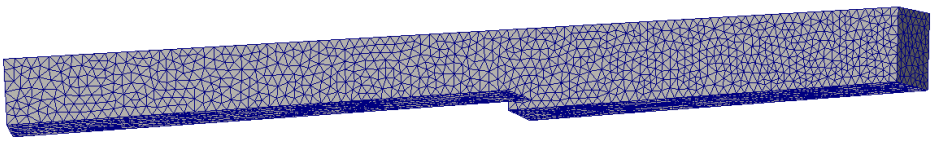

Figure 5.5: Initial mesh for the Coriolis tester arm.

Mesh movement methods using wear velocity as the chosen grid velocity are enabled to allow for the movement of the specified surface in response to wear. The initial surface where boundary deformation can occur along the lower boundary is defined by $0.103m \leq x \leq 0.147m$ $-0.003m \leq z \leq 0.003m$ and $y = -0.005m$. The mesh is set to adapt every 5 time steps to ensure that the mesh remains well formed when deforming in response to wear. The lower and upper bounds on the element size is given as $l_{min} = 0.001m$ and $l_{max} = 0.012m$ respectively. The mesh is set to adapt on wear velocity and continuous fluid velocity to ensure resolution to these fields are adequate where required. Resolution is required for the wear velocity field as this is the solution field defining the rate of boundary deformation. Continuous velocity also benefits from the use of mesh adaptivity to capture the effect of boundary movement and particle interactions.

5.3 Coriolis Tester Arm Simulations

In this section, numerical simulations of 1mm garnet particles with Carbon Steel 1018 over a simulation time of t=0.025s is conducted on both non-deforming boundary and boundaries that deform in response to wear.

5.3.1 Non-deforming boundary

Numerical simulations with non-deforming boundaries are quick to conduct is able to show instantaneous particle-wall impact events which could be used to predict initial areas of interest for wear. The simulation parameters remain the same as that of the deforming boundary, however, the key difference being mesh movement of the boundary is disabled and mesh adaptivity occurs only within the boundary specified at the start. Figure 5.6 shows the impact events for garnet sized particles against the target material of Carbon Steel 1018 at a time of t=0.025s. The profile indicates two main regions of impact. The two regions of impact indicates that the larger garnet sized particles possesses sufficient inertia to move away from the wall post collision in order to make further impacts with the wall. The first region occurs over a smaller surface area at approximately 0.01m from the step, with the second region towards the end of the sample holder covering a wider surface area. The smaller first region can be due to the particles making its initial impact after falling from the step. The wider second region of impact events can be explained by the greater variance of particle velocities and trajectories following its initial impact as particles experience a reduction of momentum following the initial particle-wall collision.

Figure 5.6: Particle-wall impact events for garnet sized particles with target surface material Carbon Steel 1018. The profile is taken along slice z=0 with presence of representative particles at t=0.025s.

Mesh adaptivity can be observed to adapt to the simulation providing the level of resolution required to obtain level of accuracy specified. The number of elements and nodes rapidly decreased from 4494 elements and 17686 nodes converging to 1729 elements and 6665 nodes by t=0.003s as the level of resolution was not required to obtain the results at the specified accuracy (see Figure 5.7). This results in fast

simulations that can be conducted with low computation cost.

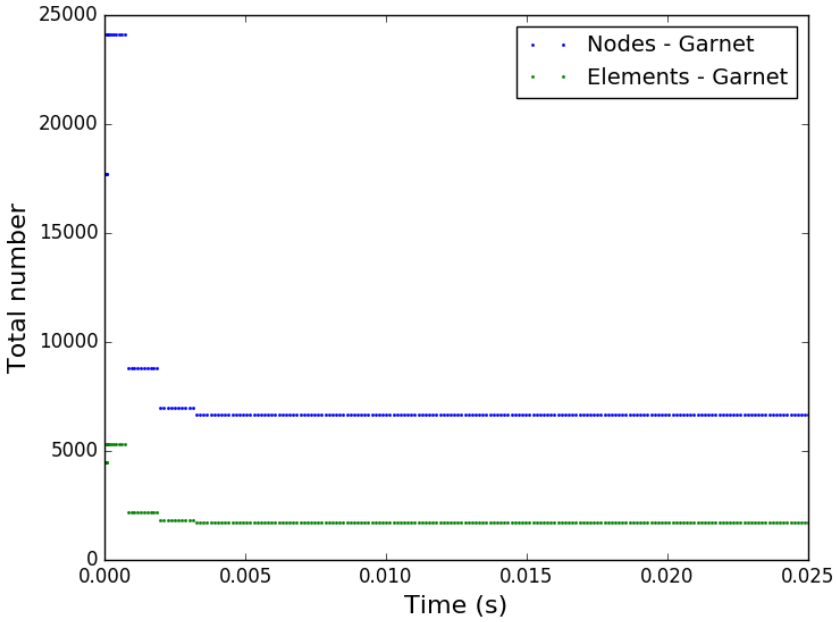

Figure 5.7: Number of elements and nodes within the non-deforming domain with only mesh adaptivity adaptive mesh for garnet particles with target material Carbon Steel 1018.

Whilst non-deforming boundary simulations are quick to conduct and is able to show initial positions of wear based on particle-wall collision events, there is the limitation that it does not take into account the effect of surface profile changes on subsequent particle-wall collision events identified as having a significant impact on wear mechanisms by Nguyen et al. [2014].

5.3.2 Deforming boundary in response to wear

To address the limitations with non-deforming boundaries when considering wear modelling, mesh movement is enabled along the deforming surface. Wear velocity calculated along the deforming boundary surface is chosen as the grid velocity to allow for the movement of the surface in response to wear. The surface wear profile for the default numerical simulation comprising of 1mm garnet particles with Car-

bon Steel 1018 over a simulation time of t=0.025s is given in Figure 5.8. The wear profile is taken as a slice along the midpoint of the domain at z=0, adaptive mesh was enabled with upper and lower bounds defined in Section 5.2.4 on continuous velocity and wear velocity fields. The wear profile shows the maximum wear occurring at around 0.01m from the step with a further region of wear towards the end of the sample holder at approximately half the magnitude as the initial maximum wear. The two regions of wear with differing magnitudes is due to the large garnet particle size possessing greater inertia compared to the drag felt from the fluid. This means that garnet particles are more weakly dampened by the fluid following its first collision after the step observed at x=0.01m from the step and retains sufficient inertia to leave the wall for further collisions with the wall at lower magnitudes before leaving the domain at the outlet. The shallower second region of impact indicates a reduction of momentum post the initial particle-wall collision.

The evolution of the surface deformation is shown in Figure 5.9. Deformation first occurs at first impact after the step from particles falling off the step. At t=0.01s, a second region of wear appears towards the end of the Coriolis tester arm due to subsequent collision with the wall from particles rebounding off the wall after first collision. Two regions of wear increases in depth as time proceeds

The trajectory of garnet sized particles is shown in Figure 5.10. Particle can be observed to rebound off the deforming surface after falling off the step subsequent collision event towards the outlet of the Coriolis tester arm. Figure 5.11 illustrates the behaviour of garnet particles remaining close to the Coriolis tester arm wall before falling off the step, colliding with the deforming surface and rebounding from the surface.

Mesh adaptivity can be observed to provide higher resolutions towards the inlet where particles are first inserted as well as after the step in order to resolve wear and continuous velocities where required. The number of mesh nodes at the start of the is 17686 ending with 22029 nodes and there were 4494 elements at the start and ending with 4944 elements. Element and node resolution increased at the start of the simulation to account for the changes in particle insertion and fluid properties before decreasing to below the initial values as the particles travels along the arm

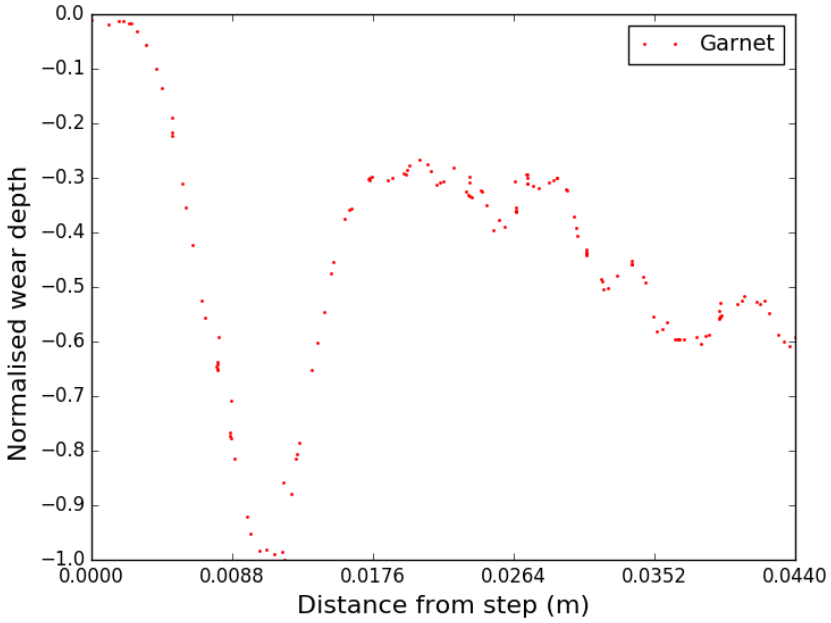

(a) Normalised wear profile

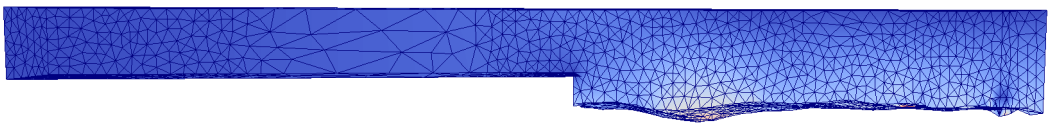

(b) Simulation wear profile mesh

(c) Simulation wear profile

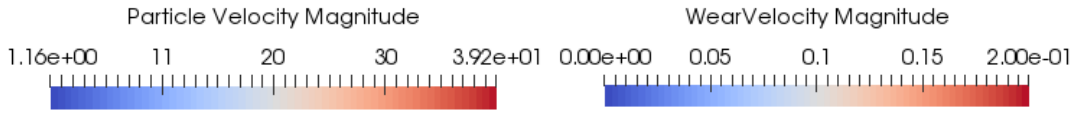

Figure 5.8: Wear profiles for garnet sized particles with target surface material Carbon Steel 1018. (a) shows the normalised wear profile based on distance after the step at x=0.103m. Normalisation of wear depth is based on min-max normalisation. (b) is the 3-dimensional domain with visible adaptive mesh and (c) is the wear profile along slice z=0 with presence of representative particles at t=0.025s.

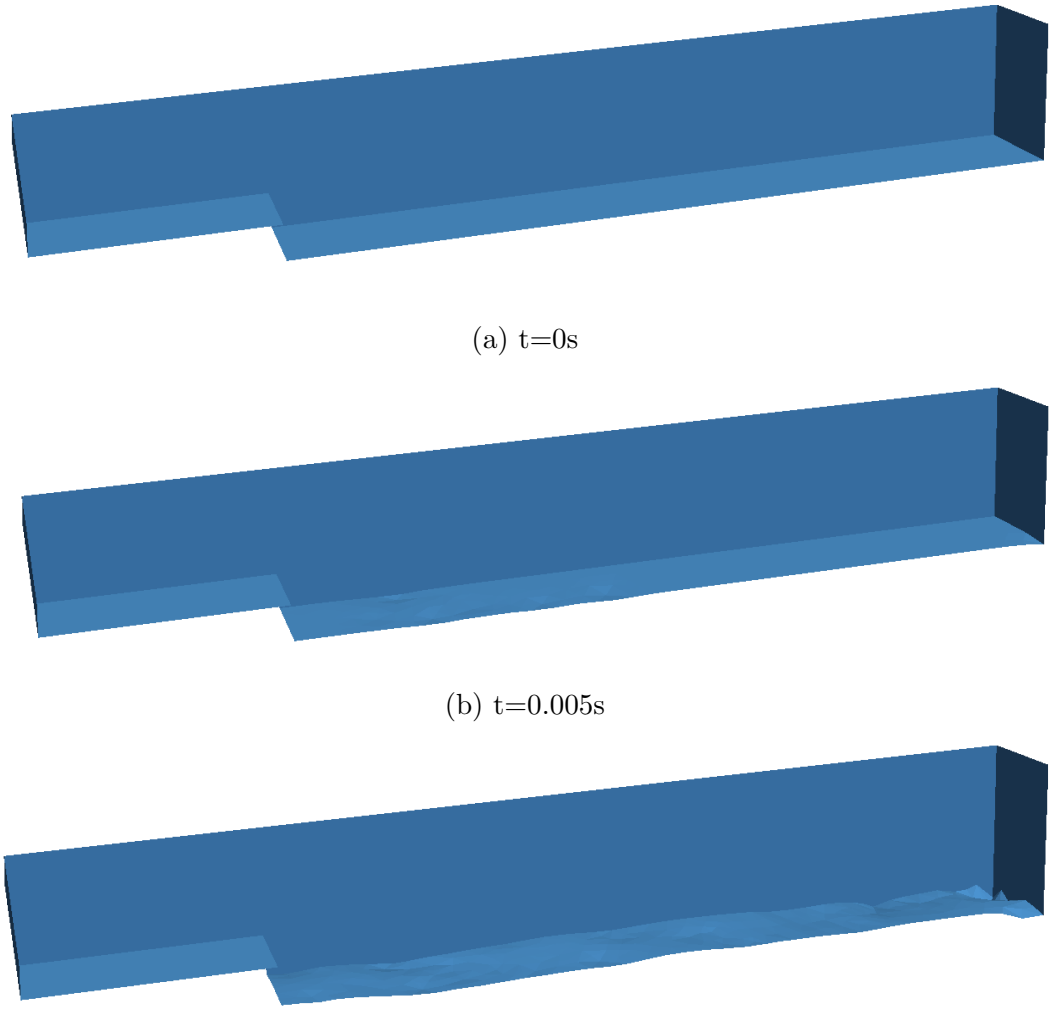

(a) t=0s

(b) t=0.005s

(c) t=0.01s

Figure 5.9: 3 dimensional simulation wear profiles for garnet particles with target surface material Carbon Steel 1018. Time steps of the profiles are taken every t=0.005s.

(d) t=0.015s

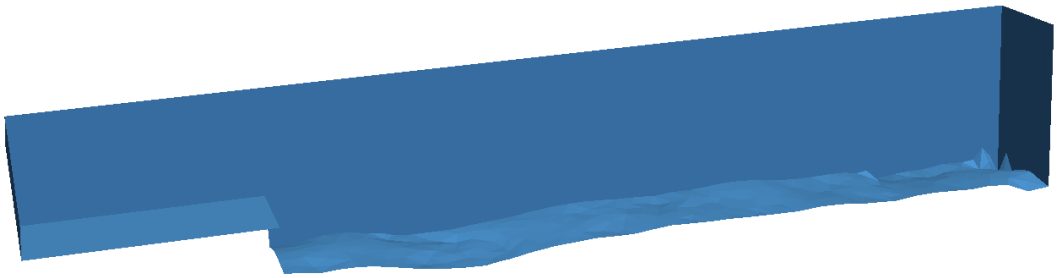

(e) t=0.02s

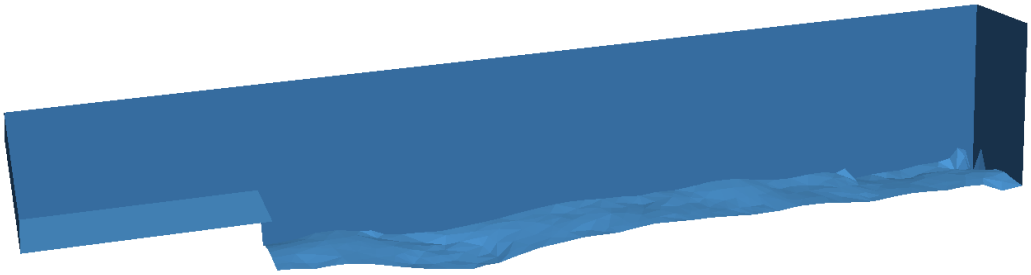

(f) t=0.025s

Figure 5.9: 3 dimensional simulation wear profiles for garnet particles with target surface material Carbon Steel 1018. Time steps of the profiles are taken every t=0.005s.

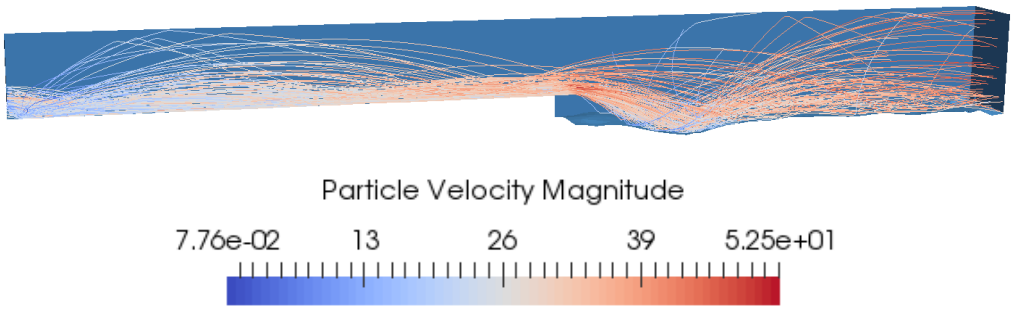

Figure 5.10: A sample of particle trajectory of garnet particles with target surface material Carbon Steel 1018.

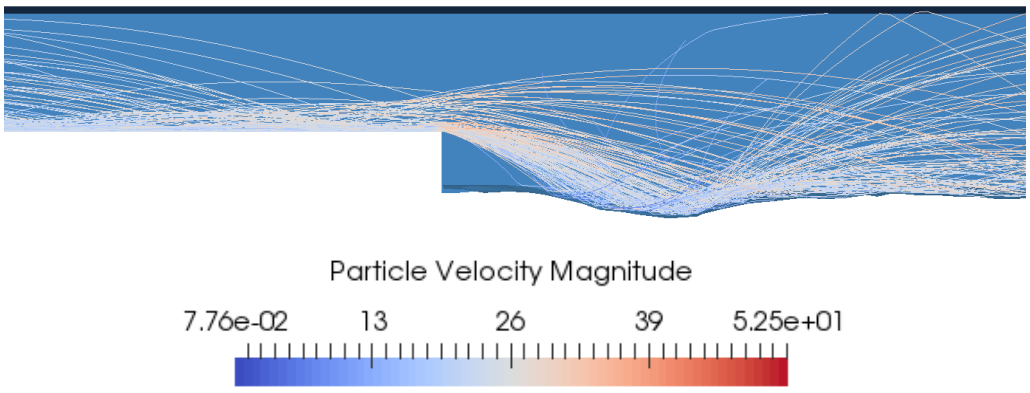

Figure 5.11: A close up cross section of garnet particle behaviour as particles falls of the step making initial impact at approximately 0.01m after the step.

before finally increasing again before t=0.005s as particles begin to fall off the step and initial particle-wall collisions are observed. Both number of nodes and elements are then observed to increase to account for boundary deformation remaining within the region of 20000 nodes and 5000 elements (see Figure 5.12).

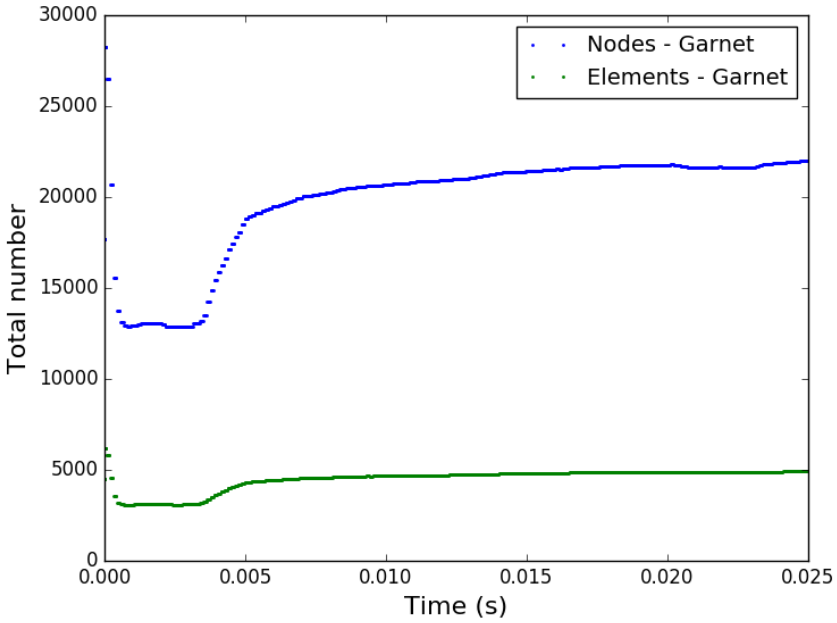

Figure 5.12: Number of elements and nodes within the domain with mesh movement and adaptive mesh for garnet particles with target material Carbon Steel 1018.

5.3.3 Comparison between non-deforming and deforming boundaries

Comparing simulations conducted between non-deforming and deforming boundaries with garnet sized particles on Carbon Steel 1018 revealed that non-deforming boundary simulations are able to accurately predict the initial particle-wall impact events whilst maintaining low computation cost with the use of mesh adaptivity, identifying the correct regions of interest, especially with the location of the first impact from the step.

However, non-deforming boundaries does come with limitations that it does not

take into account the effect of surface profile changes on subsequent impact events. This can be observed when deforming boundary simulations were conducted using the same simulation parameters. At the same simulation time point of t=0.025s. Whilst the point of first impact occurs at the same distance, roughly 0.01m away from the step, the width of this first impact region in the deforming boundary case is greater than that of the non-deforming boundary. This can be due to the particles smoothing our the deforming surface as it rebounds out of the initial region of impact. The comparison between non-deforming and deforming boundaries in response to wear confirms that changes to surface profiles does have an impact on subsequent wear events, therefore initial wear events is not representative of long-term wear profiles. Limitations around element sizes exist for numerical simulations of the non-deforming and deforming boundaries in Sections 5.3.1 and 5.3.2 involving garnet sized particles defined in Table 5.1 using the unstructured mesh provided in Section 5.2.4. It is important to note that the assumption the particle is smaller than the element could be violated as the minimum element size is the same size as that of the garnet sized particle. While this could be problematic and is pushing the limits of the modelling framework, the model is also limited with options to mitigate this issue. Options are to either make the mesh coarser, restricting the model to limited particle sizes based on the mesh or explicitly simulating each of the large particles by resolving the flow around the particle. If the mesh was made coarser, this would sacrifice on the needed resolution of the model to accurately simulate the wear behaviour. Restricting the sizes of the particles is not feasible when applying the model to real-world parameters and requirements. Finally, explicitly simulating each of the particles by resolving the flow around them becomes computationally infeasible. When creating computational models, there will always be a range of sizes where limitations are pushed and restricted, for this case, the limit only is only violated if the mesh adapts to use the minimum grid size.

5.4 Validation with experimental wear scars

Access to experimental wear scars was obtained from Weir Minerals for target material A05HT with density of 7528kgm^{-3}. This section aims to compare the numerical simulation of the Coriolis tester arm against the wear scar obtained from experimentation. As empirical values for the target material A05HT were not available for the wear equation, the results are compared with both Carbon Steel 1018 with a density of 7870kgm^{-3} and Stainless Steel 316 with a density of 8000kgm^{-3}. Slices along the z-axis were taken at regular intervals between z=-0.015m, z=0m and z=0.015m. A particle size of 1mm, a fluid flow rate of 49.2lmin^{-1}, a 20% solid concentration by weight with a Coriolis force rotating at a speed of 3000RPM matches that of the experimental conditions.

Figure 5.13 illustrates the wear profile scars from experimental data which was scanned and processed with wear depth measured along the sample. Figure 5.14 illustrates the equivalent numerical simulation wear profile in the shape of the 3d backward facing step with dimensions of the domain matching that of the experimental Coriolis tester arm.

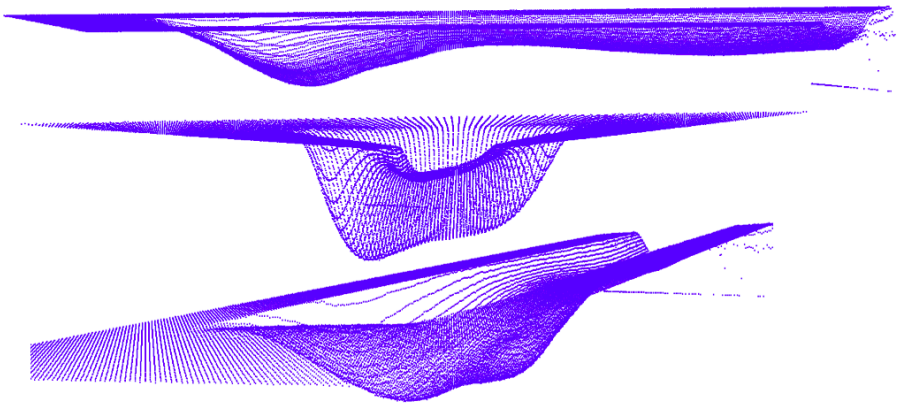

Figure 5.13: Wear profile of experimental Coriolis tester arm for garnet particles with material A05HT

The results and comparison of the normalised wear profile between experimental A05HT and numerically simulated Carbon Steel 1018 is presented in Figure 5.15. Three slices are taken, each represented by its individual plot within the figure. The

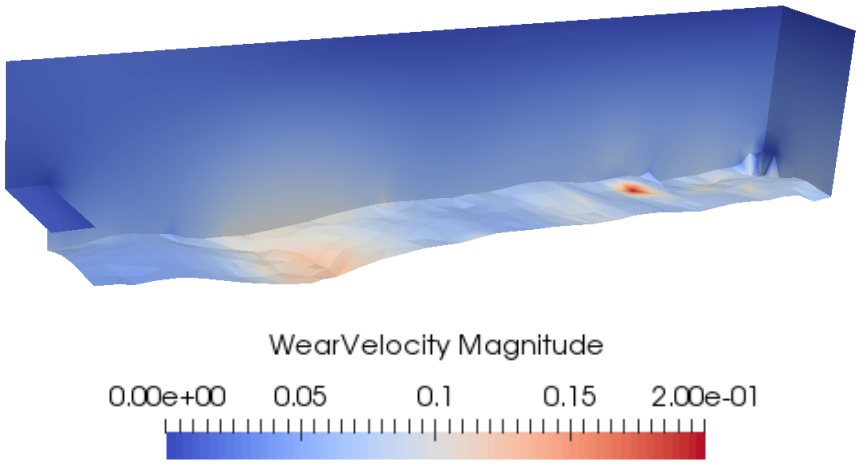

Figure 5.14: Simulation wear profile of 3d backward facing step for garnet particles with Carbon Steel 1018

maximum normalised wear depth for the first wear region contributed by the first impact after the step is represented well in magnitude between experimental and simulated results, however there is a slight offset in the location of maximum wear across slices z=0 and z=-0.015. In simulations across all 3 slices, a second wear region of approximately half the magnitude of the first is present towards the end of the Coriolis tester arm which tracks well with experimental data in both magnitude and position along z=-0.015 and z=0. Along z=0.015 in the experimental data, there fails to be a second region of wear, this can be seen in Figure 5.13 where there is a distinct off set towards the left of the wear profile possibly due to the presence of additional body forces experienced during the experimental run or by the wear modelling framework assumed to have point particles while the real particles are of finite size and so less able to counter the Coriolis of the system.

The effects of finite sized particles on wear profile is shown in Figure 5.16 wear a birds eye view of the experimental wear profile for target material A05HT shows a boundary around the sample holder wear no wear occurs. Furthermore, the two distinct regions of wear exhibits a curved wear pattern towards the end explained by finite sized particles rebounding off the lateral walls towards the centre of the Coriolis tester arm. As seen in Figure 5.17, these effects are not present in the wear

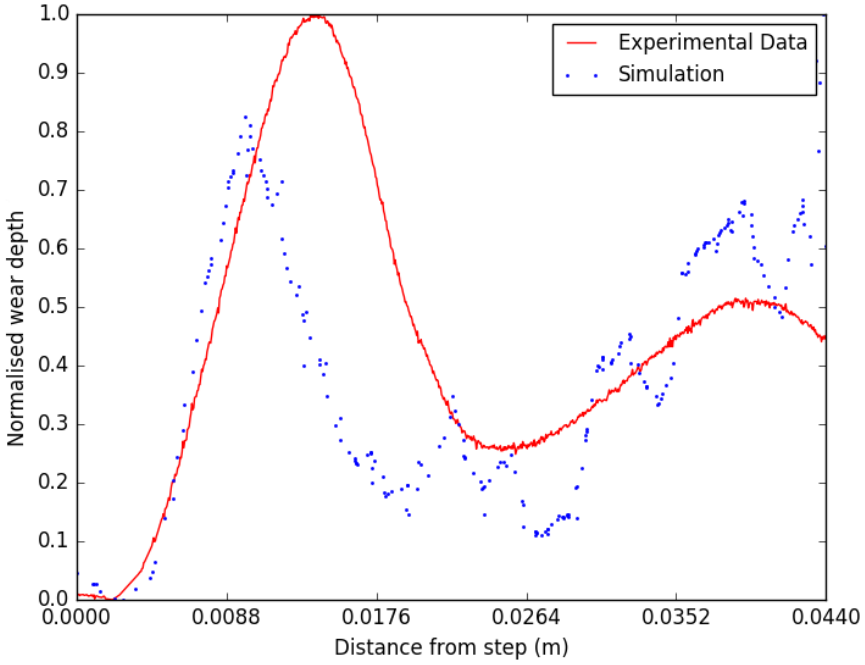

(a) z=-0.015m

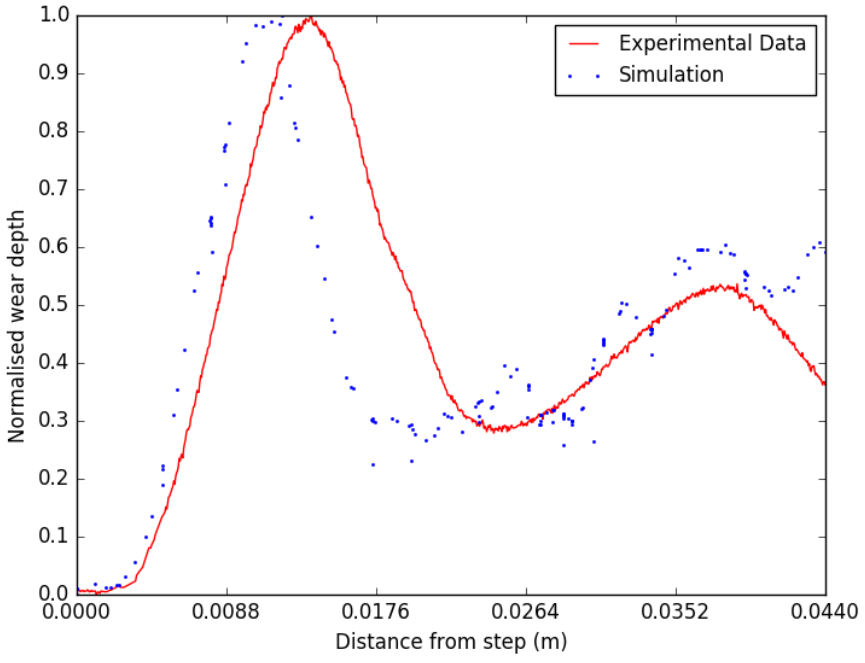

(b) z = 0.0m

Figure 5.15: Comparison of wear profiles between simulation target material Carbon Steel 1018 and experimental target material A05HT. Wear profiles taken at regular slices at z = -0.015m, z=0m and z=0.015m. Normalisation of wear depth is based on min-max normalisation across experimental data and numerical simulation normalised for each slice.

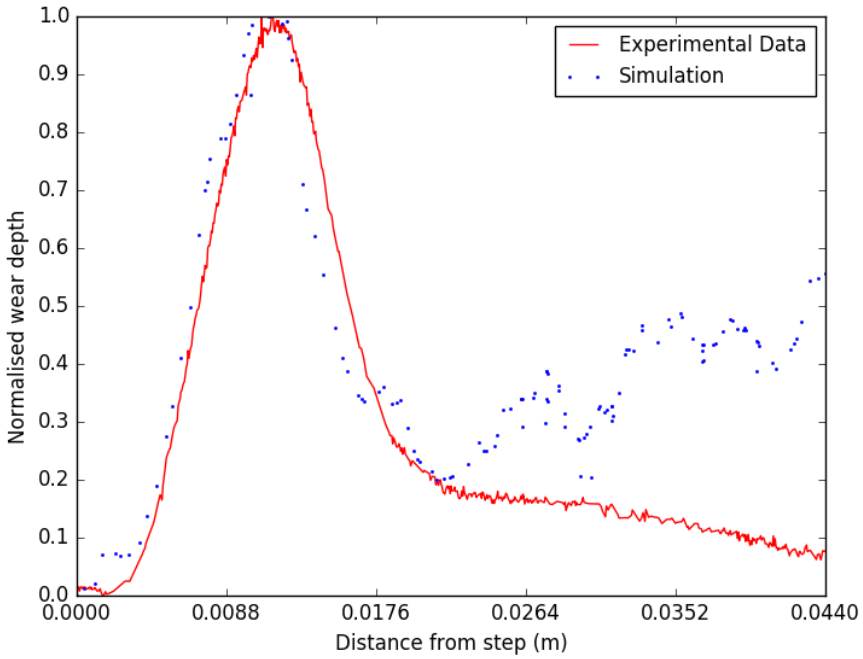

(c) z=0.015m

Figure 5.15: Comparison of wear profiles between simulation target material Carbon Steel 1018 and experimental target material A05HT. Wear profiles taken at regular slices at z = -0.015m, z=0m and z=0.015m.

modelling framework and could be due to both non uniform inlet flows and the finite size of the particles compared to the assumed point particles in the simulations.

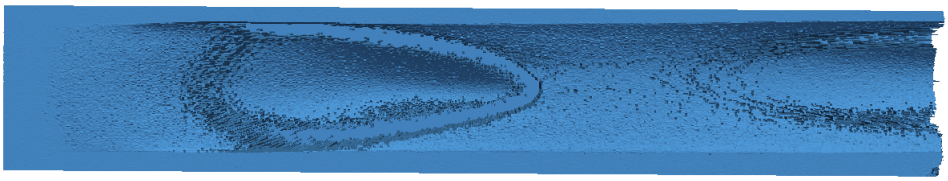

Figure 5.16: Birds eye view of wear profile scan for experimental target material A05HT with garnet particles. Each of the two wear regions is seen to curve and taper towards the end due to particles in experimentation to be of a finite size rebounding of the lateral walls. A boundary around the edges of the surface where no wear is present can be seen.

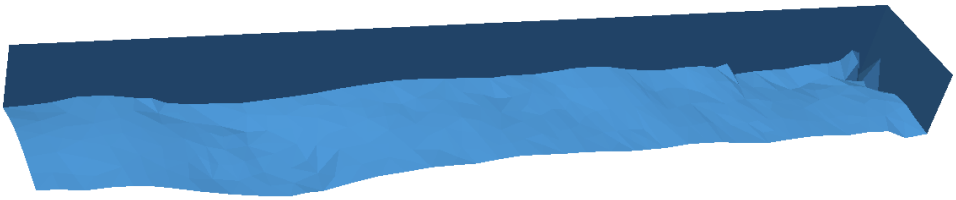

Figure 5.17: Numerically simulated 3D wear profile for Carbon Steel 1018 with garnet particles. Wear profile is evenly distributed across the channel of the Coriolis tester arm with wear occurring to the edges of the surface material.

Comparison with different material properties with the experimental wear data, Figure 5.18 shows both materials identified two distinct regions of wear predicting the rebounding of particles post particle-wall collision for further impacts with the surface. Similar position of maximum first impact is visible between simulated and experimental data. Stainless Steel 316 displays a smaller magnitude of wear compared to that of Carbon Steel 1018 and A05HT. This is due to the Vickers hardness of Stainless Steel as the cutting erosion factor within the wear equation is a function of hardness Hv (Equation 2.35) as the hardness of Carbon Steel 1018

and Stainless Steel 316 is differs by nearly a factor of 2 [Arabnejad et al., 2015b]. As well as the larger Vickers hardness for Stainless Steel 316, it also has an higher threshold velocity for deformation erosion factor by a factor of 10 when compared to that of Carbon Steel 1018. Discussion of the effect of material properties can be found in Section 6.2, however from the wear profile comparison presented in Figure 5.18, target material A05HT can be said to have more similar material properties with Carbon Steel 1018

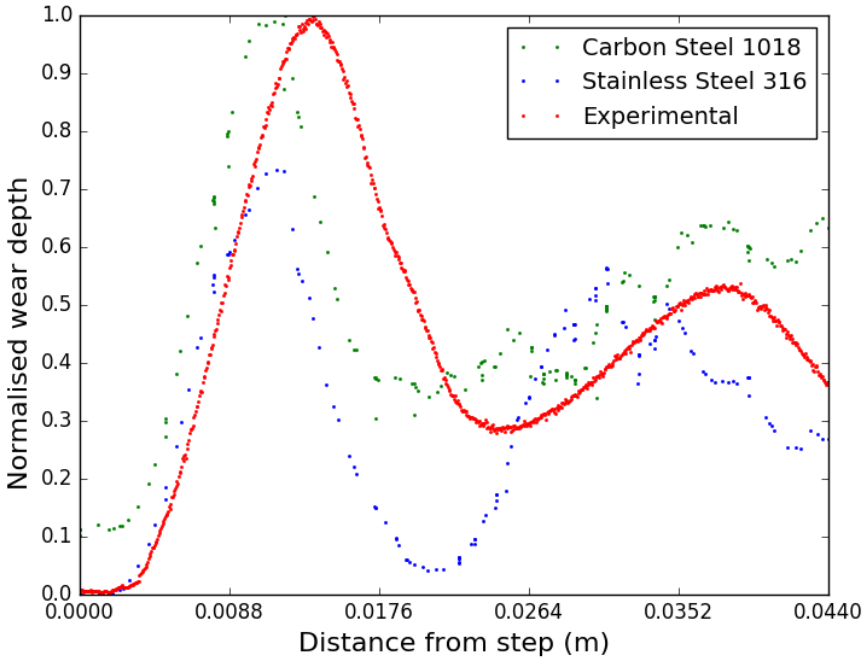

Figure 5.18: Comparison of wear profiles between Carbon Steel 1018, Stainless Steel 316 and experimental target material A05HT for garnet particles. Profile taken along z = 0. Normalisation of wear depth is based on min-max normalisation across all wear profiles at z=0.

5.5 Conclusion

In this chapter, all individual components of the wear modelling framework were combined and applied in an in depth study of wear in the form of the Coriolis tester arm. This study involved a fully coupled multiphase model with the use of representative Lagrangian particles to provide particle trajectory information, wear erosion modelling and the use of mesh movement and adaptive mesh technology from Fluidity for the movement of boundary in response to wear. Limitations of the model involving the choice of element size for the larger particles was discussed. The Coriolis tester arm took the form of a 3 dimensional backward facing step, a common geometry used in the validation of CFD code and the behaviour of garnet sized particles against Carbon Steel 1018 was studied and compared to that of experimental results.

Simulations involving non-deforming boundaries were able to accurately show the initial areas of wear based on particle-wall collisions, it does not take into consideration the effect of surface profile changes on subsequent wear events when considering long term wear profiles. This was evident when comparing against the deforming boundary simulation under the same simulation conditions, where position of the first impact after the step was well predicted, however, the evolution of the surface profile as it begins to spread and over a wider region as time progressed failed to be captured in that of the non-deforming boundary case. Therefore, initial wear impact events is not representative or suitable for the prediction of long term wear. This result agrees with the findings of Nguyen et al. [2014] and demonstrates the importance of considering the evolution of the surface profile as behaviour of the particles and its subsequent wear is sensitive to its change.

Numerical simulations of Carbon Steel 1018 were able to leverage the particle and flow conditions as that of the experimental data for A05HT when conducting wear profile comparisons between experimental data and numerical simulations. However, there was a challenge between the material properties available for the experimental results and material properties available for the wear model since the wear model is a semi-empirical model obtained literature. Best efforts has been made to match that

as closely as possible and the behaviour of different material properties are discussed in Chapter 6. Nevertheless comparison of wear profile against experimental data for A05HT showed good agreement with magnitude of maximum wear after first impact along z=0 and z=0.015.Position of maximum wear was also good along z=0.015 but off set for z=0 and z=-0.015. The second region of wear was well predicted in both depth and position along z=0 however, no second area of wear was present in experimental data at z=0.015 as the experimental wear profile exhibited a bias towards the left of the sample material.

Chapter 6

Studying the effect of varying model and physical parameters

Contents

6.1 Overview

This chapter continues the work presented in Chapter 5, where the numerical simulations of the Coriolis tester arm is expanded to include the study and exploration of simulation parameters. It begins with a sensitivity analysis of the wear modelling parameters involving critical impact angle, acceleration factor and diffusivity factor. Simulations involving the study of the behaviour of physical parameters such as particle size, solid concentration and material properties is presented in this chapter.

6.2 Sensitivity analysis of modelling parameters

This section studies the sensitivity of modelling parameters that forms the wear modelling framework. These parameters include the critical impact angle, K, which determines the impact angle where maximum wear occurs, the acceleration factor which artificially scales up the rate of wear and the diffusivity factor which determines the spread at which each wear event is smoothed out in time and space when working with representative particles.

6.2.1 Critical impact angle

The ratio of contact (K) is the ratio of vertical to horizontal contact area of the particle as it impacts the material surface with the maximum wear occurring at the critical angle of $tan^{-1}K$. If the impact angle is greater than this critical angle, then the first equation of Equation 2.36 applies and the particle will have a velocity component in the horizontal direction. Otherwise, the horizontal component of the velocity will decrease to zero earlier with the application of the second equation in Equation 2.36 [Arabnejad et al., 2015b]. K is obtained experimentally and takes a value of 0.4 for most materials eroded with sand. Varying the value of K allows for the study of the critical impact angle and its affect on the erosion equation.

Figure 6.1 illustrates the L2 norm of the erosion factor composed of cutting

erosion factor and deformation erosion factor across the simulation domain given by Equation 2.39. It can be observed that the maximum erosion factor occurs at K=0.4 equivalent to impact angle $\tan^{-1}(0.4) = 21.8^{o}$. Although direct comparison with the experimental data presented in literature from [Arabnejad et al., 2015b] cannot be made due to varying experimental parameters with differing flow conditions, particle size and impact velocities, there is fair agreement in the profile of the erosion factor provided in Figure 6.2.

The erosion factor compared to the Arabnejad et al. [2015b]'s data for Carbon Steel 1018 with particle impact velocity of $28 ms^{-1}$ and sand particles of size $150 \mu m$ has a maximum erosion factor of 3.8 x 10^{-5}. This is an order of magnitude smaller than the erosion factor of 4.5 x 10^{-4} obtained in this thesis for Carbon Steel 1018 with garnet particles of size 1mm. The difference in erosion factor can be explained by the order of magnitude increase in size between the particle sizes in those experiments compared to the particles in these simulations. Whilst there is fair agreement between the relationship between ratio of contact and erosion factor between 6.1 and 6.2, it is important to remember that these values are obtained empirically and would generate uncertainty when extrapolating the data for other test cases.

6.2.2 Acceleration scaling

Acceleration scaling artificially scales up the rate of wear thus reducing the time taken to study wear profiles when compared to the study of wear in the field or experimentally. Four acceleration factors were chosen comprising of acceleration factors of 100, 500, 1000 and 2000 where the factor of 1000 is the default value used elsewhere in this thesis.

Figure 6.3 shows the normalised wear profiles at increasing acceleration factors taken at t=0.025s. The overall wear profile with two distinct regions of wear is not affected at acceleration factors of 100, 500, and 1000, however, it is impacted at the highest simulated acceleration factor of 2000. This shows that acceleration factor does have an impact, as increasing the acceleration scaling of each representative particle increases the significance of the coupling between the local fluid and wear. At

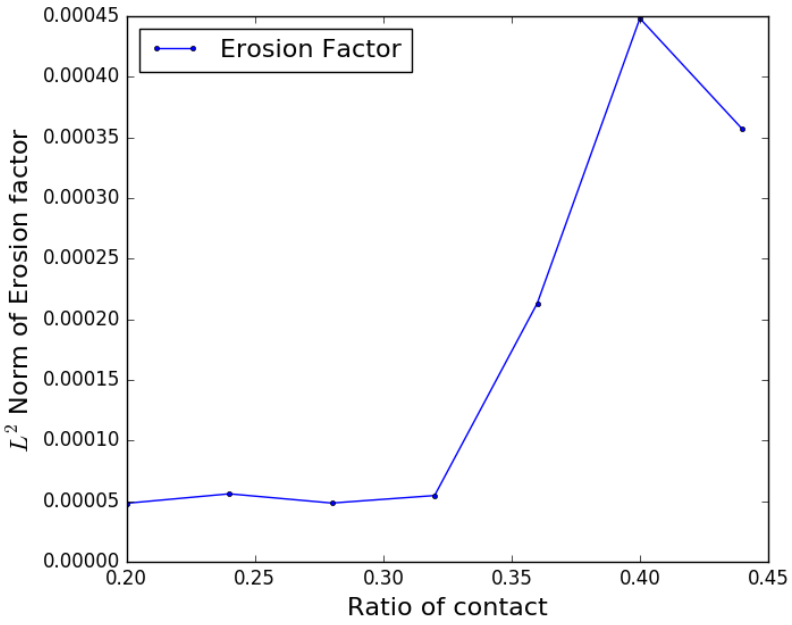

Figure 6.1: L^2 norm of erosion factor at varying ratios of contact. Maximum erosion factor is observed at K=0.4 which is equivalent to impact angle $\tan^{-1}(0.4)$.

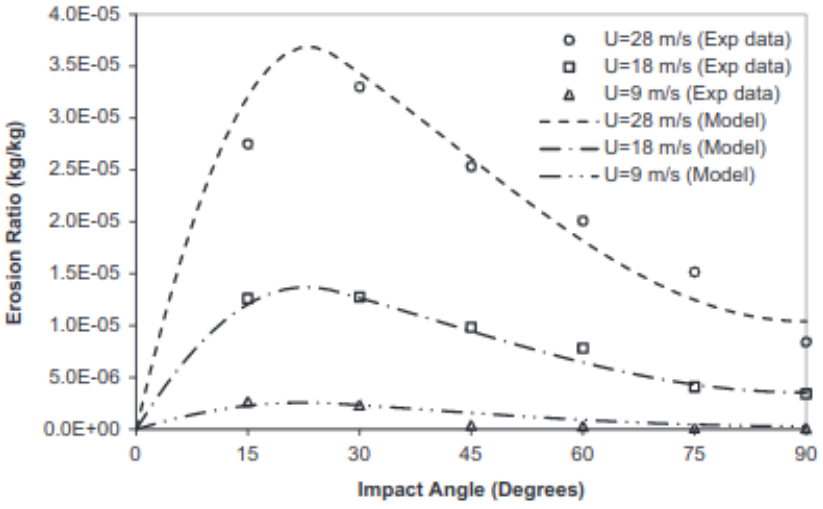

Figure 6.2: Erosion ratio of Carbon Steel 1018 at different impact velocities and angles. Image taken from Arabnejad et al. [2015b].

an acceleration factor of 2000, the increased wear depth observed furthest away from the step can be explained by the fact that each wear event experienced by a single representative particle is removing material 2000 times faster, thus causing an effect on the coupling between the short term fluid flow and drag. As a result one local eddy experienced upstream can create a greater influence of other's downstream. This indicates that the chosen acceleration factor of 1000 is within the right time scale and did not affect the behaviour of the particle-fluid and particle-particle interactions. The maximum wear depth observed at first impact shows a good correlation with the increase in acceleration factor as doubling the acceleration factor doubled the wear depth.

Figure 6.4 confirms the similar behaviour when considering overall volume loss within the domain, however it trends at a rate below first order with volume loss increasing at a factor of 1.5 as acceleration factor doubles. Similar behaviour is also observed when comparing between acceleration factors of 100 and 1000 as volume loss increased at a factor of 6.7 as acceleration factor increased by an order of magnitude. This is due to the fact that particles are also subject Coriolis forces, gravity and inter phase interactions affecting the particle trajectory and the subsequent wear relationships. An offset in time can be observed in Figure 6.4 associated with the time taken for first impacts to occur resulting in volume loss, it is important to note that this time is independent of the acceleration factor.

Verifying the time taken to reach a specified wear depth Figure 6.5 confirms a similar relationship between acceleration factor and time taken to reach a specified wear depth measured at set points in the domain as with acceleration factor and volume loss where the time taken to reach a specified depth decrease by a factor of $\frac{2}{3}$ as acceleration factor doubles at $x = 0.007m$ from the step. At $x = 0.01m$ from the step, the change in time taken at acceleration factor of 2000 can be explained by the fact that the acceleration factor is now causing an effect on the coupling between the particle and the fluid where local changes upstream can have a greater influence on wear downstream and results are no longer independent of acceleration factor.

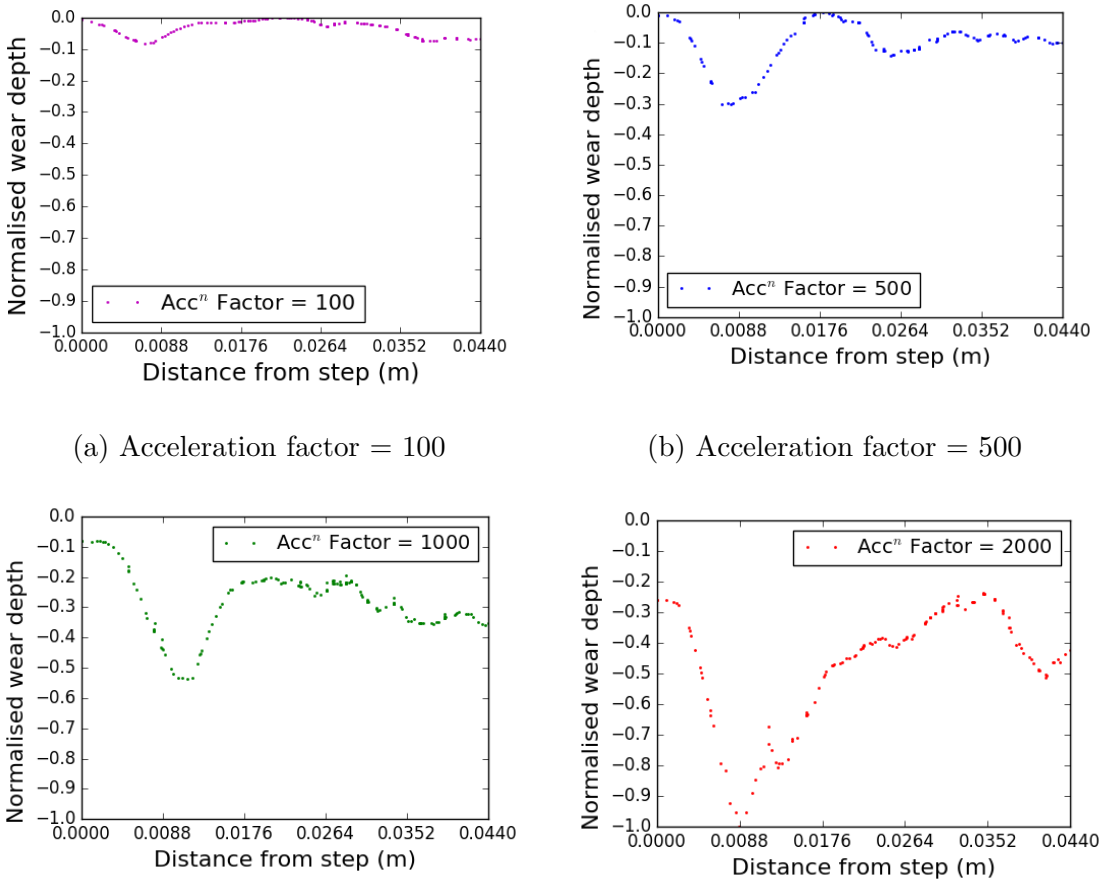

(a) Acceleration factor = 100

(b) Acceleration factor = 500

(c) Acceleration factor = 1000

(d) Acceleration factor = 2000

Figure 6.3: Normalised wear profiles at varying acceleration factor for Carbon Steel 1018. Wear profiles taken at t=0.025s. Normalisation of wear depth is based on min-max normalisation across all acceleration factors.

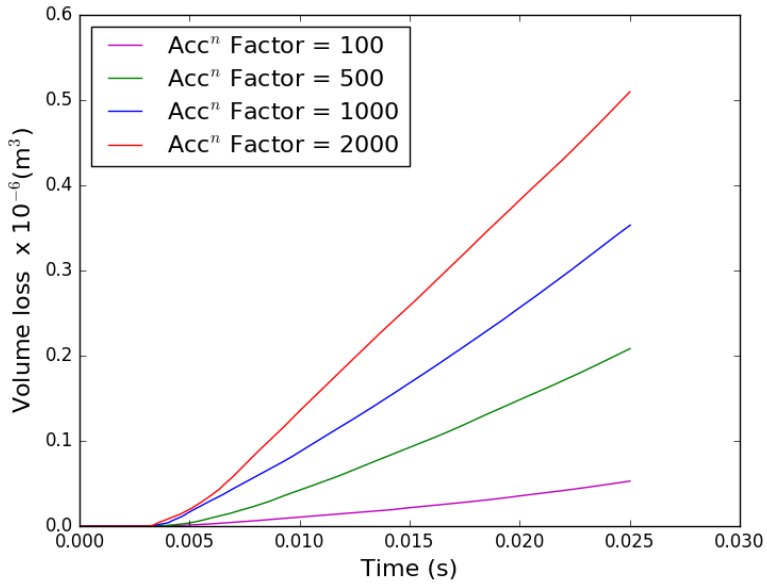

Figure 6.4: Total volume loss at with varying acceleration factors using garnet particles on Carbon Steel 1018 over time.

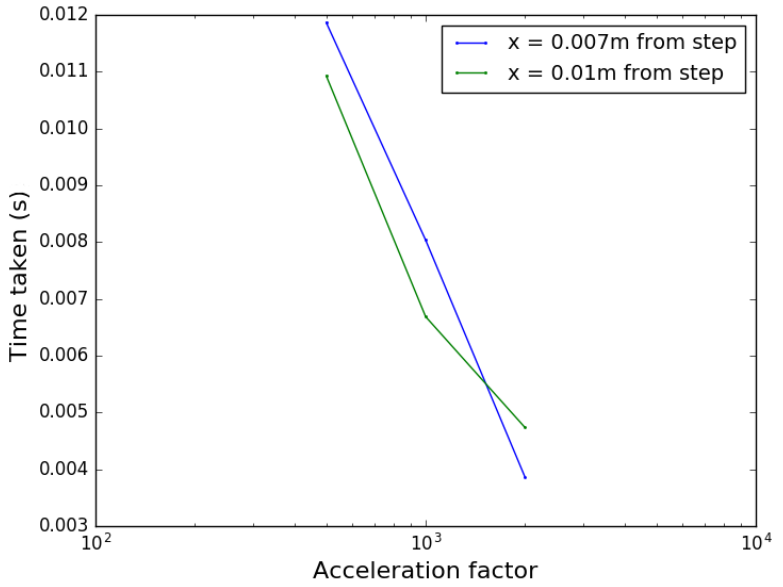

Figure 6.5: Time taken to achieve a wear depth of 0.0005m at varying acceleration factors with wear depth measured at x=0.007m and x=0.01m from the step.

6.2.3 Diffusivity factor

The diffusivity factor determines the the spread with which each wear event is smoothed out in time and space. It is used to smooth out the time scaling as well as particle scaling driving the wear rate as outlined in Section 4.2.3. A study of varying factors consisting of 0.0005, 0.001, 0.002 and 0.004 with the default values used in the simulations being 0.001. Lower values of diffusivity factor would result in less smoothing of each wear event through time and space.

Figure 6.6 shows the normalised wear depth for varying diffusivity factors for garnet particles. For garnet sized particles, while each simulated particle is representative of an actual particle (Table 5.1), there is still an acceleration factor which would need to be smoothed out in time and space. Lower diffusivity factors has the sharpest and greatest wear profile compared to the smoother wear profiles that are lower in magnitude at higher diffusivity factors. This is due to the use of representative particles, where each particle in the simulation is representative of a larger number of particles in the actual system. Therefore each wear impact from a simulated particle is equivalent to the wear impact for a larger number of particles in the actual system and would need to be spread out in time and space accordingly.

A lower diffusivity factor would spread the impact of wear across a smaller distance and time than a larger diffusivity factor resulting in the behaviour observed. However, while large values of the diffusivity factor may increase the smoothness of the wear profile, reducing the impact of a single wear event, it comes at the cost of sensitivity to the genuine variation within the wear profile. This effect is evident from Figure 6.6, the diffusivity factor of 0.004 has a smooth wear profile throughout the domain, however, it has lost its distinct second region of wear created by subsequent particle-wall collisions. Appropriate diffusivity factor should be chosen based on the combination of acceleration factor and particle scaling used within the simulation and ideally verified against available experimental data.

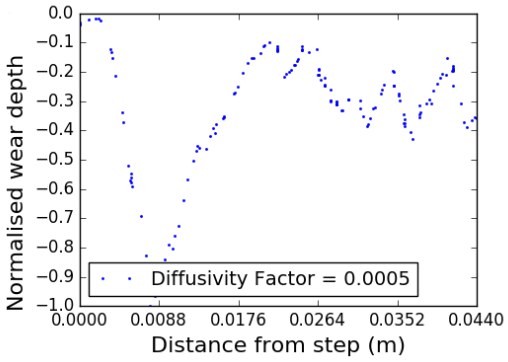

(a) Diffusivity factor=0.0005

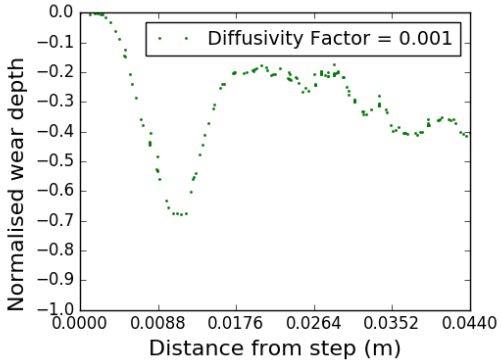

(b) Diffusivity factor=0.001

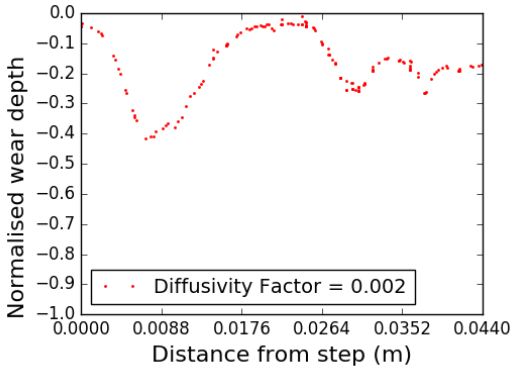

(c) Diffusivity factor=0.002

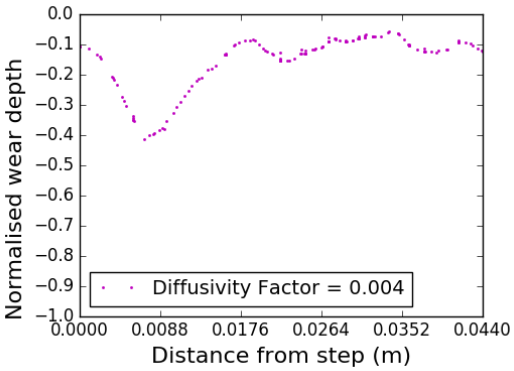

(d) Diffusivity factor=0.004

Figure 6.6: Normalised wear profiles at varying diffusivity factor for Carbon Steel 1018 with garnet particles. Wear profiles of the slice is taken from the midpoint z=0m at a time point of t=0.025s. Normalisation of wear depth is based on min-max normalisation across all diffusivity factors.

6.3 The effect of varying physical parameters

The section studies the effect of varying physical parameters and its effect on the subsequent wear profile. The physical parameters include particle sizes, target material properties and solid concentration. Two additional particle sizes are introduced and compared to that of the garnet particle presented in Section 5.3.2, target material properties looks at the wear profile of Stainless Steel 316 and compared to that of Carbon Steel 1018, both these material properties are obtained through empirical data from literature [Arabnejad et al., 2015a]. Finally, a range of solid concentration and its behaviour on the wear profile surface is conducted for garnet particles on Carbon Steel 1018.

6.3.1 Particle size

Variations in particle sizes are studied and compared with that of the standard garnet particle simulations. Particle sizes consists of fine sand, medium sand and garnet particles with sizes and parameters provided in Table 5.1. Particle insertion rate was calculated using fluid flow rate and solid concentration, particle scaling of 100 is applied to fine sand particles in order to artificially scale up to account for the total number of actual particles in the system due to the use of representative particles.

In Figure 6.7, medium sand particles exhibits a similar wear profile to that of garnet particles where two distinct regions of wear can be observed due to the ability of these larger sized particles to retain sufficient inertia to leave the wall for further particle-wall collisions. The adaptive mesh generated displays a similar pattern where greater resolution is present towards the inlet and then again from the step onwards as the mesh is providing greater resolution for wear velocity field and the deforming boundary. The position of maximum wear corresponds with the location of first impact as the particles fall off the backward facing step. Figures 6.8 shows the evolution of the surface wear profiles at t=0.005s increments. First impacts with visible wear after falling off the step is visible from t=0.01s. This is off a smaller magnitude to the wear observed for garnet particles in Figure 5.9. Two

distinct regions of wear is still observed by time t=0.025s for medium particles. The trajectory of medium sand particles is shown in Figure 6.9, some erratic particle rebounds are still observed similar to that for garnet particles in Figure 5.11 along with the second impact from the rebounding particles. However, the trajectory of medium sand particles remained closer to the wall as the smaller sized particles are less able to oppose the Coriolis force imposed on the particles.

Fine sand particles are an order of magnitude smaller in diameter than that of the garnet particles simulated in the thesis and displays a different set of wear profile and particle behaviour than that of the larger garnet and medium sand particles. Figure 6.10 displays the 3 dimensional wear profile over time. As expected, first surface deformation is observed at first impact after the step at a smaller magnitude compared to medium sand and garnet particles. However, no two distinct regions of wear appear over the same time frame that was observed with the larger particle sizes discussed above. Figure 6.11 displays a slowly decreasing wear depth after first impact from the step with maximum wear at about 0.03m from the step compared to garnet and medium sand particles with maximum wear at about 0.01m from the step. This is because small particles exhibits an almost dependence on the Coriolis force due to its size, with their momentum dampened by drag forces immediately after initial particle-wall collision, they do not possess sufficient inertia from the wall for further impacts. Thus, they remain closer to the wall for the remainder of the time producing wear through a sliding motion against the wall. This behaviour can be observed in the trajectory of fine sand particles in Figure 6.12.

Equivalent figures and discussions presented for medium and fine sand particles is available for the garnet sized particle in Section 5.3.2, specifically Figures 5.9, 5.8 and 5.11.

Figure 6.13 compares the normalised wear profile of fine sand, medium sand and garnet particles for Carbon Steel at t=0.025s. Garnet particles can be observed to have the greatest maximum wear and subsequent wear profile post initial collision as expected for larger particles. Medium sand has similar wear profiles with two regions of impact like that of garnet particles. For both garnet and medium sand particles the second region of impact closer to the outlet of the domain is around

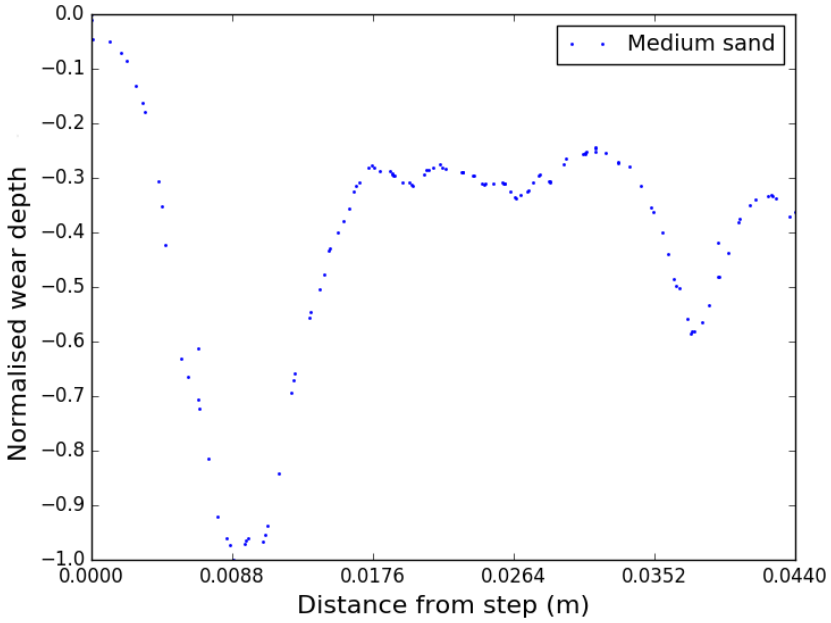

(a) Normalised wear profile

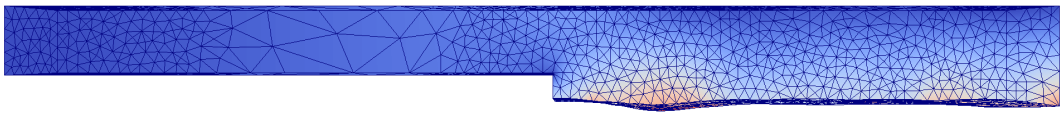

(b) Simulation wear profile mesh

(c) Simulation wear profile

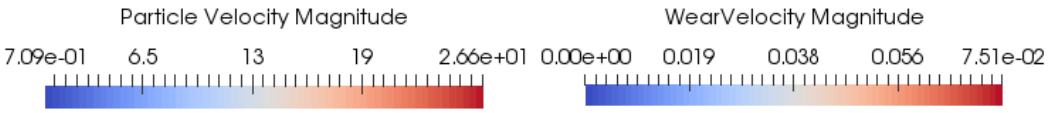

Figure 6.7: Wear profiles for medium sand particles with target surface material Carbon Steel 1018. (a) shows the normalised wear profile based on distance after the step at x=0.103m. Normalisation of wear depth is based on min-max normalisation. (b) is the 3-dimensional domain with visible adaptive mesh and (c) is the wear profile along slice z=0 with presence of representative particles at t=0.025s.

(a) t=0s

(b) t=0.005s

(c) t=0.01s

Figure 6.8: 3 dimensional simulation wear profiles for medium sand particles with target surface material Carbon Steel 1018. Time steps of the profiles are taken every t=0.005s.

(d) t=0.015s

(e) t=0.02s

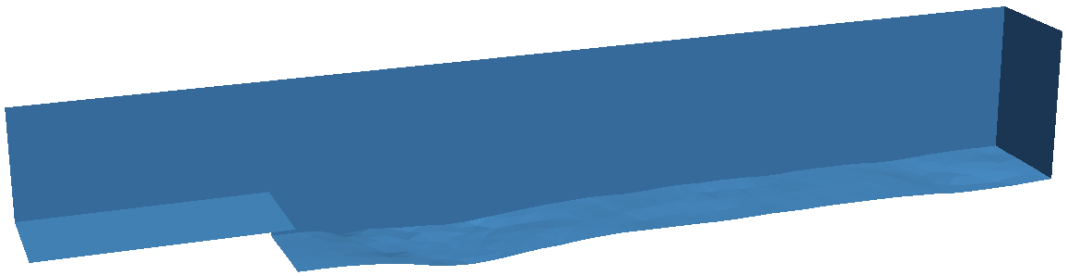

(f) t=0.025s

Figure 6.8: 3 dimensional simulation wear profiles for medium sand particles with target surface material Carbon Steel 1018. Time steps of the profiles are taken every t=0.005s.

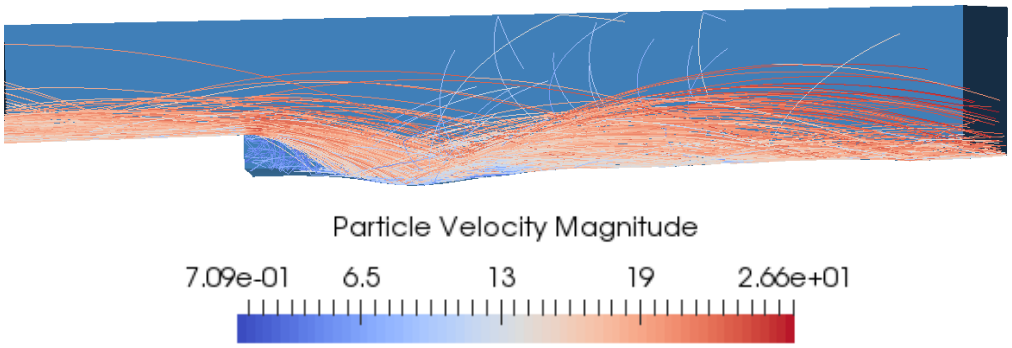

Figure 6.9: A close up cross section of medium particle rebounding off the deforming material surface after falling off the step.

(a) t=0s

(b) t=0.005s

(c) t=0.01s

Figure 6.10: 3 dimensional simulation wear profiles for fine sand particles with target surface material Carbon Steel 1018. Time steps of the profiles are taken every t=0.005s.

(d) t=0.015s

(e) t=0.02s

(f) t=0.025s

Figure 6.10: 3 dimensional simulation wear profiles for fine sand particles with target surface material Carbon Steel 1018. Time steps of the profiles are taken every t=0.005s.

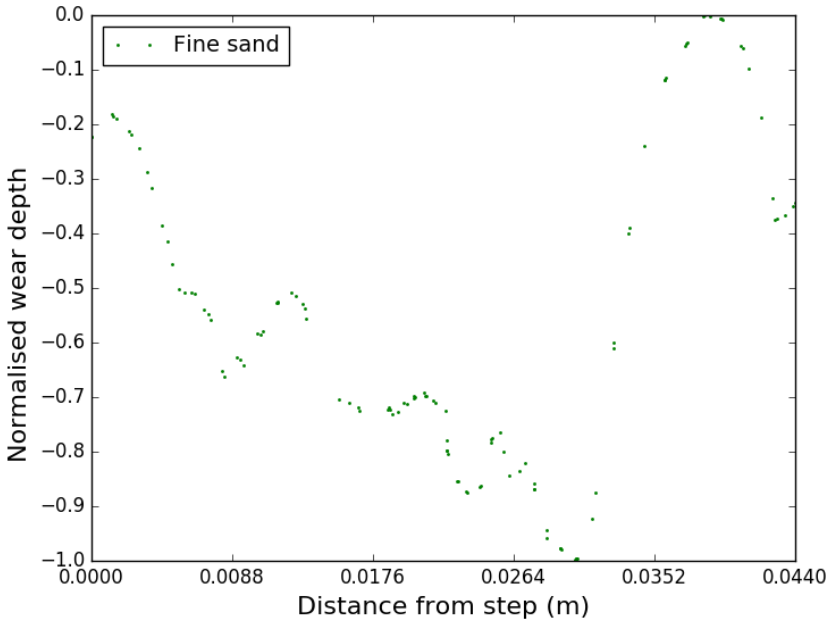

(a) Normalised wear profile

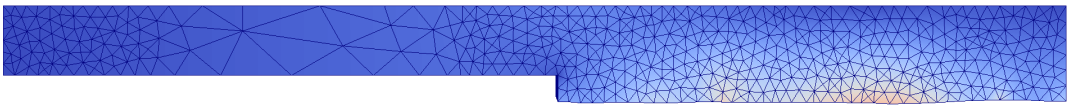

(b) Simulation wear profile mesh

(c) Simulation wear profile

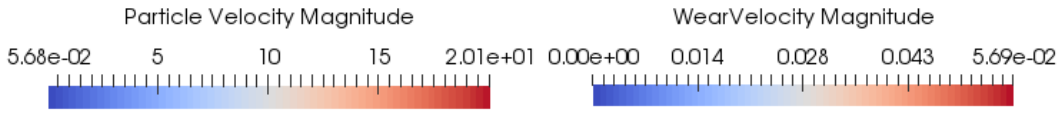

Figure 6.11: Wear profiles for fine sand particles with target surface material Carbon Steel 1018. (a) shows the normalised wear profile based on distance after the step at x=0.103m. Normalisation of wear depth is based on min-max normalisation. (b) is the 3-dimensional domain with visible adaptive mesh and (c) is the wear profile along slice z=0 with presence of representative particles at t=0.025s.

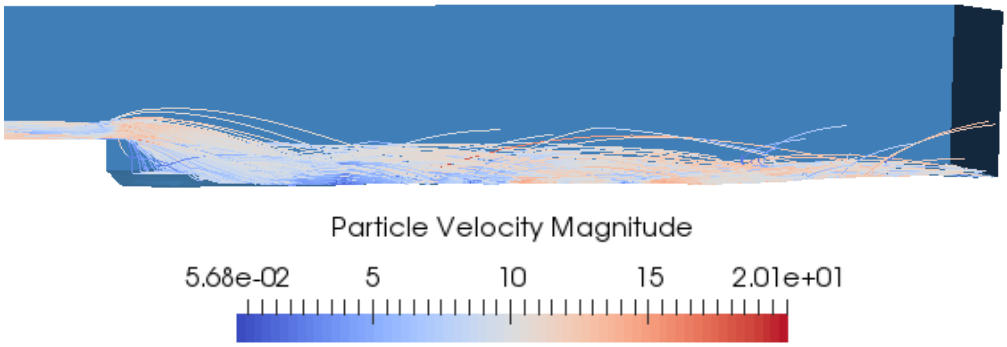

Figure 6.12: A close up cross section of fine sand particle behaviour remaining close to the deforming boundary after falling off the step.

$\frac{2}{3}$ of the magnitude of the first impact. The overall magnitude of wear for medium sand particles is half that of garnet particles. Fine sand particles displays a different wear profile resembling a sliding motion as they do not possess sufficient inertial post initial particle-wall collision.

Figure 6.14 displays the behaviour of adaptivity as time progressed for the varying particle sizes. All three particle sizes had the same initial number of elements and nodes, however there is a trend that the larger the particle size the greater number of elements and nodes used within the domain, which is representative of the amount of wear experienced. The increase in the number of nodes and element present around at t=0.005s corresponds well with the time of first impact with the deforming boundary surface and is seen to converge towards a constant value as time progresses. The wide variations in the total number of elements and nodes at the start of the simulation and the fact that the number towards the end of the simulation is smaller than the maximum number highlights the significance of adaptive mesh technology in providing resolution where required, while reducing computational cost where possible.

Volume loss based on particle sizes is displayed in Figure 6.15. As expected, garnet particles displayed the greatest volume loss over time, more than double that of medium sand particles and seven times greater than fine sand particles. Time taken for wear to produce loss in volume is fastest for garnet at t=0.0026s, with medium sand particles at t=0.0033s and fine sand taking t=0.0053s. This is due

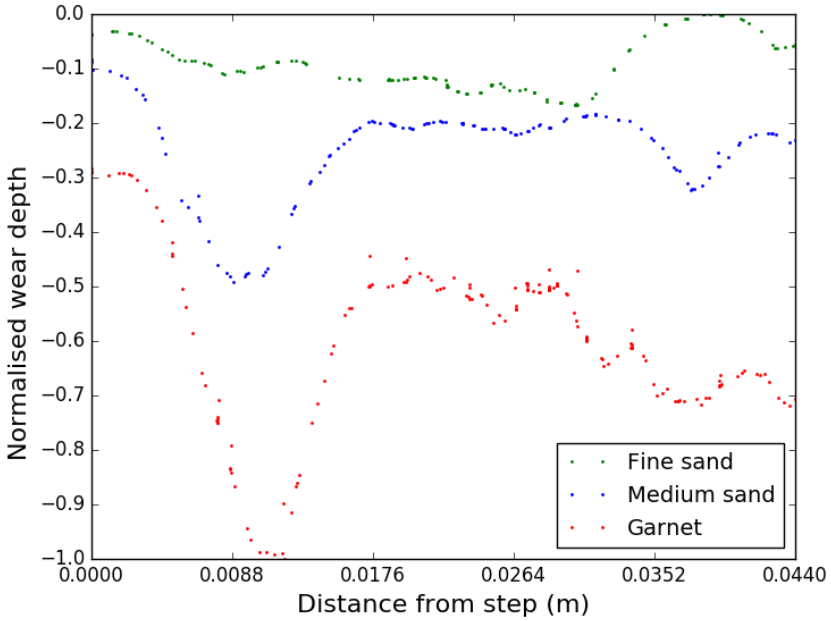

Figure 6.13: Normalised wear profile at varying particle sizes for Carbon Steel 1018 at t=0.025s. Wear profile taken from the midpoint of the domain, along z = 0. Normalisation of wear depth is based on min-max normalisation across all particle sizes.

to large garnet sized particles possessing greater momentum compared to that of smaller particles and as a result produce greater impact velocities with the wall requiring fewer collision events to achieve the volume loss.

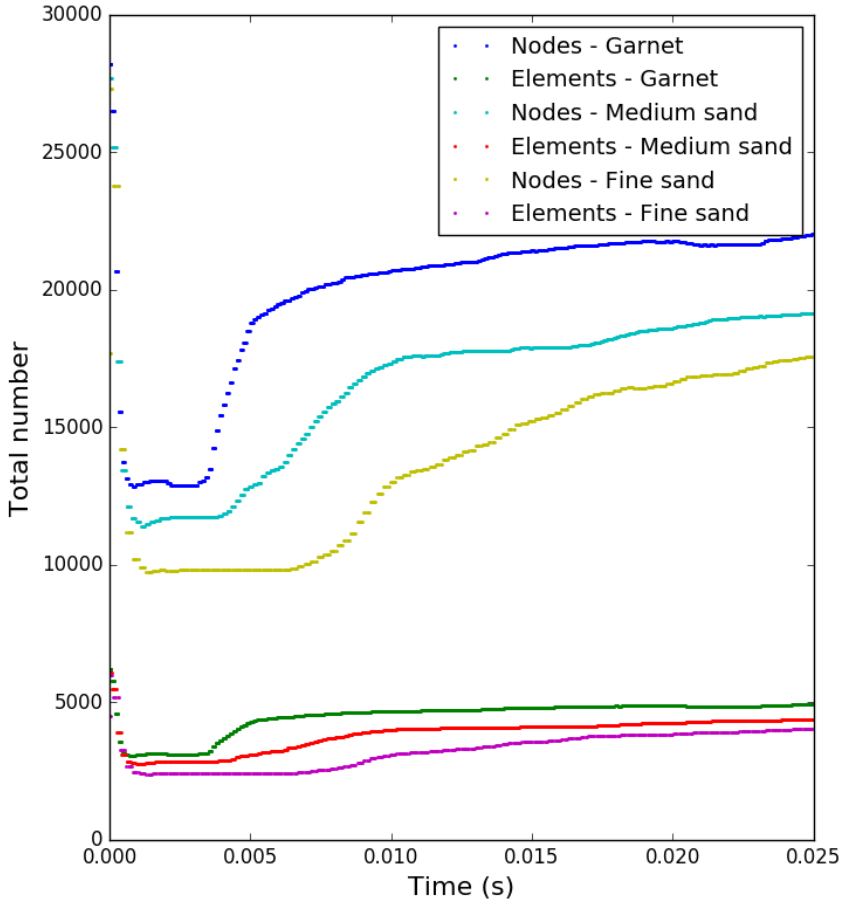

Figure 6.14: Number of nodes and elements within the domain with mesh movement and adaptive mesh for varying particle sizes for Carbon Steel 1018. Number of elements and nodes with varying particle sizes are proportional to the amount of wear experienced.

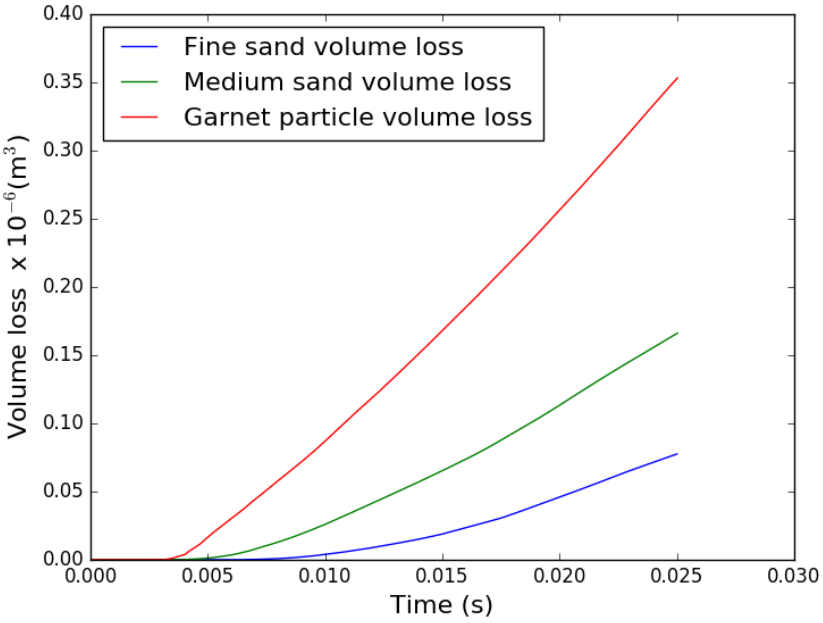

Figure 6.15: Total volume loss at varying particle sizes for Carbon Steel 1018 at t=0.025s.

6.3.2 Material properties

Effects on wear profile with varying target material properties is studied here with the use of Stainless Steel 316 as the second target material. Figure 6.16 shows the normalised wear profile for Stainless Steel 316 again with the two distinct regions of wear as with Carbon Steel 1018 confirming the behaviour of larger sized particles possessing sufficient inertial for multiple particle-wall collisions (see Figure 5.8). Figure 6.17 shows when the wear depth is normalised with that of Carbon Steel 1018, the results show the maximum wear depth occurs at the same distance of 0.01m away from the step. Post particle-wall collision, Carbon Steel 1018 has a great wear depth before the second region of wear towards the outlet of the domain. On the other hand, Stainless Steel 316 had minimal wear between the two regions.

When comparing the material properties and the empirical constants derived for those materials, Stainless Steel 316 possesses greater density and Vickers hardness with a density of 8000kgm^{-3} compared to 7870kgm^{-3} for Carbon Steel 1018. More significantly, the deformation erosion factor for Stainless Steel 316 is a third of that

for Carbon Steel 1018 having a value of 1.4 x 10^{11}. Stainless Steel 316 also possesses a higher threshold velocity by an order of magnitude. The threshold velocity defines the minimum velocity below which the deformation erosion is negligible. This suggests the area between the two distinct regions ($0.0176m \leq x \leq 0.0264m$ has its main contribution from deformation erosion where Carbon Steel 1018 is more susceptible when compared to Stainless Steel 316.

Furthermore as the cutting erosion ratio is a function of Vickers hardness Hv with $ER_C \propto \frac{1}{\sqrt{Hv}}$ (see Equation 2.35) and Stainless Steel 316 has a greater value by almost a factor of 2 when compared to Carbon Steel 1018 resulting in a smaller contribution to cutting erosion factor when presented with the same particle trajectory. As the total wear experienced is made up of the cutting erosion factor and the deformation erosion factor, a smaller contribution from the cutting erosion for Stainless Steel 316 results in a smaller overall total wear experienced as observed with the difference in magnitude in normalised wear depth.

6.3.3 Solid concentration

The study of the effect solid concentration by weight on the wear profile is conducted in this section with the use of garnet particles and target material of Carbon Steel 1018. The default concentration of 20% was selected due to the availability of experimental data. Solid concentrations of 10% and 30% are numerically simulated in this thesis with the particle insertion rate configured to 0.7 x $10^5 s^{-1}$ and 2.1 x $10^5 s^{-1}$ respectively. All other physical parameters of the system remains the same as that of the default simulation at 20% concentration. The result of normalised wear depth across the varying concentrations is presented in Figure 6.18. As with 20% solid concentration, two distinct regions of wear exists and occurs at approximately 0.01m and 0.03m from the step, which is similar for all concentrations. However, the overall shape of the wear profile differs between the concentrations, the wear profile for 30% solid concentration is the most erratic given the particle-fluid and particle-particle interactions with a greater number of particles present in the system. This behaviour is not expected as more particles in the systems should produce a smoother

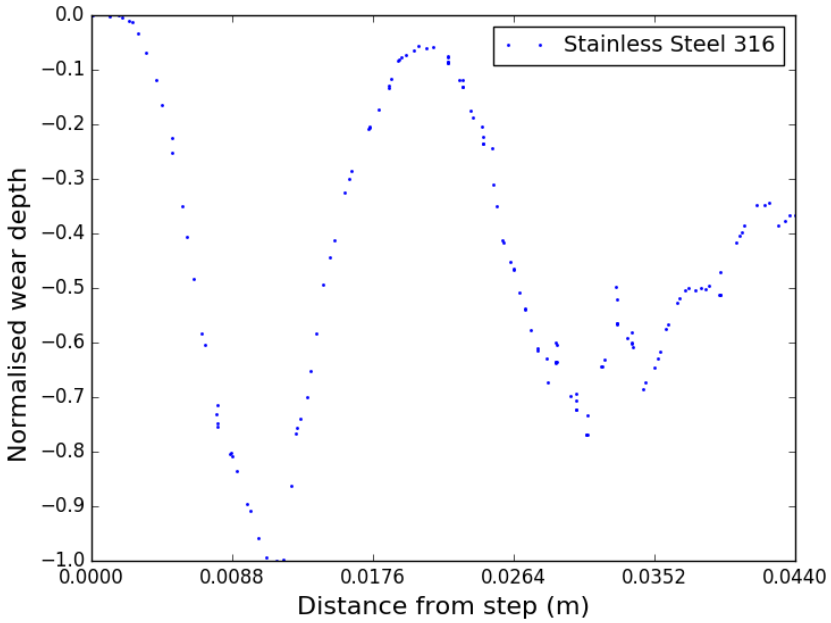

(a) Normalised wear profile

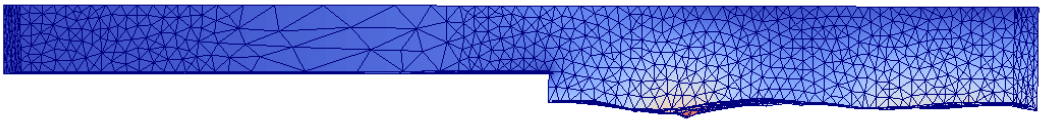

(b) Simulation wear profile mesh

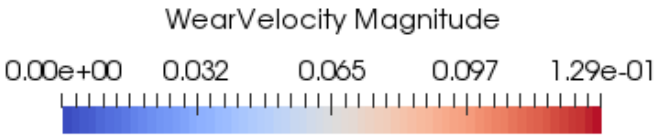

Figure 6.16: Comparison of wear profiles between normalised wear depth against distance from step and its corresponding simulation profile for garnet sized particles and Stainless Steel 316 at t = 0.025s. Normalisation of wear depth is based on min-max normalisation.

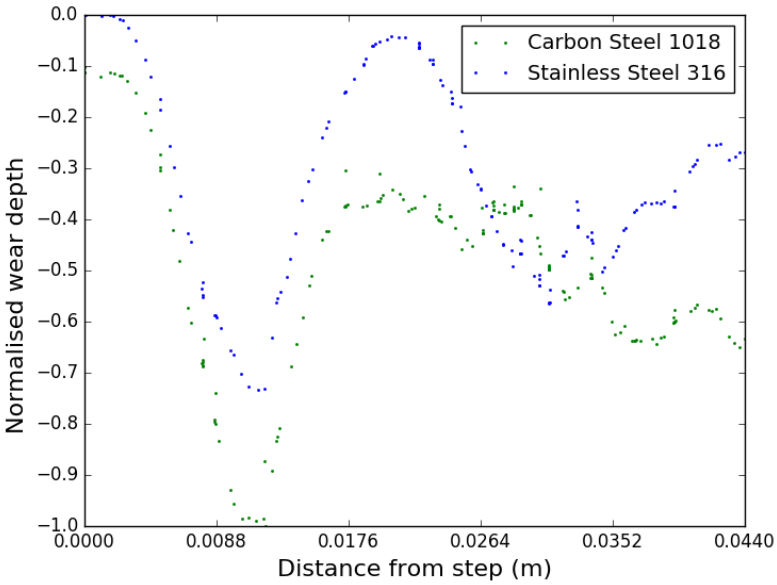

Figure 6.17: Normalised wear profile for garnet particles with Carbon Steel 1018 and Stainless Steel 316 at t =0.025s. Wear profile taken from the midpoint of the domain, along z = 0. Normalisation of wear depth is based on min-max normalisation across both material properties.

wear profile due to the increase in particle collisions. This could be due to the acceleration factor remaining the same as that of 20% solid concentration case and should be reduced so that it does not dominate the overall multiphase flow. When considering maximum wear depth taken at the initial collision after the step, a linear relationship can be observed in Figure 6.19 with maximum normalised depth of 0.29, 0.61 and 1 for solid concentrations of 10%, 20% and 30% respectively. Overall volume loss at varying solid concentrations in Figure 6.20 where volume loss increases a rate below first order to solid concentration with values summarised in Table 6.1. The increase in number of particles as solid concentration increase will increase the wear rate as there will be more particle-wall collisions, however at high concentrations particle-particle interactions, in the form of granular pressure, will reduce the proportion of the particles that collide with the wall reducing the amount of total wear and volume loss. Conversely, there is a competing effect from the fluid, as the solid concentration increases, the fluid will move more strongly towards the wall off the step as the drag from the particles pulls the fluid towards that direction resulting in more wear. These competing effect explains the behaviour of volume loss increase at a rate below first order against solid concentration. It is worth noting that at a solid concentration by mass of 30% equates to a particle volume fraction of around 15%. Therefore the effects of particle-particle interactions via granular pressure are minimal when compared to the effects of the increase in number of collisions and particle-fluid interactions.

6.4 Conclusion

In this section, the effects of varying modelling, particle and material parameters are studied. Variation of the critical impact angle was able to reproduce the profile of the erosion factor against impact angle when compared to the literature, however, it was not able to reproduce the magnitude of the erosion factor. This is due to the fact that the critical impact angle is obtained empirically and thus restricted to the test cases and conditions under which it was created. Results should be treated with a level of uncertainty when trying to extrapolate the model for other test conditions.

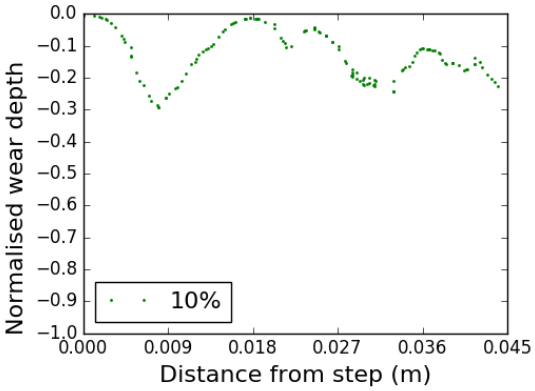

(a) 10% solid concentration

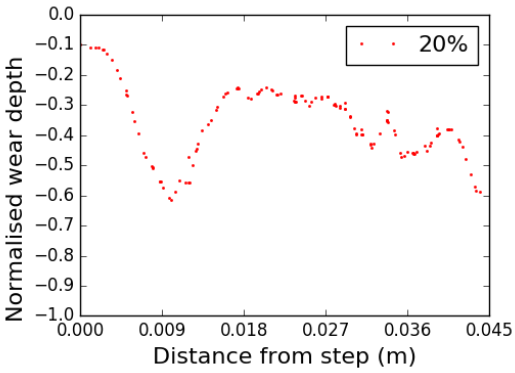

(b) 20% solid concentration

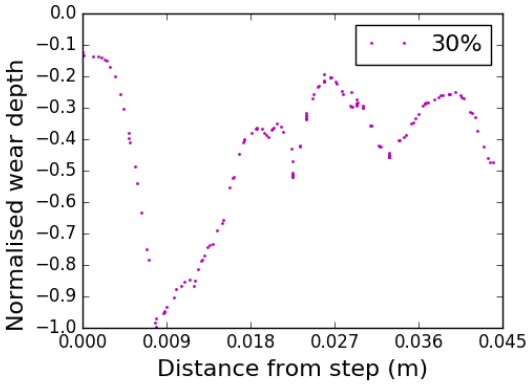

(c) 30% solid concentration

Figure 6.18: Normalised wear profiles at varying solid concentration by weight for Carbon Steel 1018. Wear profiles taken at t=0.025s along z=0. Normalisation of wear depth is based on min-max normalisation across all solid concentrations.

Solid concentration	**Max normalised wear depth**	**Total volume loss x 10^{-6}**
10 %,	0.29	0.20
20%,	0.61	0.35
30 %	1	0.48

Table 6.1: Maximium normalised wear depth and total volume loss at varying solid concentrations for garnet particles at time t=0.025s. Normalisation of wear depth is based on min-max normalisation across all solid concentrations.

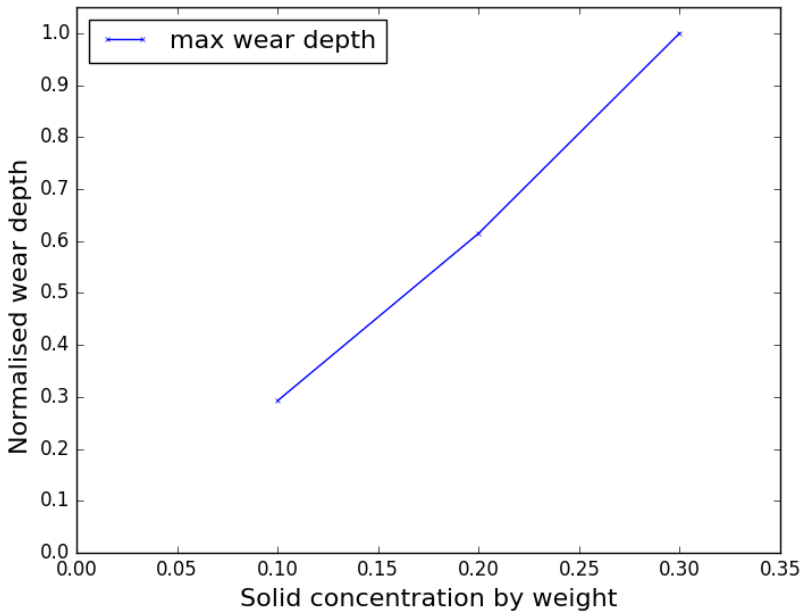

Figure 6.19: Maximum normalised wear depth is proportional to the solid concentration for garnet particles with Carbon Steel 1018 at t=0.025s.

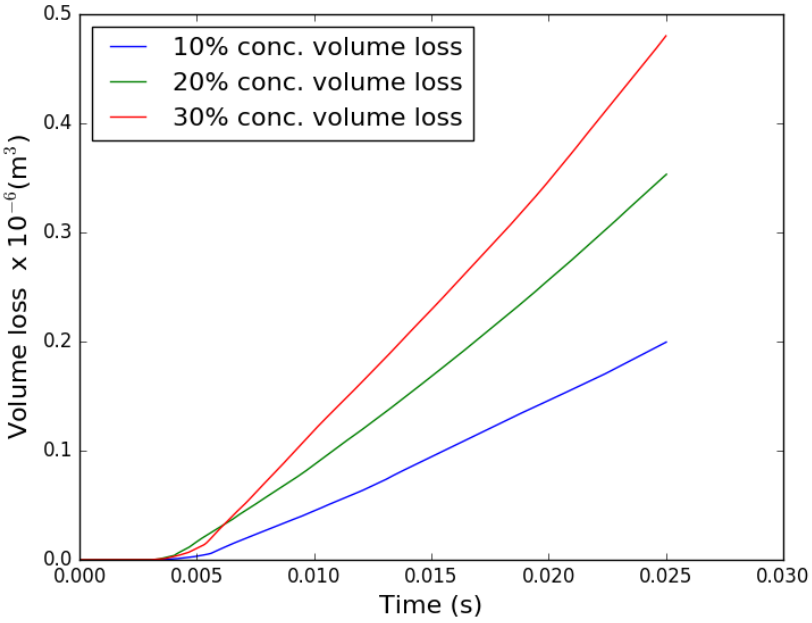

Figure 6.20: Total volume loss with varying solid concentrations using garnet particles with Carbon Steel 1018 at t=0.025s.

The artificial scaling of acceleration factor to speed up the effect of wear was able to increase the rate of wear without impacting on the behaviour of the particle-fluid and particle-wall interactions up to an acceleration factor of 1000. However, at an acceleration factor of 2000, it is evident that acceleration factor does have an impact on the wear profile with additional wear experienced towards the end of the Coriolis tester arm. Increasing the acceleration factor increases the significance of the coupling between the local fluid and wear. The wear experienced by a single representative particle is removing materials disproportionately faster than the time scale allows, thus causing an effect on the coupling between the local fluid flow and drag, therefore one local eddy experienced upstream can in turn create a greater influence downstream. As such, this indicates that the default acceleration factor of 1000 for the simulations as defined in Table 5.1 is within the correct time scale and did not adversely influence the behaviour of the multiphase flow. Results from Figure 6.4 show that the relationship between acceleration factor and wear depth and volume loss trends at just under first order where doubling the acceleration

factor will only increase its effect on wear profile by a factor of 1.5, this is due to the particles subject to Coriolis forces, gravity and interphase interactions affecting the particle trajectory and the subsequent wear relationships.

The effect of the diffusivity factor shows the importance of this scaling when modelling with representative particles where each impact event is representative of a larger number of particles in the actual system. This factor smooths out the wear experienced by a single representative particle through time and space, not just due to the particle scaling but also acceleration scaling. A low diffusivity factor will over exaggerate each wear impact event failing to smooth out its effect through space and time. Higher values of diffusivity factor may over compensate, increasing the smoothness of the wear profile at the cost of sensitivity to the genuine variance in wear.

On the study of particle size on wear profiles, larger particles are seen to possess sufficient inertia compared to the drag from the fluid post particle-wall collisions to leave the surface for further particle-wall collisions. As a result, a second region of wear is observed with a shallower region of impact indicating a reduction of momentum following the initial particle-wall collision. In comparison, fine sand particles an order of magnitude smaller in diameter than the large garnet particles remain close to the surface as it travels through the domain as these fine sand particles are heavily dominated by the fluid drag and do not possess the required inertial post particle-wall collision to leave the surface of the wall. Therefore, the wear observed for fine sand particles is due to the sliding motion of the particles as they travel through the Coriolis tester arm with no definitive region of wear.

The effect of target material properties was investigated using data presented in Arabnejad et al. [2015b]'s wear model. Carbon Steel 1018 and Stainless Steel 316 were the chosen target materials due to its density being comparable to the experimental target material A05HT (Section 5.4). When the same simulation parameters were conducted on Stainless Steel 316, Carbon Steel 1018 was more susceptible to wear, although the wear profiles for the two materials remain similar. This is due to the fact that the wear profiles with the distinct regions of wear is primarily driven by particle size and trajectory whereas the magnitude of wear driven by the cutting and

deformation erosion factors made up of empirical data. From the wear equation, the cutting erosion ratio is given as a function of Vickers hardness where $ER_c \propto \frac{1}{\sqrt{Hv}}$. As Stainless Steel 316 has a Vickers hardness of 224GPa which is almost double that of Carbon Steel 1018 at 131GPa, this result in a smaller contribution of cutting erosion factor when presented with the same trajectory parameters. Furthermore, Stainless Steel has a higher threshold velocity by an order of magnitude at which deformation erosion factor is relevant which also contributes for the smaller erosion ratio compared to that of Carbon Steel 1018 despite their similar densities.

Variations of solid concentration of particles was able to show normalised wear depth and volume loss trends at first order, where doubling the solid concentration almost doubled the maximum wear depth and volume loss as the rate of wear was just below first order. The wear profile for garnet particles at varying concentrations maintains the general pattern of two distinct regions of wear but at varying magnitudes of wear depth. The numerical simulation of the Coriolis tester arm was able to replicate the profile of the erosion factor at varying ratios of contact and corresponds well to the data presented in literature.

An understanding of the sensitivity to the modelling parameters as well as the behaviour of the physical parameters could allow industries to better understand the wear profile of their equipment under specific operating conditions. This could allow industries to design components that could help reduce wear through optimising flow conditions and operating parameters, improve performance and reliability of parts though better design of these parts and investigating the impact of wear in new products under development.

Chapter 7

Conclusions and Future Work

7.1 Conclusions

The research presented in this thesis was to develop a new wear modelling framework capable of modelling multiphase flow with moving boundaries which deforms in response to wear. The framework provides a comprehensive model incorporating the modelling of fluid flow, particle motion, wear modelling, boundary movement and the coupling between these components which has not yet been achieved within a single model prior to this thesis.Therefore, the ability to computationally model and simulate these systems would provide a great industrial advantage both from an economical and safety perspective providing the ability to design systems with improved performance and reliability.

Existing numerical methods faced limitations in solution accuracy of the model by failing to take into account the full coupling of the multiphase system, lacking the ability to dynamically deform boundaries in response to wear or the restrictions in computational resources when tracking individual particle trajectories in large domains [Nguyen et al., 2014], In addition, existing wear equations incorporated for CFD-based wear modelling is empirically based ([Chen et al., 2004], [Agrawal et al., 2019], [Zhang et al., 2007]), thus restricted to specific test cases and generates uncertainty when extrapolating to other test conditions [Parsi et al., 2014]. These

limitations motivated the adoption of the use of adaptive unstructured meshes to couple the wear equation to boundary movement. A hybrid Eulerian-Lagrangian multiphase model allowed the use of representative Lagrangian particles retaining the important particle trajectory information required for accurate wear modelling whilst parameterised particle-fluid and particle-particle interactions allowed for fast, fully coupled simulations in large domains. The research in the thesis was able to demonstrate that such an approach, in this new modelling framework, was able to predict behaviour of wear profiles and the importance of boundary movement in the study of wear.

The first use of mesh movement in response to wear presented in this thesis in Chapter 4, considered the jet impingement simulation in a 2D domain of a jet of fine particles in water and its effect of wear against a deforming boundary. The 2D test case is a simplified version of the industrially relevant abrasive slurry jet micro-machining technology. The importance of boundary movement in response to wear was confirmed as the evolution of the wear profile showed the changes in particle behaviour and trajectory changes in response to the deforming boundary. Comparison with a static boundary highlighted the difference in the wear velocity profile obtained. Both the deforming and static boundaries were observed to have identical wear velocity along the boundary at first impact before the velocity profile of the deforming boundary evolved over time decreasing in magnitude over time while the static case remained at the same magnitude over time. This result agrees with Nguyen et al. [2014]'s findings that wear is sensitive to the evolution of the surface profile, thus, the importance of including surface deformation when considering wear modelling.

Following the successful jet impingement test case, the application of boundary deformation in response to wear was applied to the 3 dimensional geometry of the Coriolis tester arm in the form of the 3 dimensional backward facing step. The wear modelling framework was able to successfully simulate the behaviour of differing particle sizes and its effect on wear. Large 1mm garnet particles created two distinct wear regions as they possessed sufficient inertia compared to fluid drag forces to leave the wall surface post particle-wall collision. As a result, further collisions of a

smaller magnitude created a shallower second region of wear towards the end of the Coriolis tester arm. In comparison, fine sand particles of 100μm exhibited a different wear profile under the same simulation conditions as particles remained close to the surface post particle-wall collision as their behaviour is dominated by Coriolis and drag forces and they do not possess the required inertia to leave the deforming surface. Therefore, the wear observed for fine sand particle was representative of sliding wear with no distinct regions of wear.

Comparison of numerical simulations was made against experimental wear scars obtained from Weir Minerals for target material A05HT in Chapter 5. The normalised wear profiles between experimental and numerical simulations compared well and showed good agreement in terms of magnitude and position of first impact through various slices along the Coriolis tester arm. However, the experimental wear scar showed a bias towards the left of the sample material with the loss of the second region of wear in the sample material which was not predicted in the numerical simulation. This could be due to both non uniform inlet flows and the finite size of the particles compared to the assumed point particles in the simulations. Limitation exists for the comparison of numerical simulations against experimental wear scars due to the fact that the wear model is based on a set of semi-mechanistic equations, thus still requiring input from empirical parameters (material properties, critical impact angle) obtained from experimentation conducted from literature. As such, best attempt was made to match the parameters of numerical simulation as closely as possible to the experimental data available. Whilst the results shows a good comparison between simulation and experimental data, it does generate a level of uncertainty when extrapolating empirically obtained modelling parameters.

The effect of target material properties and critical impact angle was investigated and the results compared well with that of literature data from [Arabnejad et al., 2015b]. Simulation of material properties between Carbon Steel 1018 and Stainless Steel 316 confirmed the relationship of the cutting erosion factor to be a function of material hardness given by Vickers hardness ($ER_C \propto \frac{1}{\sqrt{Hv}}$). Numerical simulations involving varying critical impact angle were able to reproduce the a similar erosion ratio profile for Carbon Steel 1018 for varying impact angles as presented in the

literature.

The artificial acceleration scaling used to increase the effect of wear experienced was able to successfully increase the rate of wear without significantly impacting on the particle-particle and particle-fluid interactions, thus maintaining the expected two regions of wear for garnet particles with varying magnitudes of wear depth. The rate of acceleration to wear depth was below a rate of first order.

The application of the pseudo-diffusivity factor used to spread out the effect of a single wear event in time and space due to the acceleration factor and under-representation of actual particles through the use of representative particles illustrated the importance of this scaling. A low diffusivity factor over exaggerates each wear event failing to spread out its effect through space and time, however, at larger diffusivity factors, there may be a risk of over smoothing at the cost of sensitivity to the genuine variation in wear. This loss of genuine variation in wear was observed for the case where the diffusivity factor was set to 0.004 for the simulation of garnet particles on Carbon Steel 1018 where the second region of wear towards the end of the Coriolis tester arm was smoothed out.

Overall, this research showed the successful implementation of a wear modelling framework for predicting wear profiles with deforming boundaries. This modelling framework can now be applied to simulate a variety of wear problem with industrial relevance, such as the simulation of wear in pipes with elbow bends and plugged tees common used in industry [Chen et al., 2004]. It has the potential to allow industries to better understand the wear profile of their equipment under specific operating conditions Providing industries with the ability to design components that could help reduce wear through optimising flow conditions and operating parameters, improve performance and reliability of parts though better design of these parts and investigating the impact of wear in new products under development. The wear modelling framework can be further enhanced by adding complexity in the modelling of particles and in order to improve on this framework, the following next steps are proposed.

7.2 Potential Areas for Future Work

The results in this thesis proved the capability of the wear modelling framework in predicting the behaviour of wear when surface deformation is considered. There are many more avenues of investigation and features that are beneficial which can further develop the basis of the wear modelling framework. These are summarised below:

1. **Finite sized particles** For larger particles, it is important to capture the effect on size of the particles during particle-wall collisions as there will be areas into which the centre of the particles cannot travel. As such, there should exist a region around the boundaries of the domain where wear and boundary deformation cannot occur.

2. **Distribution of particle sizes** Although simulations presented in this research were based on single sized particles, there is the opportunity to extend this research and enable a distribution of particle sizes within the framework through the coupling of the fluid to multiple instances of the Lagrangian particle model each consisting of a single sized particle. This would make the slurry mixture more representative of real-life scenarios.

3. **Distribution of particle shapes** This research was limited to the study of sand particles with a sharpness factor of $F_s = 0.5$. Similar to the distribution of particle sizes, the framework would be more industrially relevant should it consider a distribution of particle shapes with varying sharpness factor. This capability can be applied in a similar fashion to that for distributing particle sizes through the initialisation of multiple instances of the particle model coupled to the Fluidity framework.

4. **Implementation of shear and bulk viscosity for KTGF** As stated in Section 2.4.2, the solid stress tensor has been simplified to only include the solid pressure term excluding shear and bulk viscosity. The shear viscosity contains the kinetic and collision part of the particle-particle momentum exchange, whereas the bulk viscosity accounts for the resistance of these particles to compression and expansion. While the effects of these components are negligible as the fluidity across the domain is

relatively dilute, implementing the inclusion of these viscosities would broaden the applicability of this modelling framework to a great range of scenarios.

5. **Industrially relevant geometries - centrifugal pump** To fully leverage the potential of this wear modelling framework, numerical simulations of industrially relevant geometries involving large complex domains should be studied. An example of a relevant system is the centrifugal pump where there complexity exists with the geometry involving a rotating impeller enclosed within a stationery casing. Challenges in fluid fields exist as they are difficult to resolve in the narrow throatbush region of the pump between the impeller and casing as seen in Figure 7.1. Furthermore, the scale of these simulations is often infeasible with a DEM approach when tracking particles within the whole domain for the study of wear. There is no literature involving the simulation of fully coupled simulations of pump geometries taking into account the rotation of the impeller enclosed in a stationary casing with impellers which also deforms in response to wear. Initial work has been conducted in the simulation of particle motion within a centrifugal pump with rotating impellers as seen in Figure 7.2 The ability to numerically simulate wear in the centrifugal pump will prove invaluable to many industries.

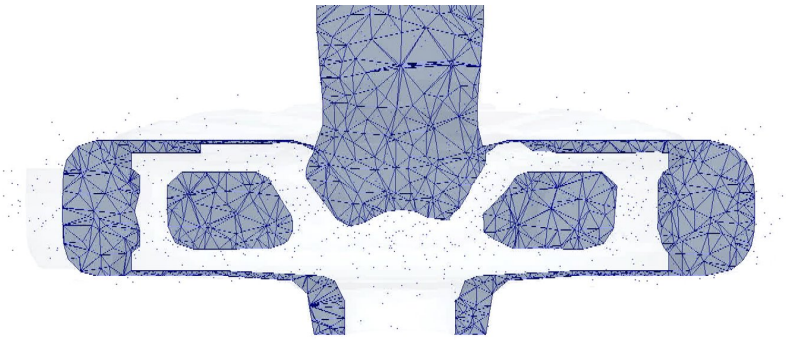

Figure 7.1: Cross-section of centrifugal pump highlighting the narrow throatbush region between impeller and casing.

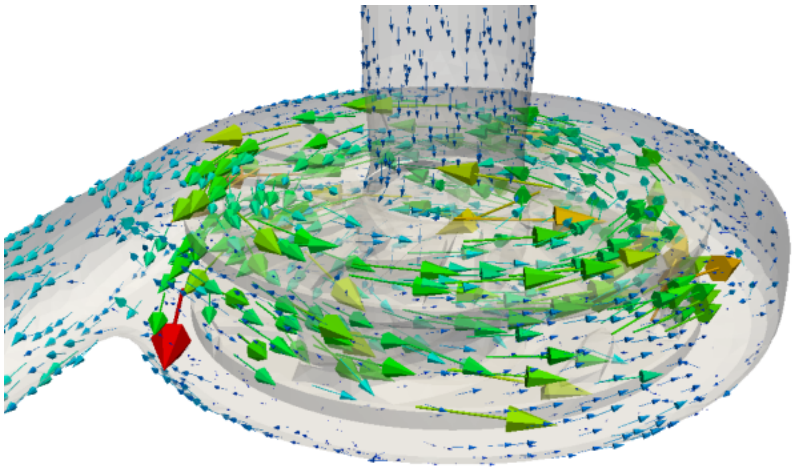

Figure 7.2: Particle flow within a centrifugal pump with rotating impellers. Arrows depict the particle velocity magnitude and direction.

Bibliography

M. Adnan, J. Sun, N. Ahmad, and J. J. Wei. Verification and validation of the ddpm-emms model for numerical simulations of bubbling, turbulent and circulating fluidized beds. *Powder Technology*, 379:69–88, 2020.

M. Agrawal, S. Khanna, A. Kopliku, and T. Lockett. Prediction of sand erosion in cfd with dynamically deforming pipe geometry and implementing proper treatment of turbulence dispersion in particle tracking. *Wear*, 426-427:596–604, 2019. ISSN 0043-1648. doi: https://doi.org/10.1016/j.wear.2019.01.018. URL https://www.sciencedirect.com/science/article/pii/S0043164819300286. 22nd International Conference on Wear of Materials.

J.P. Andrews. Theory of collision of spheres of soft metals. *The London, Edinburgh, and Dublin Philosophical Magazine and Journal of Science*, 58:593–610, 1930. doi: https://doi.org/10.1080/14786443008565033.

M. J. Andrews and P. J. O'Rourke. The multiphase particle-in-cell (mp-pic) method for dense particulate flows. *International Journal of Multiphase Flow*, 22:379–402, 1996.

ANSYS Inc. Ansys fluent 12.0/12.1 documentation, 2009. URL https://www.afs.enea.it/project/neptunius/docs/fluent/index.htm.

H. Arabnejad, A. Mansouri, S. A. Shirazi, and B. S. Mclaury. Evaluation of Solid Particle Erosion Equations and Models for Oil and Gas. *SPE Annual Technical Conference and Exhibition*, (April 2016), 2015a. doi: 10.2118/174987-MS.

H. Arabnejad, A. Mansouri, S. A. Shirazi, and B. S. McLaury. Development of mechanistic erosion equation for solid particles. *Wear*, 332-333:1044–1050, 2015b. ISSN 00431648. doi: 10.1016/j.wear.2015.01.031.

H. Arabnejad, A. Mansouri, S. A. Shirazi, and B. S. McLaury. Abrasion erosion modeling in particulate flow. *Wear*, 2017. ISSN 00431648. doi: 10.1016/j.wear.2017.01.042.

M. Atkinson, E.V. Stepanov, D.P. Goulet, S.V. Sherikar, and J. Hunter. High pressure testing sand erosion in 3d flow channels and correlation with cfd. *Wear*, 263(1):270–277, 2007. ISSN 0043-1648. doi: https://doi.org/10.1016/j.wear.2007.01.100. URL https://www.sciencedirect.com/science/article/pii/S0043164807004115. 16th International Conference on Wear of Materials.

S. Bahadur and R. Badruddin. Erodent particle characterization and the effect of particle size and shape on erosion. *Wear*, 138(1):189–208, 1990. ISSN 0043-1648. doi: https://doi.org/10.1016/0043-1648(90)90176-B. URL https://www.sciencedirect.com/science/article/pii/004316489090176B.

S. Balay, S. Abhyankar, M. F. Adams, J. Brown, P. Brune, K. Buschelman, L. Dalcin, V. Eijkhout, D. Kaushik, M. G. Knepley, L. Curfman McInnes, W. D. Gropp, K. Rupp, B. F. Smith, S. Zampini, H. Zhang, and H. Zhang. Petsc users manual. Technical Report ANL-95/11 - Revision 3.7, Argonne National Laboratory, 2016.

F. Bassi and S. Rebay. A high-order accurate discontinuous finite element method for the numerical solution of the compressible navier–stokes equations. *Journal of Computational Physics*, 131(2):267–279, 1997. ISSN 0021-9991. doi: https://doi.org/10.1006/jcph.1996.5572. URL https://www.sciencedirect.com/science/article/pii/S0021999196955722.

G. K. Batchelor. *An introduction to fluid dynamics*. Cambridge University Press, Cambridge, 1967.

G. Bhutani. *Numerical modelling of polydispersed flows using an adaptive-mesh*

finite element method with application to froth flotation. PhD thesis, Imperial College London, 2016.

.G.A. Bitter. A study of erosion phenomena part i. *Wear*, 6(1):5–21, 1963. doi: https://doi.org/10.1016/0043-1648(63)90003-6.

C. E. Brennen. *Fundamentals of Multiphase Flow*. Cambridge University Press, 2005. doi: 10.1017/CBO9780511807169.

S.-N. Carey, H. Sigurdsson, and R.-S.-J. Sparks. Experimental studies of particle-laden plumes. , 93(B12):15,314–15,328, December 1988. doi: 10.1029/JB093iB12p15314.

S. Chapman. *The mathematical theory of non-uniform gases : an account of the kinetic theory of viscosity, thermal conduction and diffusion in gases*. Cambridge University Press, London, 3rd ed / prepared in co-operation with d. burnett. edition, 1970. ISBN 0521075777.

X. Chen and J. Wang. A comparison of two-fluid model, dense discrete particle model andcfd-dem method for modeling impinging gas–solidflows. *Powder Technology*, 254:94–102, 2014.

X. Chen, B. S. McLaury, and S. A. Shirazi. Application and experimental validation of a computational fluid dynamics (CFD)-based erosion prediction model in elbows and plugged tees. *Computers and Fluids*, 33(10):1251–1272, 2004. ISSN 00457930. doi: 10.1016/j.compfluid.2004.02.003.

X. Chen, B. S. McLaury, and S. A. Shirazi. A Comprehensive Procedure to Estimate Erosion in Elbows for Gas/Liquid/Sand Multiphase Flow. *Journal of Energy Resources Technology*, 128(1):70–78, 08 2006. doi: 10.1115/1.2131885. URL https://doi.org/10.1115/1.2131885.

H. McI. Clark. Particle velocity and size effects in laboratory slurry erosion measurements or... do you know what your particles are doing? *Tribology International*, 35(10):617–624, 2002. ISSN 0301-679X. doi: https://doi.

org/10.1016/S0301-679X(02)00052-X. URL https://www.sciencedirect.com/science/article/pii/S0301679X0200052X. Tribo-Erosion.

S. Cloete, S. T. Johansen, and S. Amini. Performance evaluation of a complete lagrangian ktgf approach for dilute granular flow modelling. *Powder Technology*, 226:43–52, 2012. ISSN 0032-5910. doi: https://doi.org/10.1016/j.powtec.2012.04.010.

M. Colombo and M. Fairweather. Multiphase turbulence in bubbly flows: Rans simulations. *International Journal of Multiphase Flow*, 77:222–243, 2015. ISSN 0301-9322. doi: https://doi.org/10.1016/j.ijmultiphaseflow.2015.09.003.

C. J. Cotter and D. A. Ham. Numerical wave propagation for the triangular p1dg–p2 finite element pair. *Journal of Computational Physics*, 230(8):2806–2820, 2011. ISSN 0021-9991. doi: https://doi.org/10.1016/j.jcp.2010.12.024. URL https://www.sciencedirect.com/science/article/pii/S0021999110006984.

C. J. Cotter, D. A. Ham, and C. C. Pain. A mixed discontinuous/continuous finite element pair for shallow-water ocean modelling. *Ocean Modelling*, 26 (1):86–90, 2009. ISSN 1463-5003. doi: https://doi.org/10.1016/j.ocemod.2008.09.002. URL https://www.sciencedirect.com/science/article/pii/S1463500308001479.

C. T. Crowe. *Multiphase Flow Handbook*. Mechanical and Aerospace Engineering Series. CRC Press, 2005. ISBN 9781420040470. doi: https://doi.org/10.1201/9781420040470.

S. Cuomo. Modelling of flowslides and debris avalanches in natural and engineered slopes: a review. *IGeoenviron Disasters*, 7, 2020. doi: https://doi.org/10.1186/s40677-019-0133-9.

J. Ding and D. Gidaspow. A bubbling fluidization model using kinetic theory of granular flow. *AIChE Journal*, 36(4):523–538, 1990. doi: 10.1002/aic.690360404.

J. Donea and A. Huerta. *Finite Element Methods for Flow Problems*. Wiley, New York, 2003. ISBN 0471496669.

D. A. Drew and S. L. Passman. *Theory of Multicomponent Fluids*. Springer, 1999.

R. Durand and E. Condolios. Experimental investigation of the transport of solids in pipes. *Deuzieme Journee de l'hydraulique, Societe Hydrotechnique de France*, 1952.

S. Elghobashi. On predicting particle-laden turbulent flows. *Applied Scientific Research*, 52(4):309–329, 1994. ISSN 00036994. doi: 10.1007/BF00936835.

H. C. Elman. *Finite elements and fast iterative solvers : with applications in incompressible fluid dynamics*. Numerical mathematics and scientific computation. Oxford University Press, Oxford, second edition. edition, 2014. ISBN 0199678804.

S. Ergun. Fluid flow through packed columns. *Chemical Engineering Progress*, 48: 82–94, 1952.

J. Fan, J. Yao, X. Zhang, and K. Cen. Experimental and numerical investigation of a new method for protecting bends from erosion in gas-particle flows. *Wear*, 251(1):853–860, 2001. ISSN 0043-1648. doi: https://doi.org/10.1016/S0043-1648(01)00742-6. URL https://www.sciencedirect.com/science/article/pii/S0043164801007426. 13th International Conference on Wear of Materials.

P. E. Farrell. *Galerkin projection of discrete fields via supermesh construction*. PhD thesis, Imperial College London, 2009.

P. E. Farrell, M. D. Piggott, G. J. Gorman, D. A. Ham, and C. R. Wilson. Automated continuous verification and validation for numerical simulation. *Geoscientific Model Development Discussions*, 3:1587–1623, 2010. doi: 10.5194/gmdd-3-1587-2010. URL http://dx.doi.org/10.5194/gmdd-3-1587-2010.

Y. M. Ferng. Predicting local distributions of erosion–corrosion wear sites for the piping in the nuclear power plant using cfd models. *Annals of Nuclear Energy*, 35(2):304–313, 2008. ISSN 0306-4549. doi: https://doi.org/10.1016/j.anucene.2007.06.010. URL https://www.sciencedirect.com/science/article/pii/S0306454907001466.

J. H. Ferziger. *Computational methods for fluid dynamics*. Springer, third edition edition, 2002. ISBN 3540420746.

I. Finnie. Erosion of surfaces by solid particles. *Wear*, 3(2):87–103, 1960. ISSN 00431648. doi: 10.1016/0043-1648(60)90055-7.

I. Finnie and D. H. McFadden. On the velocity dependence of the erosion of ductile metals by solid particles at low angles of incidence. *Wear*, 48(1):181–190, 1978. ISSN 0043-1648. doi: https://doi.org/10.1016/0043-1648(78)90147-3. URL https://www.sciencedirect.com/science/article/pii/0043164878901473.

A. Forder, M. Thew, and D.Harrison. A numerical investigation of solid particle erosion experienced within oilfield control valves. *Wear*, 216:184–193, 1997.

M. B. Gandhi, R. Vuthaluru, H. Vuthaluru, D. French, and K. Shah. Cfd based prediction of erosion rate in large scale wall-fired boiler. *Applied Thermal Engineering*, 42:90–100, 2012. ISSN 1359-4311. doi: https://doi.org/10.1016/j.applthermaleng.2012.03.015. URL https://www.sciencedirect.com/science/article/pii/S1359431112001846. Heat Powered Cycles Conference, 2009.

C. Geuzaine and J. F. Remacle. Gmsh: A 3-d finite element mesh generator with built-in pre- and post-processing facilities. *International Journal for Numerical Methods in Engineering*, 79(11), 2009. doi: 10.1002/nme.2579. URL http://dx.doi.org/10.5194/gmdd-3-1587-2010.

A. Ghobeity, T. Krajac, T. Burzynski, M. Papini, and J.K. Spelt. Surface evolution models in abrasive jet micromachining. *Wear*, 264(3):185–198, 2008. ISSN 0043-1648. doi: https://doi.org/10.1016/j.wear.2007.02.020. URL https://www.sciencedirect.com/science/article/pii/S0043164807004280.

D. Gidaspow. *Multiphase flow and fluidization : continuum and kinetic theory descriptions*. Academic Press, Boston ;, 1994. ISBN 0122824709.

G. Grant and W. Tabakoff. Erosion prediction in turbomachinery resulting from environmental solid particles. *Journal of Aircraft*, 12:471–547, 1975. doi: https://doi.org/10.2514/3.59826.

K. Haugen, O. Kvernvold, A. Ronold, and R. Sandberg. Sand erosion of wear-resistant materials: Erosion in choke valves. *Wear*, 186-187:179–188, 1995. ISSN 0043-1648. doi: https://doi.org/10.1016/0043-1648(95)07158-X. URL https://www.sciencedirect.com/science/article/pii/004316489507158X. 8th International Conference on Erosion by Liquid and Solid Impact.

M. R. Hestenes and E. Stiefel. Methods of conjugate gradients for solving linear systems. *J Res NIST*, 49(6):409–436, 1952. doi: 10.6028/jres.049.044. URL http://dx.doi.org/10.6028/jres.049.044.

H.R. Hiester. *The application of adaptive mesh techniques to numerical simulations of gravity current flows*. PhD thesis, Imperial College London, 2 2012.

R. J. Hill, D. L. Koch, and J. C. Ladd. Moderate Reynolds number flows in ordered and random arrays ofarrays of spheres. *Journal of Fluid Mechanics*, 448:243–278, 2001. ISSN 0022-1120. doi: 10.1017/S0022112001005936.

Imperial College London. Fluidity manual v4.1.10. pages 1–321, 2014. ISSN 1098-6596. doi: 10.6084/m9.figshare.1089457. URL http://dx.doi.org/10.6084/m9.figshare.1089457.

M Ishii. *Thermo-fluid dynamic theory of two-phase flow*. Eyrolles, 1975.

C. T. Jacobs, G. S. Collins, M. D. Piggott, S. C. Kramer, and C. R.G. Wilson. Multiphase flow modelling of volcanic ash particle settling in water using adaptive unstructured meshes. *Geophysical Journal International*, 192(2):647–665, 2 2013. ISSN 0956540X. doi: 10.1093/gji/ggs059. URL http://gji.oxfordjournals.org/cgi/doi/10.1093/gji/ggs059.

C.T. Jacobs. *Modelling of multiphase flows on a daptive unstructured meshes with applications to the dynamics of volcanic ash plumes*. PhD thesis, Imperial College London, 10 2013.

J. T. Jenkins. Boundary Conditions for Rapid Granular Flow: Flat, Frictional Walls. *Journal of Applied Mechanics*, 59(1):120, 1992. ISSN 00218936. doi:

10.1115/1.2899416. URL http://appliedmechanics.asmedigitalcollection.asme.org/article.aspx?articleid=1410585.

A. L. Kartashev, M. A. Kartasheva, and A. A. Terekhin. Mathematical models of dynamics multiphase flows in complex geometric shape channels. *Procedia Engineering*, 206:121–127, 2017. ISSN 1877-7058. doi: https://doi.org/10.1016/j.proeng.2017.10.447. URL https://www.sciencedirect.com/science/article/pii/S1877705817351305. International Conference on Industrial Engineering, ICIE 2017.

S. C. Kramer, C. J. Cotter, and C. C. Pain. Solving the Poisson equation on small aspect ratio domains using unstructured meshes. *Ocean Modelling*, 35(3):253–263, January 2010. doi: 10.1016/j.ocemod.2010.08.001.

Y. Li, K.-J. Paik, T. Xing, and P. M. Carrica. Dynamic overset cfd simulations of wind turbine aerodynamics. *Renewable Energy*, 37(1):285–298, 2012. ISSN 0960-1481. doi: https://doi.org/10.1016/j.renene.2011.06.029. URL https://www.sciencedirect.com/science/article/pii/S0960148111003223.

M. Liebhard and A. Levy. The effect of erodent particle characteristics on the erosion of metals. *Wear*, 151(2):381–390, 1991. ISSN 0043-1648. doi: https://doi.org/10.1016/0043-1648(91)90263-T. URL https://www.sciencedirect.com/science/article/pii/004316489190263T.

E. Loth. Numerical approaches for motion of dispersed particles, droplets and bubbles. *Progress in Energy and Combustion Science*, 26:161–223, 2000.

C.K.K. Lun, S.B. Savage, D.J. Jeffrey, and N. Chepurniy. Kinetic theories for granular flow: inelastic particle in couette flow and slightly inelastic particle in a general flow field. *Journal of Fluid Mechanics*, 140:223–256, 1984.

J. Lundberg and B. M. Halvorsen. A review of some exsisting drag models describing the interaction between phases in a bubbling fluidized bed. *Proc. 49th Scand. Conf. Simulation and Modeling, Oslo University College, Oslo, Norway*, pages 7–8, 2008.

J. Y. Luo and A. D. Gosman. PREDICTION OF IMPELLER- INDUCED FLOW IN MIXING VESSELS USING MULTIPLE FRAMES OF REFERENCE. 1994.

S. MacNamara and G. Strang. *Operator Splitting*, pages 95–114. Springer International Publishing, Cham, 2016. ISBN 978-3-319-41589-5. doi: 10.1007/978-3-319-41589-5_3. URL https://doi.org/10.1007/978-3-319-41589-5_3.

T. Matsumura, T. Muramatsu, and S. Fueki. Abrasive water jet machining of glass with stagnation effect. *CIRP Annals*, 60(1):355–358, 2011. ISSN 0007-8506. doi: https://doi.org/10.1016/j.cirp.2011.03.118. URL https://www.sciencedirect.com/science/article/pii/S0007850611001193.

B. S. McLaury and S. A. Shirazi. An Alternate Method to API RP 14E for Predicting Solids Erosion in Multiphase Flow . *Journal of Energy Resources Technology*, 122 (3):115–122, 05 2000. ISSN 0195-0738. doi: 10.1115/1.1288209. URL https://doi.org/10.1115/1.1288209.

T. Mcmanus, J. Percival, B. Yeager, N. Barral, G. Gorman, and M. Piggott. Moving mesh methods in fluidity and firedrake. Technical report, 04 2017.

J. Mcnaughton, I. Afgan, D. D. Apsley, S. Rolfo, T. Stallard, and P. K. Stansby. A simple sliding-mesh interface procedure and its application to the CFD simulation of a tidal-stream turbine. *International Journal for Numerical Methods in Fluids*, 74(4):250–269, 2014. ISSN 02712091. doi: 10.1002/fld.3849.

R. L. Meakin. Composite overset structured grids. chapter 11. CRC Press, 1999.

H. C. Meng and K. C. Ludema. Wear models and predictive equations: their form and content. *Wear*, 181-183(PART 2):443–457, 1995. ISSN 00431648. doi: 10.1016/0043-1648(95)90158-2.

G. V. Messa and S. Malavasi. A cfd-based method for slurry erosion prediction. *Wear*, 398-399:127–145, 2018. ISSN 00431648. doi: 10.1016/j.wear.2017.11.025.

E. Michaelides, C. T. Crowe, and J. D. Schwarzkopf. *Multiphase flow handbook*. Mechanical and aerospace engineering series. CRC Press, second edition. edition, 2017. ISBN 1498701000.

S. J. Neethling and D. J. Barker. Using smooth particle hydrodynamics (sph) to model multiphase mineral processing systems. *Minerals Engineering*, 90:17–28, 2016. ISSN 0892-6875. doi: https://doi.org/10.1016/j.mineng.2015.09.022. URL https://www.sciencedirect.com/science/article/pii/S0892687515300923. Computational Modelling.

V. B. Nguyen, Q. B. Nguyen, Z. G. Liu, S. Wan, C. Y.H. Lim, and Y. W. Zhang. A combined numerical-experimental study on the effect of surface evolution on the water-sand multiphase flow characteristics and the material erosion behavior. *Wear*, 319(1-2):96–109, 2014. ISSN 00431648. doi: 10.1016/j.wear.2014.07.017. URL http://dx.doi.org/10.1016/j.wear.2014.07.017.

T. Nian, D. Li, Q. Liang, H. Wu, and X. Guo. Multi-phase flow simulation of landslide dam formation process based on extended coupled dem-cfd method. *Computers and Geotechnics*, 140:104438, 2021. ISSN 0266-352X. doi: https://doi.org/10.1016/j.compgeo.2021.104438. URL https://www.sciencedirect.com/science/article/pii/S0266352X21004286.

H. Nouraei, K. Kowsari, J.K. Spelt, and M. Papini. Surface evolution models for abrasive slurry jet micro-machining of channels and holes in glass. *Wear*, 309(1):65–73, 2014. ISSN 0043-1648. doi: https://doi.org/10.1016/j.wear.2013.11.003. URL https://www.sciencedirect.com/science/article/pii/S0043164813005383.

N. Odier, A. Thacker, M. Harnieh, G. Staffelbach, L. Gicquel, F. Duchaine, N. García Rosa, and J.-D. Müller. A mesh adaptation strategy for complex wall-modeled turbomachinery les. *Computers Fluids*, 214:104766, 2021. ISSN 0045-7930. doi: https://doi.org/10.1016/j.compfluid.2020.104766. URL https://www.sciencedirect.com/science/article/pii/S0045793020303364.

Y. I. Oka and T. Yoshida. Practical estimation of erosion damage caused by solid particle impact: Part 2: Mechanical properties of materials directly associated with erosion damage. *Wear*, 259(1-6):102–109, 2005. ISSN 00431648. doi: 10.1016/j.wear.2005.01.040.

Y. I. Oka, K. Okamura, and T. Yoshida. Practical estimation of erosion damage caused by solid particle impact: Part 1: Effects of impact parameters on a predictive equation. *Wear*, 259(1-6):95–101, 2005. ISSN 00431648. doi: 10.1016/j.wear.2005.01.039.

M. Ouda and E. A. Toorman. Development of a new multiphase sediment transport model for free surface flows. *International Journal of Multiphase Flow*, 117: 81–102, 2019. ISSN 0301-9322. doi: https://doi.org/10.1016/j.ijmultiphaseflow.2019.04.023. URL https://www.sciencedirect.com/science/article/pii/S0301932218308462.

C. C. Pain, A. P. Umpleby, C. R.E. de Oliveira, and A. J.H. Goddard. Tetrahedral mesh optimisation and adaptivity for steady-state and transient finite element calculations. *Computer Methods in Applied Mechanics and Engineering*, 190(29-30):3771–3796, 2001. ISSN 00457825. doi: 10.1016/S0045-7825(00)00294-2.

C. C. Pain, M. D. Piggott, A. J. H. Goddard, F. Fang, G. J. Gorman, D. P. Marshall, M. D. Eaton, P. W. Power, and C. R. E. de Oliveira. Three-dimensional unstructured mesh ocean modelling. *Ocean Modelling*, 10(1-2):5–33, 2005.

M. Parsi. *Sand Particle Erosion in Vertical Slug/churn flow*. PhD thesis, The University of Tulsa, 2015.

M. Parsi, K. Najmi, F. Najafifard, S. Hassani, B. S. McLaury, and S. A. Shirazi. A comprehensive review of solid particle erosion modeling for oil and gas wells and pipelines applications. *Journal of Natural Gas Science and Engineering*, 21:850–873, 2014. ISSN 1875-5100. doi: https://doi.org/10.1016/j.jngse.2014.10.001. URL https://www.sciencedirect.com/science/article/pii/S187551001400300X.

M. Parsi, A. Jatale, M. Agrawal, and P. Sharma. Effect of surface deformation on erosion prediction. *Wear*, 430-431:57–66, 2019. ISSN 0043-1648. doi: https://doi.org/10.1016/j.wear.2019.04.019. URL https://www.sciencedirect.com/science/article/pii/S0043164818313772.

S. Pedersen, P. Durdevic, and Z. Yang. Challenges in slug modeling and control for offshore oil and gas productions: A review study. *International Journal of Multiphase Flow*, 88:270–284, 2017. ISSN 0301-9322. doi: https://doi.org/10.1016/j.ijmultiphaseflow.2016.07.018. URL https://www.sciencedirect.com/science/article/pii/S0301932216300672.

M. D. Piggott, C. C. Pain, G. J. Gorman, P. W. Power, and A. J. H. Goddard. h, r, and hr adaptivity with applications in numerical ocean modelling. *Ocean Modelling*, 10(1-2):95–113, 2005. doi: 10.1016/j.ocemod.2004.07.007.

M. D. Piggott, G. J. Gorman, C. C. Pain, P. A. Allison, A. S. Candy, B. T. Martin, and M. R. Wells. A new computational framework for multi-scale ocean modelling based on adapting unstructured meshes. *International Journal for Numerical Methods in Fluids*, 56(8):1003–1015, 3 2008. ISSN 02712091. doi: 10.1002/fld.1663. URL http://doi.wiley.com/10.1002/fld.1663.

M. D. Piggott, P. E. Farrell, C. R. Wilson, G. J. Gorman, and C. C. Pain. Anisotropic mesh adaptivity for multi-scale ocean modelling. *Philosophical Transactions of the Royal Society A: Mathematical, Physical and Engineering Sciences*, 367(1907):4591–4611, 2009. ISSN 1364503X. doi: 10.1098/rsta.2009.0155.

Harker J. H. Backhurst J. R. Richardson, J. F. Elsevier, 2002. ISBN 978-0-7506-4445-7. URL https://app.knovel.com/hotlink/toc/id:kpCRCEVPT2/coulson-richardsons-chemical/coulson-richardsons-chemical.

Y. Saad and M. H. Schultz. Gmres: A generalized minimal residual algorithm for solving nonsymmetric linear systems. *SIAM Journal on Scientific and Statistical Computing*, 7(3):856–869, 1986. doi: 10.1137/0907058. URL https://doi.org/10.1137/0907058.

S. A. Shirazi, J. R. Shadley, B. S. McLaury, and E. F. Rybicki. A procedure to predict solid particle erosion in elbows and tees. *Journal of Pressure Vessel Technology; (United States)*, 117, 2 1995. ISSN 0094-9930. doi: 10.1115/1.2842089. URL https://www.osti.gov/biblio/6778457.

M. Sommerfeld. *Numerical Methods for Dispersed Multiphase Flows*, pages 327–396. Springer International Publishing, Cham, 2017. ISBN 978-3-319-60282-0. doi: 10.1007/978-3-319-60282-0_6. URL https://doi.org/10.1007/978-3-319-60282-0_6.

S. L. Soo. *Multiphase fluid dynamics*. Science Press, Beijing, 1990.

G.G. Stokes. On the Effect of the Internal Friction of Fluids on the Motion of Pendulums. *Transactions of the Cambridge Philosophical Society*, 9, 1851.

J. Tyacke, N. R. Vadlamani, W. Trojak, R. Watson, Y. Ma, and P.G. Tucker. Turbomachinery simulation challenges and the future. *Progress in Aerospace Sciences*, 110:100554, 2019. ISSN 0376-0421. doi: https://doi.org/10.1016/j.paerosci.2019.100554. URL https://www.sciencedirect.com/science/article/pii/S0376042119300715.

Yu. V. Vasilevskii and K. Lipnikov. An adaptive algorithm for quasioptimal mesh generation. *Computational Mathematics and Mathematical Physics*, 39:1468–1486, 1999.

R. E. Vieira and S. A. Shirazi. A mechanistic model for predicting erosion in churn flow. *Wear*, 476:203654, 2021. ISSN 0043-1648. doi: https://doi.org/10.1016/j.wear.2021.203654. URL https://www.sciencedirect.com/science/article/pii/S0043164821000430. 23rd International Conference on Wear of Materials.

C.-Y. Wen and Y. H. Yu. Mechanics of fluidization. *Chemical Engineering Progress Symposium Series*, 62:100–111–, 1966.

C. Wilson. *Modelling multiple-material flows on adaptive unstructured meshes*. PhD thesis, Imperial College London, 9 2009.

Z. Xie, D. Pavlidis, J. R. Percival, J. L.M.A. Gomes, C. C. Pain, and O. K. Matar. Adaptive unstructured mesh modelling of multiphase flows. *International Journal of Multiphase Flow*, 67(S):104–110, 2014. ISSN 03019322. doi: 10.1016/j.ijmultiphaseflow.2014.08.002. URL http://dx.doi.org/10.1016/j.ijmultiphaseflow.2014.08.002.

M. Xu, F. Chen, X. Liu, W. Ge, and J. Li. Discrete particle simulation of gas–solid two-phase flows with multi-scalecpu–gpu hybrid computation. *Chemical Engineering Journal*, 207-208:746–757, 2012.

Y. Zhang, E. P. Reuterfors, B. S. McLaury, S. A. Shirazi, and E. F. Rybicki. Comparison of computed and measured particle velocities and erosion in water and air flows. *Wear*, 263(1-6 SPEC. ISS.):330–338, 2007. ISSN 00431648. doi: 10.1016/j.wear.2006.12.048.

O. C. Zienkiewicz. *The finite element method : its basis and fundamentals*. Butterworth-Heinemann, Oxford, 7th edition, 2013. ISBN 008095135X.

O. C. Zienkiewicz. *The finite element method for fluid dynamics*. Elsevier/Butterworth-Heinemann, 7th edition, 2014. ISBN 0-08-095137-6.